Elementary quantum operations on Majorana systems

Nitsch, Maximilian

2025

Document Version:
Publisher's PDF, also known as Version of record

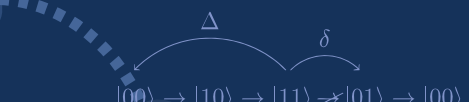

$$
\begin{aligned}
\partial_t p_e &= 2\Gamma(1 - 2p_e - s_e^z) \\
\partial_t s_e^z &= 2\Gamma(-s_e^z - s_o^z - p_e - \xi\, s_e^y) \\
\partial_t s_o^z &= 2\Gamma(-s_o^z + s_e^z + p_e + \eta\, s_o^y) \\
\partial_t s_e^x &= 2\Gamma(-s_e^x + s_o^y - I_P s_e^y) \\
\partial_t s_e^y &= 2\Gamma(-s_e^y + s_o^x + I_P s_e^x + \xi\, s_e^z) \\
\partial_t s_o^x &= 2\Gamma(-s_o^x + I_P s_o^y) \\
\partial_t s_o^y &= 2\Gamma(-s_o^y - I_P s_o^x - \eta\, s_o^z)
\end{aligned}
$$

Elementary quantum operations on Majorana systems

MAXIMILIAN NITSCH
DEPARTMENT OF PHYSICS | FACULTY OF ENGINEERING | LUND UNIVERSITY

$$H = i\,\gamma_0 \sum_k \varepsilon_k\,\gamma_k = i\,\Delta\,\gamma_0 \sum_k \frac{\varepsilon_k}{\Delta}\,\gamma_k = i\,\Delta\,\gamma_0\gamma_\Delta$$

$$P = \frac{1}{2}(1 - i\gamma_0\gamma_\Delta)$$

$$U = \mathcal{T}\exp\left(-\int_0^{\frac{\pi}{2}} [P, \partial_\omega P]\, d\omega\right)$$

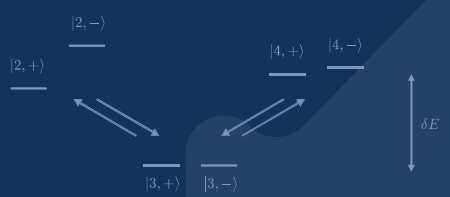

$$\Upsilon_m^{\alpha\beta} = \sum_{\substack{n \\ a,b,c=\pm}} \frac{-1}{E_n^{(m,c)} - E^{(3)}} |3a\rangle\langle 3a|\, d_\beta^\dagger\, |m,c,n\rangle\langle m,c,n|\, d_\alpha\, |3b\rangle\langle 3b|$$

$$\sum_{b,c=\pm} \langle 2,c,1|\, d_\alpha\, |3b\rangle\, |2,c,1\rangle\langle 3b| = \frac{\sin\theta}{\sqrt{2}} \begin{pmatrix} \xi_2(\delta_{\alpha,2} - \delta_{\alpha,1}) & \xi_2(\delta_{\alpha,4} - \delta_{\alpha,3}) \\ -\delta_{\alpha,3} - \delta_{\alpha,4} & \delta_{\alpha,1} + \delta_{\alpha,2} \end{pmatrix}$$

Printed by Media-Tryck, Lund 2025 NORDIC SWAN ECOLABEL 3041 0903

LUND UNIVERSITY

Division of Solid State Physics
Department of Physics
Faculty of Engineering

ISBN 978-91-8104-749-3

Elementary quantum operations on Majorana systems

Elementary quantum operations on Majorana systems

by Maximilian Nitsch

LUND
UNIVERSITY

Thesis for the degree of Doctor of Philosophy

Thesis advisor: Martin Leijnse
Supporting advisor: Ville F. Maisi

Faculty opponent: Ramón Aguado

To be presented, with the permission of the Faculty of Engineering of Lund University, for public criticism in the Rydberg lecture hall (Rydbergsalen, H418) at the Department of Physics on

Friday, the 5th of December 2025 at 09:15.

Organization	Document name
LUND UNIVERSITY Department of Physics Box 118 SE–221 00 LUND Sweden	**DOCTORAL DISSERTATION** Date of disputation 2025-12-05 Sponsoring organization
Author(s) Maximilian Nitsch	

Title and subtitle

Elementary quantum operations on Majorana systems

Abstract

This thesis aims to investigate the novel physics around Majorana bound states (MBSs). MBSs are quasiparticle excitations predicted to exist in topological superconductors. Due to the inherent protection they obtain from their topology, they have long been regarded as a promising setup to build a topologically protected quantum computer. Apart from this very practical application, they continue to fascinate as platforms built with MBS exhibit unique effects like nonabelian braiding and non-Fermi liquid behaviour in the topological Kondo effect.

The thesis starts with a general introduction to quantum computing, highlighting both the promises and challenges of that field. Afterwards follows an introduction to systems that are candidates to host MBSs. It focuses on the theoretical proposals and experimental realizations that are most relevant to the presented work. We continue with a summary of the most fundamental effects and the setups that make the physics of MBSs accessible.

The author's contributions in this field are theoretical. However, each publication comes with the explicit goal of investigating setups that make the unique physics of MBSs directly accessible in experiments. The first three papers have been peer-reviewed and were published in scientific journals. The fourth one is currently under peer review. The first two papers investigate DC transport setups connecting to a qubit based on MBSs called the MBS tetron. We show that via an effect called parity blockade, it is possible to initialize the qubit, quantify its lifetime, and determine whether it holds MBSs or trivial (normal fermionic) states. Also employing parity blockade, the second paper establishes a transport setup that enables access to MBS fusion rules, an effect directly related to nonabelian braiding. The third paper translates the concept of a MBS tetron into the newly experimentally established approach of MBSs in quantum dot-based Kitaev chains. We denote this system the poor man's Majorana tetron. We find that the poor man's Majorana tetron in a transport setup with appropriate tuning exhibits the famed topological Kondo effect. Paper IV focuses on nonabelian braiding. It investigates the hybridization-based braiding protocol and accounts for imperfections in MBS localization, breaking the ground state degeneracy. This detrimental effect is corrected by the introduction of a correction term, followed by a full analytical solution of the transformation induced by this generalized braiding protocol.

Key words

Majorana bound states, Topological Qubits, Superconductor-semiconductor hybrid strucures, Non-abelian physics

Classification system and/or index terms (if any)

Supplementary bibliographical information	Language
	English
ISSN and key title	ISBN
	978-91-8104-749-3 (print) 978-91-8104-750-9 (pdf)
Recipient's notes	Number of pages: 179 / Price
	Security classification

Elementary quantum operations on Majorana systems

by Maximilian Nitsch

LUND
UNIVERSITY

A doctoral thesis at a university in Sweden takes either the form of a single, cohesive research study (monograph) or a summary of research papers (compilation thesis), which the doctoral student has written alone or together with one or several other author(s).

In the latter case the thesis consists of two parts. An introductory text puts the research work into context and summarizes the main points of the papers. Then, the research publications themselves are reproduced, together with a description of the individual contributions of the authors. The research papers may either have been already published or are manuscripts at various stages (in press, submitted, or in draft).

Cover illustration front: Some of my favorite derivations from the past five years, presented both as equations and as graphical illustrations by Ulrike Katrin Küst.

Cover illustration back: The coffee corner at FTF – a place of great science and joy.

Funding information: The thesis work was financially supported by Nanolund, the Swedish Research Council (VR), and the European Research Council (ERC) under the European Union's Horizon 2020 research and innovation programme under Grant Agreement No. 856526.

Division of Solid State Physics
Department of Physics
Faculty of Engineering
Lund University

ISBN: 978-91-8104-749-3 (print)
ISBN: 978-91-8104-750-9 (pdf)

Printed in Sweden by Media-Tryck, Lund University, Lund 2025

Media-Tryck is a Nordic Swan Ecolabel certified provider of printed material. Read more about our environmental work at www.mediatryck.lu.se

MADE IN SWEDEN

Für meine (Groß-)Eltern
Petra – Erich – Anke – Josef

Contents

List of publications

This thesis is based on the following publications, referred to by their Roman numerals:

I **Interference and parity blockade in transport through a Majorana box**

M. Nitsch, R. Seoane Souto, M. Leijnse
Phys. Rev. B 106, L201305

I was the main responsible for developing the theory, the numerical simulations, analytical solutions, and writing the manuscript.

II **Transport-based fusion that distinguishes between Majorana and Andreev bound states**
M. Nitsch, R. Seoane Souto, S. Matern, M. Leijnse
Phys. Rev. B 109, 165404

I was the main responsible for developing the theory, the numerical simulations, and writing the manuscript.

III **Poor Man's Majorana Tetron**

M. Nitsch*, L. Maffi*, V. V. Baran, R. Seoane Souto, J. Paaske, M. Leijnse, M. Burrello
PRX Quantum 6, 030365

*These authors contributed equally

I was one of the two main authors and as such contributed to the writing of the manuscript. I performed the analytical calculations presented in section II - V of the manuscript.

IV **Adiabatic nonabelian braiding of imperfect Majoranas**

M. Nitsch, V. Svensson, W. Samuelson, K. Nestmann, J. Danon, K. Flensberg, R. Seoane Souto, M. Leijnse
arXiv:2507.11039 under review at PRL

I was the main responsible for developing the theory, the analytical solution presented in the paper, and writing the manuscript.

All papers are reproduced with permission of their respective publishers.

Acknowledgements

Academia is wonderful because working at a university, you constantly meet fascinating people with different backgrounds, interests, and talents. But academia is also cruel, as most people will leave again after only a few years.

I usually embrace change with a smile, focusing on the new opportunities it brings. However, now that it is my turn to leave, I can not help but feel a certain melancholy taking hold of me. The last five years at FTF have given my life many ups and downs. I couldn't have found a better place to grow as a researcher and friend. So, I want to take a look back and acknowledge all the people who made this journey worth taking.

I will apply an approach that corresponds to different layers of spheres. The layers determine how closely I worked with people over the years. The same person can lie in different spheres, which makes this only a decent approximation to a high-dimensional problem.

Let's start with my supervisor, Martin, who made this possible by letting me work on this project with him. A few years ago, during my Bachelor's studies, I answered a survey on physics studies at my former university. I clicked through it pretty fast (yes, no, no, yes, ...) and after a short while, I was already at the last question, which made me pause. Loosely translated, it asked if I had 'Any academic role models and if yes, describe what makes them special'. I stared at this question and didn't know what to write. Mentally, I went through the list of people in my department. They were great lecturers, but I couldn't call them my role models. After considering it for a long time, I sent the survey off, leaving this field empty. It felt a bit sad. If I had this question in front of me today, I would just type your name into the keyboard and write an essay about all the great qualities I see in you as a supervisor and person. Of course, you taught me many things about Majoranas and solid state physics, but what I took away from this time goes well beyond that. It is about how to communicate efficiently, order tasks, view research from the perspective of experimentalists, and many more things. Thanks for all the small and big lessons!

Moving on to the people in the research group. Our research group has been rather big, and many nice people have been part of it over the last years. All of them have been great company and deserve my thanks! However, I want to highlight a few people directly involved in my work. Let's start by acknowledging my unofficial co-supervisor, Rubén. You are good at eyeing the big picture and sorting topics across our huge research field. Also, despite moving away from Lund, you always stayed involved with all my projects and contributed to developing them. Chronologically, Steffi was the first colleague I met, and she was also one of the people who left first. You taught me almost everything I know about Quantum master equations. Also, I appreciate your constructive attitude. You call out problems but also stay fair towards everyone, while being fun to spend time with. Thanos, you are so well-organized that we always called you the one true German of the

group. I am unsure if that was a compliment, but you took it. We had a few very honest conversations that helped me re-evaluate my priorities. Thank you for that. Viktor - Gosh, you are smart! No sarcasm here. I only met a few people who grasp new concepts as fast as you do. It was a pleasure discussing Majoranas with you. Last and most important of all, Konstantin. You arrived exactly when I needed a best friend, and you filled the position perfectly. Being with you is so uncomplicated that it feels like we have known each other for a long time. We can talk about essentially anything; you always get me. And you also get excited about the same things, spanning from fancy Maths to Sports. In you, I found a friend who feels like a brother.

Next layer - (PhD) students from FTF! There were lots of special people in our division, and the effort of mentioning all of them would go a bit beyond my print deadline. So, I will restrict it to a selection of special people. We start with Julibu, without whom this division wouldn't be the same place. You are a very balanced person who always tries to keep everyone happy. That is not an easy task at a place full of people with many different interests. Moving on to my favorite dance instructor, Frida, who is so easygoing and fun! It's really hard to put you on the wrong foot about anything. You were also the one who brought me to Gerdahallen and, by that, founded our HIT group. I was really glad about how I got my last office mate, Samuel. The desk next to me was open for only one day before you moved in and took it. That was probably mostly because your previous office spot was not great, but I decided to take it as a compliment. And I wouldn't have asked for anyone else but you. Somehow, we managed to make a spacious two-person office appear small and crowded by grabbing any furniture available. Also, I enjoyed our sneezing contests! Pierre, I want to first thank you again for your bike - what a nice machine! You were easy to hang out with and always up for it when we wanted to organize something. I was very happy for you when you got your permanent position, although it came at the cost of losing you from FTF well before your contract ran out. For just a short but memorable time, our division hosted Pia (not to be confused with the previously mentioned Pierre!). Pictures of this legendary appearance still decorate the B200 hallway. Spending time with you was great fun! You proved that someone can live in Lund for half a year and still doesn't know how to find their way to Botaniska even after visiting it several times. You had to leave too soon again, and I speak for many when I say that we miss you. Let's finalize with Ruby and David, who always inspired me by being their authentic selves.

We move on to the senior people at FTF. What feels special about our division is that it has very flat hierachies. Titles and positions don't mean anything in everyday interactions. Here I want to highlight Ville (my co-supervisor) and Jason, who are always up for a chat about any topic. Also, I appreciated talking to Dan, Christelle, Adam, and Peter (not FTF, but close enough). What you all have in common is that you are very open and approachable. I had many easy-going conversations with all of you, but also talked about serious topics and sometimes even problems, which requires trust.

Beyond the research staff, there is a large group of administrators and lab technicians making all of the great research possible. I want to highlight Alex and Anna-Karin in particular. You two were always very nice and helpful in fixing any issue. In my five years at FTF, I only entered the Nanolab once on a lab tour (thanks for the tour, Luke!). Therefore, the technicians didn't really influence my work. However, I still got to know a few of you during chats in the coffee breaks and appreciated the funny atmosphere of those gatherings. In particular, I want to highlight Håkan, who is always in a good mood and makes many jokes! Also, I want to thank Emil for helping me mark my mug as my 'favorite mug'!

Let's go one step further and expand to friends outside of FTF. Yes, I actually went through the effort of making friends from other research divisions! We start with Sandra, whom I met first. You were my first friend at the synchrotron division, and I still vividly remember our first conversation at the Ven student retreat. That you moved away so fast was one of the first times I really experienced that sad side of academia. Thanks to Sandra, I met Alfred and Ulrike. Synchrotron is full of nice people, but I decided to highlight you two. The group around you was always so fun and open. I was very glad to join your many activities. Next, Marcus, it was always great fun visiting you for lunch! Vi avslutar med Emma. Tack för hjälpen med att förbättra min svenska. Det var du och jag som startade lunch på svenska, som fortfarande äger rum varje vecka. Efter att du lämnade universitetet tog Charlotta över som språkpolis, och hon sköter jobbet jättebra!

With that, we close the university chapter and go beyond, starting with Sofia. Meeting you felt like such an unlikely coincidence (thanks, Aleks!). Every shared weekend with you was a much-needed break during the months of writing. Those days helped me recharge and come back to the manuscript with new energy — always motivated to get things done efficiently and return to the weekend. Thank you for helping me through this. I am looking forward to returning the favour when it's your turn to write your thesis.

Abschließend möchte ich mich nach Hause wenden und meinen Freunden und meiner Familie danken. Die Entscheidung, für meine Doktorarbeit nach Schweden zu ziehen, hat mich räumlich von euch entfernt. Durch die Distanz gehen unweigerlich manche Dinge verloren, und ich habe zweifellos einige besondere Momente zu Hause verpasst. Gleichzeitig konntet auch ihr nicht an allem teilhaben, was ich in dieser Zeit erlebt habe. Dennoch blicke ich auf die letzten Jahre zurück und erinnere mich an viele schöne Momente, die wir geteilt haben. Gerade dass die gemeinsame Zeit so viel seltener ist und mehr Planung erfordert, steigert die Wertschätzung für diese Augenblicke. Dass so viele von euch den langen Weg nach Lund auf sich nehmen, um meine Doktorverteidigung mit mir zu teilen, ist nicht selbstverständlich und bedeutet mir sehr viel.

Abstract

This thesis aims to investigate the novel physics around Majorana bound states (MBSs). MBSs are quasiparticle excitations predicted to exist in topological superconductors. Due to the inherent protection they obtain from their topology, they have long been regarded as a promising setup to build a topologically protected quantum computer. Apart from this very practical application, they continue to fascinate as platforms built with MBS exhibit unique effects like nonabelian braiding and non-Fermi liquid behaviour in the topological Kondo effect.

The thesis starts with a general introduction to quantum computing, highlighting both the promises and challenges of that field. Afterwards follows an introduction to systems that are candidates to host MBSs. It focuses on the theoretical proposals and experimental realizations that are most relevant to the presented work. We continue with a summary of the most fundamental effects and the setups that make the physics of MBSs accessible.

The author's contributions in this field are theoretical. However, each publication comes with the explicit goal of investigating setups that make the unique physics of MBSs directly accessible in experiments. The first three papers have been peer-reviewed and were published in scientific journals. The fourth one is currently under peer review. The first two papers investigate DC transport setups connecting to a qubit based on MBSs called the MBS tetron. We show that via an effect called parity blockade, it is possible to initialize the qubit, quantify its lifetime, and determine whether it holds MBSs or trivial (normal fermionic) states. Also employing parity blockade, the second paper establishes a transport setup that enables access to MBS fusion rules, an effect directly related to nonabelian braiding. The third paper translates the concept of a MBS tetron into the newly experimentally established approach of MBSs in quantum dot-based Kitaev chains. We denote this system the poor man's Majorana tetron. We find that the poor man's Majorana tetron in a transport setup with appropriate tuning exhibits the famed topological Kondo effect. Paper IV focuses on nonabelian braiding. It investigates the hybridization-based braiding protocol and accounts for imperfections in MBS localization, breaking the ground state degeneracy. This detrimental effect is corrected by the introduction of a correction term, followed by a full analytical solution of the transformation induced by this generalized braiding protocol.

Popular summary in English - How to be a good qubit

A qubit called Maji walks across a wonderfully smooth and clean semiconductor surface on a lovely, chilly day inside the dilution fridge. Maji is in a great mood because he will meet his friends. His friends are also qubits, and they meet regularly to spend time together. But despite his high spirit, he is also a bit nervous, because although he loves and respects his friends, these meetings can be somewhat competitive. They are all unique qubits based on different physical setups and have very different appearances and skills. But every qubit wants to be the best qubit. Where 'best' is sometimes a bit hard to define.

To get an idea of what society demands of a good qubit, we need to take a step back and examine its common characteristics. Every qubit has two quantum states $|0\rangle$ and $|1\rangle$. But unlike their distant relatives, the classical bits, they don't have to be in the state $|0\rangle$ or in the state $|1\rangle$. Qubits can be in any combined quantum state $|\psi\rangle = \alpha\,|0\rangle + \beta\,|1\rangle$. This is exactly what makes them so special, so the first thing a good qubit should have is two quantum states. Maji is sometimes unsure if it is indeed only two states he carries, or maybe even four or eight, and people are a bit sceptical about qubits with more than two states. Maji would be very happy to find definite proof that he indeed has exactly two quantum states.

Next, people expect a qubit to have a stable state. If it starts out in a state $|\psi\rangle$, it should stay in $|\psi\rangle$ as long as possible, which is denoted as the qubit lifetime. Maji hopes that he will neither experience bit flips ($|0\rangle \leftrightarrow |1\rangle$) or phase flips ($|0\rangle + |1\rangle \leftrightarrow |0\rangle - |1\rangle$), but he doesn't know yet and he is not sure if he will live up to the expectations.

Apart from having a stable state, as a good qubit, researchers should be able to determine and change your quantum state on purpose. It is called performing measurements and quantum gates on a qubit and is measured in fidelity, which is a value between 0 and 1. A fidelity of around 1 means that measurements and intended gate changes are achieved with an accuracy close to 100 percent, while 0 means that there is almost no reliable control over the quantum state. A very high fidelity, even bigger than 0.99, is necessary for qubits to run quantum algorithms reliably. And running quantum algorithms is what every qubit eventually wants to do. About the measurement part, Maji is optimistic that he will figure it out. It is the changing of the state that challenges him. Maji is trying to learn a trick called braiding. It is a very unique way to perform some of his gates, which only he can do. If he could manage that, people would be very impressed! But despite lots of practice and many different ideas on how to braid, he hasn't found a way to perform it yet.

Last, a good qubit should be able to work together with other qubits. As a single qubit, you cannot achieve much. It is in a team of like-minded qubits, which together perform calculations that classical bits wouldn't be able to do. Maji hasn't gotten to that point yet. He very much feels that he should focus on learning to work by himself before trying to

combine into a bigger setup with other qubits like him.

At this point, Maji has almost arrived at the meeting point, and his excitement is going up. There are his friends! First, he spots the superconducting qubit. Lately, she has received lots of attention. People are very excited because she and other superconducting qubits work at IBM and Google. There, they are already building large clusters of hundreds and thousands of qubits, which perform first quantum circuits and even already start implementing logical qubits. Maji also can't help but feel impressed by this. But he knows the way to a fully functional general quantum computer is still long, even for superconducting qubits.

Next to her stands the trapped-ion qubit. Also, he already has a pretty impressive career. Many small companies believe in the abilities of trapped-ion qubits. And why not? They have amazingly stable states! Their gate times are a bit slow, and they don't manage to scale to as large numbers of qubits as the superconducting clusters, but that might be fixed with a bit of development.

Maji likes hanging out with his best friend, spin qubit. They are the only one who have a clear idea of what it is to be in a spatially spread out quantum state. Also, they are more academic than the others with their industry careers, and Maji still feels very much like an academic.

After a while, everyone is talking about their latest results. Who got which fidelity, and how fast can they perform their gates?! Maji is having a great time! Milliseconds turn into seconds, and soon it is already time to call it a day. At the end, they agree to soon meet again and have more fun. On the way home, Maji thinks about how exciting it is to be a qubit at this time. There are new ideas and approaches all the time, and also for qubits like him, decade-old theories can finally be tested and improved by new concepts. He can't help but feel optimistic about the future of quantum computing.

Maji is an example of a Majorana qubit. This qubit is based on a concept going back to the Italian physicist Ettore Majorana. He introduced Majoranas in the first half of the 20th century in the field of particle physics as an example of an exotic particle that is its own antiparticle. Many decades later, at the beginning of the 2000s, Alexei Kitaev introduced the famous Kitaev chain. A theoretical model predicting the existence of Majoranas as quasiparticles in an exotic material called a topological superconductor. It was one of the earliest setups that translated the particle physics concept of a Majorana into the field of condensed matter physics.

The core idea behind Majoranas in a topological superconductor is that they always come in pairs of two. Together, they describe the degree of freedom of one fermion inside the system. Fermions are a specific class of quantum particles. The electron is one of the most

well-known members of the class of fermions. The topology forces these two Majoranas to localize at opposite ends of the Kitaev chain, making the fermion truly nonlocal. This spatial separation then protects the quantum state from local electric or magnetic fields. These fields cannot interact with a single Majorana, as it is not a full fermionic degree of freedom. Thanks to this mechanism, the quantum information saved in such a nonlocal fermion is topologically protected against external disturbances, making these qubits potentially very stable.

Right at the introduction of the Kitaev chain, there was a challenge. There were no well-understood materials that combined all physical mechanisms used in the model. The following two decades were full of theoretical proposals making Majoranas more accessible on different platforms and experimental setups, aiming at realizing the required combinations of ingredients. One particularly noteworthy class of experimental setups were the superconductor-semiconductor hybrid structures. They come in many different variations. One possible version is a semiconducting nanowire wrapped with a thin layer of superconducting material. These superconductor-semiconductor hybrid structures were some of the earliest systems that combined all the necessary ingredients required by the Kitaev chain.

Around the same time, many concepts for Majorana qubits were developed - Maji had finally arrived. And he came in many different designs. One version of it, called the Majorana tetron, combines two of the previously mentioned nanowires into a box hosting a total of four Majoranas. The thus obtained system holds two states defining the computational space of the qubit. The first two papers of this thesis are theoretical investigations of experimental methods to work with these qubits via quantum transport. This essentially means running an electric current through the system and measuring the response as a function of experimental parameters. We found methods to initialize qubits, determine their lifetime, and also distinguish whether it is indeed only four Majoranas with two states or if the qubit holds different states that are not useful for topological qubits.

Finding clear evidence for topological Majoranas instead of different, less useful states is one of the big challenges that this research field faces. In particular, calling the previously mentioned superconductor-semiconductor nanowires 'topological' is highly controversial, as the experimental signatures are inconclusive.

As a possible solution to this issue, over the last three years, a new approach was developed thanks to pioneering work from several groups at Delft University. In this approach, experimentalists artificially construct the Kitaev chain via quantum dots. Quantum dots are nanoscale structures, with a size of hundreds of nanometers (10^{-9} m), that restrict the spatial freedom of fermions so much that at low temperatures the system is effectively 0-dimensional. This means that the fermions are fixed in space and can't move in any direction on that quantum dot. The Delft researchers combined several of these quantum dots with tunable special connections such that fermions can travel between the quantum

dots and thereby replicate the behaviour of the Kitaev chain.

The other two papers of this thesis were also theoretical and explicitly motivated by these experimental achievements. In the first paper, we take the previous design of a Majorana tetron and construct an equivalent system via the quantum dot-based Kitaev chain of Delft. This system doesn't promise to be a great qubit, but we show that it still exhibits the so-called topological Kondo effect. A transport signature unique to Majorana systems. In the second paper, we looked at new possibilities of braiding Majoranas. Braiding means controlled spatial exchanges of Majoranas and is the reason why these systems are called nonabelian. Exchanging the position of two Majoranas has a non-trivial effect on the wavefunction, which is fundamentally different from abelian quantum particles like fermions. We took one of the existing braiding protocols and showed that it can be generalized to having imperfect Majoranas that are not fully spatially separated. The spatial separation is one of the key features distinguishing Majoranas from fermions. With this generalization, we opened a door to investigating the fundamental difference between Majoranas and fermions.

Populärwissenschaftliche Zusammenfassung auf Deutsch – Wie man ein guter Qubit wird

Ein Qubit namens Maji läuft an einem schönen, kühlen Tag im Kryostat über eine wunderbar glatte und saubere Halbleiteroberfläche. Maji ist gut gelaunt, weil er seine Freunde treffen wird. Seine Freunde sind ebenfalls Qubits, und sie treffen sich regelmäßig, um Zeit miteinander zu verbringen. Doch trotz seiner guten Laune ist er auch ein wenig nervös, denn obwohl er seine Freunde liebt und respektiert, können diese Treffen etwas kompetitiv sein. Sie sind alle einzigartige Qubits, die auf unterschiedlichen physikalischen Konfigurationen basieren und sehr unterschiedliche Erscheinungsbilder und Fähigkeiten haben. Aber jedes Qubit möchte das beste Qubit sein. Dabei ist „das Beste" manchmal etwas schwer zu definieren.

Um eine Vorstellung davon zu bekommen, was die Gesellschaft von einem guten Qubit erwartet, müssen wir einen Schritt zurücktreten und deren algemeinen Eigenschaften untersuchen. Jedes Qubit hat zwei Quantenzustände $|0\rangle$ und $|1\rangle$. Aber im Gegensatz zu ihren entfernten Verwandten, den klassischen Bits, müssen sie sich nicht im Zustand $|0\rangle$ oder im Zustand $|1\rangle$ befinden. Qubits können sich in jedem kombinierten Quantenzustand $|\psi\rangle = \alpha\,|0\rangle + \beta\,|1\rangle$ befinden. Genau das macht sie so besonders, daher sollte ein gutes Qubit als Erstes zwei Quantenzustände haben. Maji ist sich manchmal nicht sicher, ob er tatsächlich nur zwei Zustände hat oder vielleicht sogar vier oder acht, und die Leute sind etwas skeptisch gegenüber Qubits mit mehr als zwei Zuständen. Maji würde sich sehr freuen, einen eindeutigen Beweis dafür zu finden, dass er tatsächlich genau zwei Quantenzustände hat.

Als Nächstes erwarten die Menschen, dass ein Qubit einen stabilen Zustand hat. Wenn es in einem Zustand $|\psi\rangle$ beginnt, sollte es so lange wie möglich in $|\psi\rangle$ bleiben, was als Qubit-Lebensdauer bezeichnet wird. Maji hofft, dass er weder Bitflips ($|0\rangle \leftrightarrow |1\rangle$) noch Phasenflips ($|0\rangle + |1\rangle \leftrightarrow |0\rangle - |1\rangle$) erleben wird, aber er weiß es noch nicht und ist sich nicht sicher, ob er die Erwartungen erfüllen wird.

Abgesehen von einem stabilen Zustand sollten Forscher bein einem guten Qubit in der Lage sein, dessen Quantenzustand gezielt zu bestimmen und zu verändern. Dies wird als Durchführung von Messungen und Quantengattern an einem Qubit bezeichnet und in der Fidelity gemessen, einem Wert zwischen 0 und 1. Eine Fidelity von etwa 1 bedeutet, dass Messungen und beabsichtigte Gatteränderungen mit einer Genauigkeit von nahezu 100 Prozent erreicht werden, während 0 bedeutet, dass es fast keine zuverlässige Kontrolle über den Quantenzustand gibt. Eine sehr hohe Fidelity, sogar größer als 0,99, ist notwendig, damit Qubits Quantenalgorithmen zuverlässig ausführen können. Und die Ausführung von Quantenalgorithmen ist das, was jedes Qubit letztendlich tun möchte. Was den Messungsaspekt angeht, ist Maji optimistisch, dass er eine Lösung finden wird. Die Herausforderung

für ihn liegt in der Veränderung des Zustands. Maji versucht, einen Trick namens „Braiding" zu erlernen. Dabei handelt es sich um eine sehr einzigartige Methode zur Ausführung einiger seiner Gatter, die nur er beherrscht. Wenn er das schaffen würde, wären die Leute sehr beeindruckt! Aber trotz viel Übung und vielen verschiedenen Ideen zum Braiding hat er noch keinen Weg gefunden, dies umzusetzen.

Schließlich sollte ein gutes Qubit in der Lage sein, mit anderen Qubits zusammenzuarbeiten. Als einzelnes Qubit kann man nicht viel erreichen. Erst in einem Team gleichgesinnter Qubits, die gemeinsam Berechnungen durchführen, die klassische Bits nicht leisten könnten. Maji ist noch nicht so weit. Er ist der festen Überzeugung, dass er sich darauf konzentrieren sollte, selbstständig zu arbeiten, bevor er versucht, sich mit anderen Qubits wie ihm zu einem größeren System zusammenzuschließen.

Mittlerweile ist Maji fast am Treffpunkt angekommen und seine Aufregung steigt. Da sind seine Freunde! Als erstes entdeckt er das supraleitende Qubit. In letzter Zeit hat sie viel Aufmerksamkeit erhalten. Die Leute sind sehr begeistert, weil sie und andere supraleitende Qubits bei IBM und Google arbeiten. Dort bauen sie bereits große Cluster aus Hunderten und Tausenden von Qubits, die erste Quantenschaltungen ausführen und sogar schon mit der Implementierung logischer Qubits beginnen. Auch Maji ist davon beeindruckt. Aber er weiß, dass der Weg zu einem voll funktionsfähigen allgemeinen Quantencomputer noch lang ist, selbst für supraleitende Qubits.

Neben ihr steht das Ionen-Qubit. Auch er kann bereits auf eine beeindruckende Karriere zurückblicken. Viele kleine Unternehmen glauben an die Fähigkeiten von Ionen-Qubits. Und warum auch nicht? Sie haben erstaunlich stabile Zustände! Ihre Gate-Zeiten sind etwas langsam, und sie schaffen es nicht, auf so viele Qubits zu skalieren wie die supraleitenden Cluster, aber das könnte mit ein wenig Entwicklung behoben werden.

Maji verbringt gerne Zeit mit seinem besten Freund, dem Spin-Qubit. Sie sind die einzigen, die eine klare Vorstellung davon haben, was es bedeutet, sich in einem räumlich ausgedehnten Quantenzustand zu befinden. Außerdem sind sie akademischer als die anderen mit ihren Karrieren in der Industrie, und Maji fühlt sich immer noch sehr wie ein Akademiker.

Nach einer Weile sprechen alle über ihre neuesten Ergebnisse. Wer hat welche Genauigkeit erreicht und wie schnell können sie ihre Gates ausführen? Maji hat viel Spaß! Millisekunden werden zu Sekunden, und schon bald ist es Zeit, für heute Schluss zu machen. Am Ende vereinbaren sie, sich bald wieder zu treffen und weiter Spaß zu haben. Auf dem Heimweg denkt Maji darüber nach, wie aufregend es ist, in dieser Zeit ein Qubit zu sein. Es gibt ständig neue Ideen und Ansätze, und auch für Qubits wie ihn können jahrzehntealte Theorien endlich durch neue Konzepte getestet und verbessert werden. Er kann nicht anders, als optimistisch in die Zukunft des Quantencomputings zu blicken.

Maji ist ein Beispiel für ein Majorana-Qubit. Dieses Qubit basiert auf einem Konzept, das auf den italienischen Physiker Ettore Majorana zurückgeht. Er führte Majoranas in der ersten Hälfte des 20. Jahrhunderts im Bereich der Teilchenphysik als Beispiel für ein exotisches Teilchen ein, das sein eigenes Antiteilchen ist. Viele Jahrzehnte später, zu Beginn der 2000er Jahre, stellte Alexei Kitaev die berühmte Kitaev-Kette vor. Ein theoretisches Modell, das die Existenz von Majoranas als Quasiteilchen in einem exotischen Material namens topologischer Supraleiter vorhersagt. Es war eines der frühesten Modelle, die das Teilchenphysikkonzept eines Majorana in den Bereich der Physik der kondensierten Materie übertrug.

Die Kernidee hinter Majoranas in einem topologischen Supraleiter ist, dass sie immer paarweise auftreten. Zusammen beschreiben sie den Freiheitsgrad eines Fermions innerhalb des Systems. Fermionen sind eine bestimmte Klasse von Quantenteilchen. Das Elektron ist eines der bekanntesten Mitglieder der Klasse der Fermionen. Die Topologie zwingt diese beiden Majoranas, sich an den entgegengesetzten Enden der Kitaev-Kette zu lokalisieren, wodurch das Fermion nichtlokal wird. Diese räumliche Trennung schützt den Quantenzustand dann vor lokalen elektrischen oder magnetischen Feldern. Diese Felder können nicht mit einem einzelnen Majorana interagieren, da es sich nicht um einen vollständigen fermionischen Freiheitsgrad handelt. Dank dieses Mechanismus ist die in einem solchen nichtlokalen Fermion gespeicherte Quanteninformation topologisch vor äußeren Störungen geschützt, wodurch diese Qubits potenziell sehr stabil sind.

Gleich bei der Einführung der Kitaev-Kette gab es eine Herausforderung. Es gab keine gut verstandenen Materialien, die alle im Modell verwendeten physikalischen Mechanismen kombinierten. Die folgenden zwei Jahrzehnte waren voller theoretischer Vorschläge, die Majoranas auf verschiedenen Plattformen und in verschiedenen Versuchsaufbauten zugänglicher machten, mit dem Ziel, die erforderlichen Kombinationen von Bestandteilen zu realisieren. Eine besonders bemerkenswerte Klasse von Versuchsaufbauten waren die Hybridstrukturen aus Supraleiter und Halbleiter. Es gibt sie in vielen verschiedenen Varianten. Eine mögliche Version ist ein halbleitender Nanodraht, der mit einer dünnen Schicht aus supraleitendem Material ummantelt ist. Diese Hybridstrukturen aus Supraleiter und Halbleiter gehörten zu den frühesten Systemen, die alle notwendigen Bestandteile der Kitaev-Kette kombinierten.

Etwa zur gleichen Zeit wurden viele Konzepte für Majorana-Qubits entwickelt – Maji war endlich da. Und er kam in vielen verschiedenen Ausführungen. Eine Version davon, das sogenannte Majorana-Tetron, kombiniert zwei der zuvor erwähnten Nanodrähte zu einer Box, die insgesamt vier Majoranas beherbergt. Das so erhaltene System enthält zwei Zustände, die die Rechenzustände des Qubits definieren. Die ersten beiden Artikel dieser Arbeit sind theoretische Untersuchungen zu experimentellen Methoden, um mit diesen Qubits

über Quantentransport zu arbeiten. Das bedeutet im Wesentlichen, dass ein elektrischer Strom durch das System geleitet und die Reaktion als Funktion der experimentellen Parameter gemessen wird. Wir haben Methoden gefunden, um Qubits zu initialisieren, ihre Lebensdauer zu bestimmen und auch zu unterscheiden, ob es sich tatsächlich nur um vier Majoranas mit zwei Zuständen handelt oder ob das Qubit verschiedene Zustände aufweist, die für topologische Qubits nicht nützlich sind.

Eindeutige Beweise für topologische Majoranas anstelle von anderen, weniger nützlichen Zuständen zu finden, ist eine der großen Herausforderungen, denen sich dieses Forschungsgebiet gegenübersieht. Insbesondere die Bezeichnung der zuvor erwähnten Supraleiter-Halbleiter-Nanodrähte als „topologisch" ist höchst umstritten, da die experimentellen Signaturen nicht eindeutig sind.

Als mögliche Lösung für dieses Problem wurde in den letzten drei Jahren dank der Pionierarbeit mehrerer Gruppen an der Universität Delft ein neuer Ansatz entwickelt. Bei diesem Ansatz konstruieren Experimentalphysiker die Kitaev-Kette künstlich mithilfe von Quantenpunkten. Quantenpunkte sind nanoskalige Strukturen mit einer Größe von einigen hundert Nanometern (10^{-9} m), die die räumliche Freiheit von Fermionen so stark einschränken, dass das System bei niedrigen Temperaturen effektiv 0-dimensional ist. Das bedeutet, dass die Fermionen im Raum fixiert sind und sich auf diesem Quantenpunkt nicht in irgendeine Richtung bewegen können. Die Forscher aus Delft kombinierten mehrere dieser Quantenpunkte mit abstimmbaren speziellen Verbindungen, sodass Fermionen zwischen den Quantenpunkten wandern und so das Verhalten der Kitaev-Kette nachbilden können.

Die beiden anderen Arbeiten dieser Dissertation waren ebenfalls theoretischer Natur und ausdrücklich durch diese experimentellen Erfolge motiviert. In der ersten Arbeit nehmen wir das bisherige Design eines Majorana-Tetrons und konstruieren ein äquivalentes System über die auf Quantenpunkten basierende Kitaev-Kette von Delft. Dieses System verspricht zwar kein großartiges Qubit zu sein, aber wir zeigen, dass es dennoch den sogenannten topologischen Kondo-Effekt aufweist. Eine für Majorana-Systeme einzigartige Transportsignatur. In der zweiten Arbeit haben wir uns mit neuen Möglichkeiten des Braidings von Majoranas befasst. Braiding bedeutet den kontrollierten räumlichen Austausch von Majoranas und ist der Grund, warum diese Systeme als nicht-abelsch bezeichnet werden. Der Austausch der Position zweier Majoranas hat einen nicht trivialen Effekt auf die Wellenfunktion, was sich grundlegend von abelschen Quantenteilchen wie Fermionen unterscheidet. Wir haben eines der bestehenden Braiding-Protokolle genommen und gezeigt, dass es auf unperfekte Majoranas verallgemeinert werden kann, die nicht vollständig räumlich getrennt sind. Die räumliche Trennung ist eines der Hauptmerkmale, das Majoranas von Fermionen unterscheidet. Mit dieser Verallgemeinerung haben wir eine Tür geöffnet, um den grundlegenden Unterschied zwischen Majoranas und Fermionen zu untersuchen.

Populärvetenskaplig sammanfattning på svenska – Hur man är en bra kvantbit

En kvantbit som heter Maji går över en underbart slät och ren halvledaryta på en härlig, kylig dag inne i kryostaten. Maji är på gott humör eftersom han ska träffa sina vänner. Hans vänner är också kvantbitar, och de träffas regelbundet för att umgås. Men trots sitt goda humör är han också lite nervös, för även om han älskar och respekterar sina vänner kan dessa möten vara något konkurrenspräglade. De är alla unika kvantbitar baserade på olika fysiska uppställningar och har mycket olika utseende och färdigheter. Men varje kvantbit vill vara den bästa kvantbiten. Där ”bäst” ibland är lite svårt att definiera.

För att få en uppfattning om vad samhället kräver av en bra kvantbit måste vi ta ett steg tillbaka och undersöka dess gemensamma egenskaper. Varje kvantbit har två kvanttillstånd $|0\rangle$ och $|1\rangle$. Men till skillnad från sina avlägsna släktingar, de klassiska bitarna, behöver de inte befinna sig i tillståndet $|0\rangle$ eller i tillståndet $|1\rangle$. Kvantbitar kan befinna sig i vilket kombinerat kvanttillstånd som helst $|\psi\rangle = \alpha\,|0\rangle + \beta\,|1\rangle$. Det är just detta som gör dem så speciella, så det första en bra kvantbit bör ha är två kvanttillstånd. Maji är ibland osäker på om det verkligen bara är två tillstånd han bär på, eller kanske till och med fyra eller åtta, och folk är lite skeptiska till kvantbitar med fler än två tillstånd. Maji skulle bli mycket glad om han kunde hitta definitiva bevis för att han verkligen har exakt två kvanttillstånd.

Dessutom förväntar sig folk att en kvantbit ska ha ett stabilt tillstånd. Om den börjar i tillståndet $|\psi\rangle$ bör den stanna kvar i $|\psi\rangle$ så länge som möjligt, vilket betecknas som kvantbitens livslängd. Maji hoppas att han varken kommer att uppleva bitflips ($|0\rangle \leftrightarrow |1\rangle$) eller fasflips ($|0\rangle + |1\rangle \leftrightarrow |0\rangle - |1\rangle$), men han vet inte ännu och är osäker på om han kommer att leva upp till förväntningarna.

Förutom att ha ett stabilt tillstånd, som en bra kvantbit, bör forskare kunna bestämma och ändra ditt kvanttillstånd medvetet. Det kallas att utföra mätningar och kvantportar på en kvantbit och mäts i fidelitet, vilket är ett värde mellan 0 och 1. En fidelitet på cirka 1 innebär att mätningar och avsedda portförändringar uppnås med en noggrannhet nära 100 procent, medan 0 innebär att det nästan inte finns någon tillförlitlig kontroll över kvanttillståndet. En mycket hög fidelitet, till och med större än 0,99, är nödvändig för att kvantbitar ska kunna utföra kvantalgoritmer på ett tillförlitligt sätt. Och att köra kvantalgoritmer är vad varje kvantbit i slutändan vill göra. När det gäller mätningsdelen är Maji optimistisk och tror att han kommer att lösa det. Det är förändringen av tillståndet som utmanar honom. Maji försöker lära sig ett trick som kallas braiding. Det är ett mycket unikt sätt att utföra vissa av hans portar, som bara han kan göra. Om han kunde klara det skulle folk bli mycket imponerade! Men trots mycket övning och många olika idéer om hur man utföra braiding har han ännu inte hittat ett sätt att utföra det.

Slutligen bör en bra kvantbit kunna samarbeta med andra kvantbitar. Som en enskild kvant-

bit kan man inte åstadkomma mycket. Det är i ett team av likasinnade kvantbitar som tillsammans utför beräkningar som klassiska bitar inte skulle kunna göra. Maji har inte kommit så långt ännu. Han känner starkt att han bör fokusera på att lära sig att arbeta själv innan han försöker kombinera sig till en större enhet med andra kvantbitar som han.

Vid det här laget har Maji nästan kommit fram till mötesplatsen, och hans spänning stiger. Där är hans vänner! Först ser han den supraledande kvantbiten. På senare tid har hon fått mycket uppmärksamhet. Folk är mycket uppspelta eftersom hon och andra supraledande kvantbitar arbetar hos IBM och Google. Där bygger de redan stora kluster med hundratals och tusentals kvantbitar, som utför de första kvantkretsarna och till och med redan har börjat implementera logiska kvantbitar. Maji kan inte undvika att bli imponerad av detta. Men han vet att vägen till en fullt fungerande allmän kvantdator fortfarande är lång, även för supraledande kvantbitar.

Bredvid henne står den fångade jon-kvantbiten. Han har också redan en ganska imponerande karriär. Många små företag tror på de fångade jonqubiternas förmågor. Och varför inte? De har otroligt stabila tillstånd! Deras porttider är lite långsamma, och de klarar inte av att skala upp till lika stora antal kvantbitar som de supraledande klustren, men det kan kanske åtgärdas med lite utveckling.

Maji gillar att umgås med sin bästa vän, spin-kvantbiten. De är de enda som har en klar uppfattning om vad det innebär att befinna sig i ett rumsligt utspritt kvanttillstånd. Dessutom är de mer akademiska än de andra med sina karriärer inom industrin, och Maji känner sig fortfarande mycket akademisk.

Efter ett tag pratar alla om sina senaste resultat. Vem fick vilken trohet, och hur snabbt kan de utföra sina portar?! Maji har jättekul! Millisekunder blir sekunder, och snart är det redan dags att avsluta dagen. I slutet kommer de överens om att snart träffas igen och ha mer kul. På vägen hem tänker Maji på hur spännande det är att vara en kvantbit just nu. Det dyker hela tiden upp nya idéer och tillvägagångssätt, och även för kvantbitar som honom kan gamla teorier äntligen testas och förbättras med hjälp av nya koncept. Han kan inte låta bli att känna sig optimistisk inför framtiden för kvantdatorer.

Maji är ett exempel på en Majorana-kvantbit. Denna kvantbit baseras på ett koncept som går tillbaka till den italienska fysikern Ettore Majorana. Han introducerade Majoranas under första hälften av 1900-talet inom partikelfysiken som ett exempel på en exotisk partikel som är sin egen antipartikel. Många decennier senare, i början av 2000-talet, introducerade Alexei Kitaev den berömda Kitaevkedjan. En teoretisk modell som förutsäger existensen av Majoranas som kvantpartiklar i ett exotiskt material som kallas topologisk supraledare. Det var en av de tidigaste uppställningarna som översatte partikelfysikens koncept av en Majorana till området kondenserad materiafysik.

Kärnidén bakom Majoranas i en topologisk supraledare är att de alltid förekommer i par om två. Tillsammans beskriver de frihetsgraden för en fermion inuti systemet. Fermioner är en specifik klass av kvantpartiklar. Elektronen är en av de mest kända medlemmarna i klassen av fermioner. Topologin tvingar dessa två Majoranas att lokaliseras i motsatta ändar av Kitaevkedjan, vilket gör fermionen icke-lokal. Denna rumsliga separation skyddar sedan kvanttillståndet från lokala elektriska eller magnetiska fält. Dessa fält kan inte interagera med en enskild Majorana, eftersom den inte är en fullständig fermionisk frihetsgrad. Tack vare denna mekanism är kvantinformationen som lagras i en sådan icke-lokal fermion topologiskt skyddad mot yttre störningar, vilket gör dessa kvantbitar potentiellt mycket stabila.

Redan vid introduktionen av Kitaevkedjan fanns det en utmaning. Det fanns inga välkända material som kombinerade alla fysiska mekanismer som användes i modellen. De följande två decennierna var fyllda av teoretiska förslag som gjorde Majoranas mer tillgängliga på olika plattformar och experimentella uppställningar, i syfte att realisera de nödvändiga kombinationerna av ingredienser. En särskilt anmärkningsvärd klass av experimentella uppställningar var hybridstrukturerna av supraledare och halvledare. De finns i många olika varianter. En möjlig version är en halvledande nanotråd omsluten av ett tunt lager av supraledande material. Dessa hybridstrukturer av supraledare och halvledare var några av de tidigaste systemen som kombinerade alla nödvändiga ingredienser som krävdes av Kitaevkedjan.

Ungefär samtidigt utvecklades många koncept för Majorana-kvantbitar – Maji hade äntligen kommit. Och han kom i många olika utföranden. En version av den, kallad Majoranatetron, kombinerar två av de tidigare nämnda nanotrådarna i en låda som rymmer totalt fyra Majoranas. Det därmed erhållna systemet har två tillstånd som definierar kvantbitens beräkningsutrymme. De två första artiklarna i denna avhandling är teoretiska undersökningar av experimentella metoder för att arbeta med dessa kvantbitar via kvanttransport. Detta innebär i huvudsak att man leder en elektrisk ström genom systemet och mäter responsen som en funktion av experimentella parametrar. Vi fann metoder för att initialisera kvantbitar, bestämma deras livslängd och även skilja på om det verkligen bara är fyra Majoranas med två tillstånd eller om kvantbiten har olika tillstånd som inte är användbara för topologiska kvantbitar.

Att hitta tydliga bevis för topologiska Majoranas istället för olika, mindre användbara tillstånd är en av de stora utmaningarna som detta forskningsområde står inför. I synnerhet är det mycket kontroversiellt att kalla de tidigare nämnda superledande halvledande nanotrådarna för ”topologiska”, eftersom de experimentella resultaten är oklara.

Som en möjlig lösning på detta problem har en ny metod utvecklats under de senaste tre åren tack vare banbrytande arbete från flera grupper vid Delft University. I denna metod konstruerar experimentella forskare artificiellt Kitaevkedjan via kvantprickar. Kvantprickar

är strukturer i nanoskala, med en storlek på hundratals nanometer (10^{-9} m), som begränsar fermionernas rumsliga frihet så mycket att systemet vid låga temperaturer i praktiken är 0-dimensionellt. Detta innebär att fermionerna är fixerade i rymden och inte kan röra sig i någon riktning på den kvantpricken. Forskarna i Delft kombinerade flera av dessa kvantprickar med justerbara specialanslutningar så att fermioner kan röra sig mellan kvantprickarna och därmed replikera Kitaevkedjans beteende.

De andra två artiklarna i denna avhandling var också teoretiska och uttryckligen motiverade av dessa experimentella resultat. I den första artikeln tar vi den tidigare designen av en Majorana-tetron och konstruerar ett motsvarande system via Delfts kvantpunktbaserade Kitaevkedja. Detta system lovar inte att bli en fantastisk kvantbit, men vi visar att det fortfarande uppvisar den så kallade topologiska Kondoeffekten. En transportsignatur som är unik för Majoranasystem. I den andra artikeln tittade vi på nya möjligheter att utföra braiding på Majoranas. Braiding innebär kontrollerade rumsliga utbyten av Majoranas och är anledningen till att dessa system kallas icke-abeliska. Att byta position mellan två Majoranas har en icke-trivial effekt på vågfunktionen, vilket skiljer sig fundamentalt från abelska kvantpartiklar som fermioner. Vi tog ett av de befintliga flätningsprotokollen och visade att det kan generaliseras till att ha ofullkomliga Majoranas som inte är helt rumsligt separerade. Den rumsliga separationen är en av de viktigaste egenskaperna som skiljer Majoranas från fermioner. Med denna generalisering öppnade vi en dörr för att undersöka den grundläggande skillnaden mellan Majoranas och fermioner.

Introduction

1 The need for growing computational resources

Moores' law states that the density of microprocessors doubles every 18 months, leading to an exponential increase of available computing power [1, 2]. This prediction has been astonishingly accurate for several decades, see Figure 1. One of the main drivers for this development was the miniaturization of transistors, which are the elementary building blocks of classical computers. The average size of state-of-the-art transistors decreased over several orders of magnitude during the last decades, thus enabling an ever larger number of transistors on the same chip size. This miniaturization was so successful that the gate size of transistors reached the nanometer scale during the 2000s [3].

As a consequence, the cross-section of modern transistors consists of just a few dozen atoms. This impressive success also indicates fundamental problems that are arising. For example, the statistical variance of doping as one channel only contains around five doping atoms in a

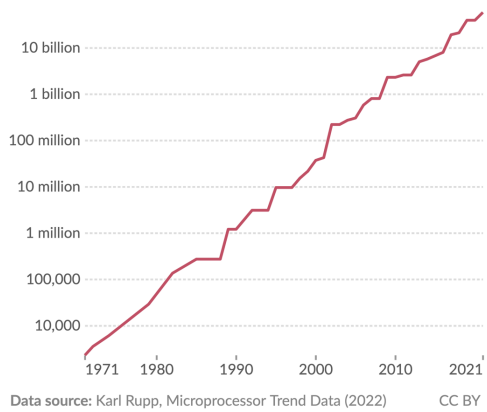

Figure 1: Historical development of the number of transistors per microprocessor. It shows a consistent, exponential growth of available computing power over 50 years. The figure was taken from [4].

10 nm transistor [3]. In terms of miniaturization, it appears that fabrication is approaching a fundamental limit, which will end Moore's law as we know it.

But is that even a problem? Modern computers are powerful and affordable machines that are widespread throughout society. Is it necessary to get more computing power, or is the available one already sufficient? The answer to this depends a lot on the problems one wants to solve. There is a vast class of computational tasks that are considered hard to solve [5]. In a simplified way, 'hard' means that the computational cost of the solution scales exponentially with the size of the problem.

Prime number factorization is one of the more famous examples [6]. Given some chosen integer number N, one would like to know whether N is a prime number. If it is not, the next step is to describe it as a product of prime numbers. For small numbers, this can be solved via brute-force calculation of division by smaller numbers. However, the possible combinations grow exponentially for large numbers N. The computational cost for the most efficient known algorithm, called GNFS, scales sub-exponentially like $O\left(\exp\left(\left(\frac{64}{9}\right)^{\frac{1}{3}}(\ln N)^{\frac{1}{3}}(\ln\ln N)^{\frac{2}{3}}\right)\right)$ for large numbers N [7]. Therefore, no matter how powerful a given classical computer is, there will always be numbers for which the prime number factorization takes more time than available. This is important because the security of the widely used RSA encryption [8] relies on the difficulty of prime number factorization.

Prime number factorization is an example where the difficulty of the computational task provides digital security and, therefore, is positive. However, there are many examples of hard computational problems where society would profit from effective solutions. A short, but not exhaustive, list includes the travelling salesman problem [5], protein folding [9], and energy storage systems [10]. The latter two are especially relevant for a thriving human society in the face of pandemics and the need for carbon-neutral energy production.

We conclude that there are problems from the real world demanding computational solutions, but we cannot hope for ever more powerful computers to eventually find solutions for all of them. What other options are imaginable?

2 Quantum computers: A new computation paradigm

One possible answer lies in the development of quantum computers [5, 11, 12]. Those are machines that do not encode information in classical bits (0 or 1) but in quantum bits (0, 1, and every possible superposition in between). A system comprising several qubits encodes information in a superposition state of all qubits and implements algorithms via gates performing operations on these states. A superposition state of N qubits can encode 2^N states simultaneously. Each state represents one number, thereby providing an exponential in-

Figure 2: One of the IBM quantum computers. Most of the machine is a cryostat, providing several layers of cooling. The actual chip containing the qubits is the black dot sitting at the bottom of the setup. The figure was taken from [13].

crease in computing power. The ability of quantum computers to implement circuits using this exponential increase to solve problems considered hard for classical computers is called quantum advantage.

We can sketch one possible way to achieve quantum advantage on a quantum computer as follows [5]. We consider a given computational task. We have a classical algorithm that takes the input x and calculates the output $f(x)$ called the oracle. This oracle $f(x)$ tells us whether x is a solution to the task or not. Our quantum computer consists of N qubits that we initialize in a superposition of many different inputs x. This input typically comprises all numbers $[0, 2^N]$. The advantage of a quantum computer lies in the fact that it performs the algorithm of the oracle on the superposition of all inputs x simultaneously, thereby calculating a superposition of all outputs $f(x)$ in one run. Unfortunately, quantum mechanics does not allow us to simply read out $f(x)$ for all x. This is fundamentally impossible. Instead, we need to find a second algorithm that takes advantage of the superposition and reduces the local inputs from all the points x to a global property of the function f. This can be read out in the end and corresponds to our final solution. Designing this second step is the challenging part of quantum algorithms, as the behavior of superpositions of quantum states doesn't follow classical intuition. The arguably most famous example of an algorithm achieving quantum supremacy is Shor's algorithm, which solves prime number factorization on a quantum computer in polynomial scaling $O(\log(N)^3)$, clearly outperforming the GNFS algorithm at large numbers.

In summary: Quantum computers don't calculate faster than classical computers, but algorithms solving certain, classically 'hard' computational problems are in another complexity class (scale more slowly) for quantum computers [5]. This is due to the possibility of probing the space of solutions more efficiently.

Due to the intriguing possibilities quantum computers offer, funding for their development has been increasing constantly. Regarding the sheer number of qubits, large technology

companies like Google and IBM are leading the field. For example, IBM started with the Falcon containing 27 qubits in 2019 and introduced a new, larger machine every year until the Condor in 2023, comprising 1,121 superconducting qubits [14]. See Figure 2 for an example of a quantum computer.

This progress is very impressive, and one could assume that these machines will soon be ready for the broad market. However, these platforms offer only a large number of physical qubits. Meaning every qubit has a certain stability and can perform all necessary gates. However, the operations are imperfect with error rates a lot larger than on modern classical computers. For example, the ibm_fez, which is a quantum computer of processor type Heron r2 available on the IBM Quantum Platform, has median gate errors $10^{-4} - 10^{-2}$, depending on the specific operation[1]. These errors render it impossible to perform long quantum algorithms [15].

Therefore, the next expected step is to apply error correction codes on these large systems [5]. The general idea of quantum error correction is to encode the information of one qubit redundantly in many qubits, monitor if they stay in the same state, and apply corrections if their states deviate. This approach reduces many physical qubits into a single logical qubit with fewer errors. There has been impressive progress in this direction with implementations of the surface code; see [16–20] for more details. However, still, if these large machines successfully implement a logical qubit via quantum error correction, we obtain systems offering a single qubit. To obtain a fully operational quantum computer, next, gates need to be successfully operated on these logical qubits and they need to be connected into larger networks. All of this will take continued research effort.

To decrease the necessary overhead of physical qubits in quantum error correction, it is vital to develop stable qubits and gates with as few errors as possible. This is the underlying motivation for qubit systems with protection against errors due to physical mechanisms, which finally bring us to the concept of topologically protected Majorana qubits. We provide a basic introduction to the concept of Majoranas in the next section.

3 What are Majoranas?

The concept of Majorana fermions comes from the field of particle physics. The idea goes back to the physicist Ettore Majorana and describes a particle that is its own anti-particle [21]. Within the field of condensed matter physics, the name was adapted to describe Majorana operators acting on electronic states inside an effectively one-dimensional superconducting nanowire [22, 23] depicted in Figure 3. This description already opens up several questions:

[1]Accessed on 19th of September 2025 via `https://quantum-computing.ibm.com/`

Figure 3: A topological superconductor hosting an isolated electronic state described by two spatially separated Majorana operators (orange crosses).

1. What is a superconductor? These are materials where electrons experience an attractive interaction that makes them group in pairs - so-called Cooper pairs [24]. These Cooper pairs create the fundamental background for Majorana operators, which behave like their own antiparticles [22]. Applying the Majorana operator once creates an electron. Applying the Majorana operator a second time combines that electron into a Cooper pair with another electron, seemingly destroying it again.

2. How can something be one-dimensional? Crucially, these systems are only 'effectively' one-dimensional. One fundamental difference between quantum physics and classical physics is the discretization of energies. Depending on the chosen basis, each system can be described by quantum states with well-defined, discrete energies. Assume we start with a three-dimensional system with x-, y-, and z-direction. If we strongly restrict the spatial extent L_x of a system in the x-direction, the associated energies split strongly due to the spatial restriction of the quantum mechanical wavefunction $\Delta E \propto \frac{1}{L_x^2}$ [25]. Next, we decrease the temperature of the system until the thermal energy is below the energy splitting $k_B T \ll \Delta E$. This way, the quantum particles are forced to be in a specific state, which prevents them from moving spatially. By doing so, we eliminated the x-direction and effectively created a lower-dimensional system. By repeating the same procedure in the y-direction, we arrive at an effectively one-dimensional system with only the z-direction left. This is the reason why many interesting examples of quantum physics in solid state materials are nicely observed by putting nanowires, where the wire circumference is only of the size of hundreds of nanometers (10^{-9} m), in ultra-cold fridges.

Importantly, not all one-dimensional superconducting nanowires hold Majoranas. The system needs to be a topological superconductor [23], which is a special class of superconductor, that we will explain in more detail in section 5. Inside a topological superconductor exists an energetically-isolated quantum mechanical state described by two Majorana operators. The topology forces the Majorana operators to localize at the boundaries between the topological and trivial phases. As the whole wire is in the topological phase, the boundaries are located at the physical ends of the wire, forcing the Majoranas to localize at these edges. This mechanism yields the topological protection. Small fluctuations in the parameters of the system cannot change the topological phase and therefore cannot move the Majoranas away from the wire ends.

Together, the finite length and the topology of the system guarantee the spatial separation. Accordingly, by connecting to just one end of the wire, we couple to just one of the Majoranas. Coupling to just 'half of an electron' behaves fundamentally differently from other

physical systems, where one always couples to a full electron.

In the following, we will provide a focused introduction to the vast research field of Majoranas. We will begin by discussing two different systems that are candidates for hosting spatially localized Majoranas. In particular, we will highlight the achievements and outstanding challenges of these experimental realizations. Afterwards, follows a discussion of the exotic physics of Majoranas, where we will introduce nonabelian braiding, designs for Majorana qubits, transport setups connecting to Majoranas, and the topological Kondo effect. We finish with a summary of the results of papers I-IV comprising this thesis. Here, the focus is on an intuitive picture to understand the suggested experiments, making the unique physics of Majoranas more accessible.

Where to find isolated MBSs

A wide range of theoretical models predict the existence of isolated Majorana bound states (MBSs). Prominent examples include ferromagnetic atomic chains on superconductors [26, 27], flux vortices in p-wave superconductors [28], the Kitaev chain [22], and the Rashba nanowire [29, 30]. In this chapter, we will focus on the latter two, as they are the models motivating the MBS system considered in papers I–IV. We begin with a brief introduction to superconductivity. Afterwards, we turn to the Kitaev chain and Rashba nanowire and outline the emergence of MBSs within them. We finish by discussing potential experimental realizations of both systems.

4 Quasiparticles in superconducting systems

As motivated in section 3 MBS operators can both create and annihilate fermionic occupations and are therefore combinations of fermionic creation and annihilation operators. Accordingly, we expect to find them in materials like superconductors, which carry particle-hole superpositions. Therefore, we will now prepare the ground for the later discussion on systems hosting MBSs with a basic introduction to superconductivity following [24].

Superconductors are materials in which electrons experience an attractive force between each other. As electrons are negatively charged and thus should repel one other, this attraction can't be due to a direct electromagnetic interaction between electrons. Instead, for low-temperature superconductors like Aluminium, it is an effective interaction that is mediated via the positively charged atomic lattice of the material within which the electron cloud moves. A given positive ion can attract two electrons that are spatially separated far enough not to repel each other. By choosing a description that removes this ion as a degree of freedom, we arrive at an effective picture in which two electrons experience a positive attraction between one other. This leads to the formation of a bosonic degree of freedom consisting of two correlated electrons, known as a Cooper pair. The zero resistivity of superconductors is due to these Cooper pairs. However, they also provide the background for the particle-hole superposition, motivated earlier, as the system allows for the coherent

creation and annihilation of a single Cooper pair in a sea of Cooper pairs.

The previous explanation is formalized by the BCS theory, which provides a microscopic derivation of superconductivity; for details on this, see [24, 31]. We begin with a general Hamiltonian describing electrons moving within a lattice of positive ions. In the first step, the many-body term of electron-ion interaction is transformed via a Schrieffer-Wolff transformation into an effective attractive interaction between electrons that is mediated by lattice phonons. Afterwards, applying a mean field approximation to the electron-electron correlations in the effective interaction yields the BCS Hamiltonian

$$H_{\mathrm{BCS}} = \sum_{k\sigma} (\varepsilon_k - \mu) c^\dagger_{k\sigma} c_{k\sigma} - \sum_k \Delta\, c^\dagger_{k\uparrow} c^\dagger_{-k\downarrow} + \Delta^* c_{-k\downarrow} c_{k\uparrow}. \tag{1}$$

The first term describes free electrons with kinetic energy ε_k at momentum k and spin σ in a chemical potential μ. The second term is the attractive interaction (global minus sign) between electrons. The attraction strength is determined by the superconducting interaction strength Δ. At first sight, this interaction seems unphysical, as it is described by a process that creates/destroys two electrons out of/into the vacuum. This is a result of the previously applied mean-field theory in which Δ was obtained as the expectation value of the correlations of creating/destroying two electrons. This approximation violates charge conservation but yields a good approximation to describe processes in superconductors.

Diagonalizing Eq. (1) via a Bogoliubov transformation yields the energy spectrum

$$E_k = \pm\sqrt{|\Delta|^2 + (\varepsilon_k - \mu)^2}, \tag{2}$$

and the ground state BCS wavefunction

$$|\psi\rangle_{\mathrm{BCS}} = C \prod_k (u^*_k + v^*_k\, c^\dagger_{k\uparrow} c^\dagger_{-k\downarrow})\, |0\rangle\,. \tag{3}$$

This ground state describes a superposition of any number of bosonic Cooper pairs combining into the macroscopic superconducting condensate. It lies at the chemical potential μ within an energy gap $\pm\Delta$ referred to as the superconducting gap. Charges in Cooper pairs inside this gap can move through the material while being protected from any scattering interaction that is smaller than the superconducting gap Δ, which results in the unique zero electrical resistance of these materials. Furthermore, the superconducting condensate provides an intuitive picture for the violation of charge conservation, as two existing charges can combine into a Cooper pair and, by that, vanish into the condensate. Outside of this gap lie the Bogoliubov quasiparticles created by the operator

$$b^\dagger_{k\uparrow} = v_k\, c_{-k\downarrow} + u_k\, c^\dagger_{k\uparrow}, \tag{4}$$

which creates a particle-hole superposition at energy E_k. The prefactors determining the particle (u_k) and hole (v_k) character are normalized, $|v_k|^2 + |u_k|^2 = 1$, and depend on the

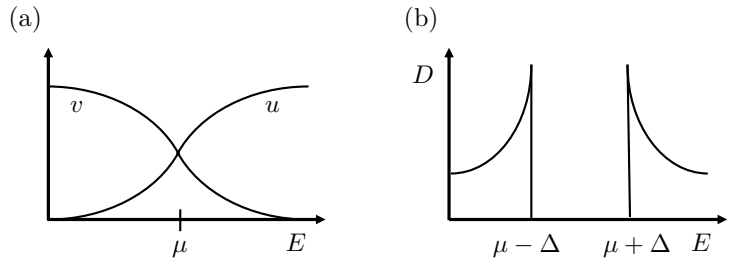

Figure 4: (a) Sketch of the particle (u) and hole (v) composition of Bogoliubov quasiparticles in a superconductor as a function of the energy E. Above (below) the chemical potential, the particle (hole) character dominates, with an equal superposition at $E = \mu$. (b) Sketch of the local density of states in a superconductor as a function of the energy E. There are no states inside of the superconducting gap ($|E - \mu| < \Delta$). At the gap boundaries ($E = \pm\Delta$), D diverges before falling off to the normal state value far away from μ.

energy E. See Figure 4 (a) for a qualitative representation of this dependence. The previous energy dependence of the state distribution is efficiently summarized in the density of states

$$D(E) = \frac{1}{2\pi} \int dk\, \delta(E - E_k), \tag{5}$$

which counts the number of states D in a infinitesimal interval between energies E and $E + dE$, see Figure 4 (b).

As explained before, the region inside the gap is empty for a BCS superconductor. In the following, we will introduce several models that also exhibit a superconducting gap but host a limited number of states inside the gap. For the remainder of this thesis, we will describe these systems via effective low-energy models, disregarding the states outside of the superconducting gap. This is possible if the considered interactions are smaller than Δ such that the energetic separation protects the considered states from unwanted interactions with quasiparticle states above or below the gap. BCS theory also predicts a competition between the superconducting pairing Δ that combines two electrons with opposite spin into a Cooper pair and the magnet fields B that introduce an energetic splitting between electrons of different spins. In general, applying magnetic fields reduces the superconducting gap Δ and closes it at a critical field strength. Throughout the manuscript, we will consider models containing both Δ and B but assume that the magnetic field B is sufficiently small to neglect this dependence.

5 Theoretical models predicting isolated MBSs

5.1 MBSs in the Kitaev chain

The Kitaev chain is one of the simplest models capturing the emergence of MBSs in a topological superconductor. It describes a one-dimensional array of N spinless fermionic

sites [22] with Hamiltonian

$$H_{\mathrm{KC}} = -\mu \sum_{k=1}^{N} n_k - \sum_{k=1}^{N-1} \left(t\, c_k^\dagger c_{k+1} + \Delta\, c_k^\dagger c_{k+1}^\dagger + \mathrm{h.c.} \right), \tag{6}$$

where μ is the on-site chemical potential, t the hopping amplitude, and Δ a superconducting potential. We choose $e = \hbar = k_B = 1$ throughout the remaining manuscript.

Crucially, Eq. (6) is a p-wave superconductor, where Cooper pairs have total spin ($L = 1$), formed by electrons of the same spin. This is a difference to the s-wave superconductors with ($L = 0$) considered during the discussion of BCS theory in section 4 [24]. This is necessary, as we assumed spinless fermionic sites where the wavefunction needs to be antisymmetric under the exchange of electrons in a Cooper pair. We will see in the later discussion about experimental realizations in section 6 how to artificially build p-wave superconductors that obtain their superconducting pairing from s-wave superconductors.

In the following, we consider the limit of long Kitaev chains ($N \gg 1$) with real-valued parameters t, Δ. For a more general treatment of finite-size effects, see [32], while extensions including phase gradients and next-nearest-neighbor hopping are found in [33, 34].

Diagonalizing the Kitaev chain

We start by rewriting the pair of creation and annihilation operators on each site into a pair of hermitian operators

$$\gamma_k = c_k^\dagger + c_k, \qquad \tilde{\gamma}_k = i(c_k^\dagger - c_k), \tag{7}$$

see Figure 5 (a). In general, this is just a choice of basis without any physical consequences. However, for one fine-tuned point in parameter space

$$\mu = 0, \qquad t = \Delta, \tag{8}$$

it can be shown [22, 23, 35], that the Kitaev Hamiltonian Eq. (6) transforms into

$$H_{\mathrm{KC}} = -it \sum_{k=1}^{N-1} \tilde{\gamma}_k \gamma_{k+1}, \tag{9}$$

where hybridizations are reduced to couplings of operators from neighboring sites to each other, see the black lines in Figure 5 (b). Interestingly, this coupling mechanism leaves two MBSs, $\gamma = \gamma_1$ (located on site 1) and $\tilde{\gamma} = \tilde{\gamma}_N$ (located on-site N), uncoupled. These MBSs describe a fermionic degree of freedom at zero energy, meaning that occupying it comes without any energy cost. Therefore, we obtain a doubly degenerate ground state inside the

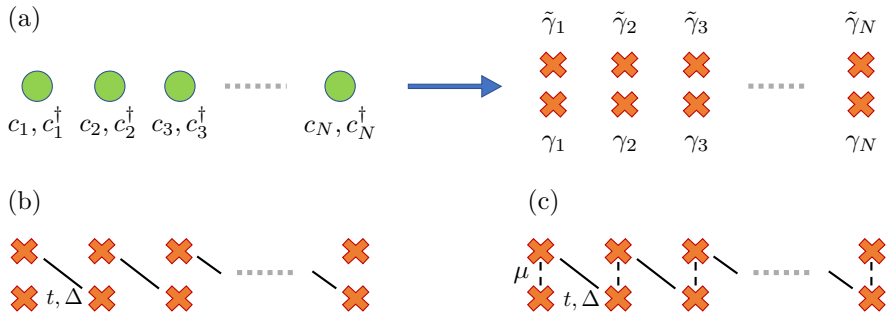

Figure 5: a) Basis transformation of the Kitaev chain from creation/annihilation operators (green circles, left) into MBS operators (orange crosses, right). (b) Kitaev chain with hybridizations $t = \Delta$ (black solid line) and $\mu = 0$. (c) Kitaev chain with hybridizations $t = \Delta$ (black solid line) and finite μ (black dashed line).

superconducting gap. The wave function of this state is described by one perfectly localized peak on either end of the wire.

Increasing μ couples the isolated MBSs γ_1 and $\tilde{\gamma}_N$ on the edges to the bulk chain, see Figure 5 (c). This has two effects: (i) It breaks the strict ground state degeneracy and (ii) $\gamma, \tilde{\gamma}$, describing the ground state, acquire tails exponentially decaying into the bulk. These two effects intertwine as the breaking of the ground state degeneracy is exponentially suppressed by the spatial separation. An approximate solution in the limit of long chains is possible [32]. However, we will restrict ourselves to a numerical investigation, by numerically diagonalizing the tight-binding Hamiltonian of Eq. (6)[2]. In the topological phase, the diagonalization will always yield two almost-degenerate zero-energy states that we combine to obtain the MBS wavefunctions, see Figure 6. To clearly visualize the spatial spread of the MBSs, we choose a short chain, $N = 40$, and a large chemical potential $\mu = \Delta = t = 1$. As we can see, the left (orange) and right (blue) MBSs are still the largest at their respective

[2]The implementation is available via [36] for reproducability.

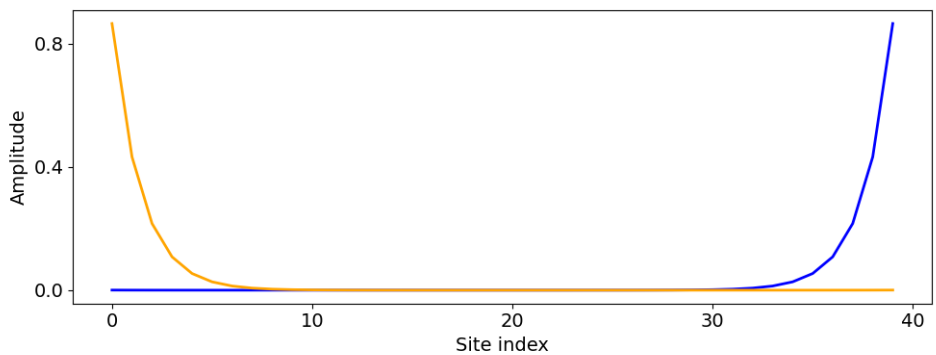

Figure 6: Numerical solution for the wavefunctions of MBSs in a Kitaev chain of length $N = 40$ at $\mu = \Delta = t = 1$.

ends of the wire while exponentially decaying into the inner part. This spread also leads to a hybridization between the MBSs that is exponentially suppressed for long wires. If we further increase μ, the spread will increase, eventually leading to a strong hybridization that lifts the fermionic state above the gap and transforms the system into a trivial superconductor. To calculate this transition point between the topological and trivial phases, we need to introduce the topological invariant characterizing the system.

Topological invariant of the Kitaev chain

A topological invariant is an integer that characterizes different topological phases of a system [37]. In particular, systems with the same integer are topologically equivalent and can be smoothly transformed into one another, i.e. without closing the bulk gap. On the other hand, transitions between different topological phases represented by different integers cannot happen due to small parameter fluctuations. For more details on the following explanations about the topological invariant of the Kitaev chain, see [38].

We start by translating the Kitaev chain Hamiltonian, Eq. (6), from the tight-binding representation to momentum space and express it in terms of Pauli matrices as

$$H_{\mathrm{KC}} = \frac{1}{2}\sum_{k\in BZ} C_k^\dagger \,\mathcal{H}\, C_k, \qquad\qquad \mathcal{H} = \varepsilon_k \sigma_z + \Delta_k \sigma_x = \vec{h}(k)\cdot\vec{\sigma}. \tag{10}$$

with $k \in [-\pi, \pi]$ varying inside the Brilloin zone (BZ). This representation allows us to map the Hamiltonian of the system onto a unit sphere

$$\hat{h}(k) = \vec{h}(k)/|\vec{h}(k)|. \tag{11}$$

It can be shown that this unit vector is aligned along the z-direction at the center and boundaries of the Brillouin zone

$$\hat{h}(0) = s_0\,\sigma_z, \qquad\qquad \hat{h}(\pi) = s_\pi\,\sigma_z, \tag{12}$$

where s_0 and s_π determine the direction of the alignment. The topological integer is given by multiplying these signs

$$\nu = s_0\, s_\pi = \pm 1. \tag{13}$$

If one follows the Hamiltonian of the system along the path from $k = 0$ to $k = \pi$ through the Brillouin zone, this path will either be a closed loop ($\nu = 1$, trivial phase) or connect the opposite poles of the sphere ($\nu = -1$, topological phase). Changing from one phase to the other requires $\hat{h}$ to be undefined along the path, which corresponds to closing the superconducting gap of the system. Therefore, the topological number is protected from parameter fluctuation smaller than the gap.

Explicit evaluation shows that the topological phase occurs when

$$2\,t > |\mu|, \qquad \Delta \neq 0. \tag{14}$$

In summary, the system needs a finite superconducting gap Δ to separate the different phases. The trivial phase occurs for a dominant on-site pairing μ and the topological phase for a dominant inter-site coupling t.

5.2 MBSs in the Rashba nanowire

Next, we will introduce the Rashba nanowire [29, 30]. The presented analysis will follow [39] closely. Like the Kitaev chain, the Rashba nanowire is an effectively one-dimensional model of a wire which contains momentum p, chemical potential μ, and superconducting pairing Δ. But additionally, it includes an effective mass m, spin degree of freedom $\vec{\sigma}$, spin-orbit coupling α, and a magnetic field B, making it a more realistic nanowire model. The following version of the Hamiltonian

$$H = \left(\frac{p^2}{2m} + V(x) - \mu - B\sigma_x + \alpha p \sigma_y \right) \tau_z + \Delta \sigma_y \tau_x, \tag{15}$$

is taken from [39] and includes a smooth potential $V(x)$ at one end of the nanowire. We will use $V(x)$ at a later point of the analysis to obtain trivial zero-energy fermions that are not topological MBSs. The superconducting pairing couples the spin to a particle-hole degree of freedom $\vec{\tau}$. The following results are based on a tight-binding representation of Eq. (15) [40], and solving the obtained Matrix via numerical diagonalization[3]. Motivated by [42] we choose the parameters to $\alpha = 50\,\text{meV nm}$, $\Delta = 0.5\,\text{meV}$, and $m = 0.015\,m_e$, where m_e is the mass of a free electron. Furthermore, we model the nanowire to be $2\,\mu$m long and discretize it on a grid with 500 grid points.

Isolated MBSs in the Rashba nanowire

We will start by setting the smooth potential to zero ($V = 0$). In this limit, [29, 30] show that the parameter space separates into two classes along the boundary

$$B^2 = \Delta^2 + \mu^2. \tag{16}$$

For sufficiently large magnetic field ($B^2 > \Delta^2 + \mu^2$), the nanowire is in the topological phase and hosts spatially isolated MBSs located at the ends of the wire. Otherwise, the system is in the trivial phase without any states inside the gap.

[3] The implementation is available via [41] for reproducibility.

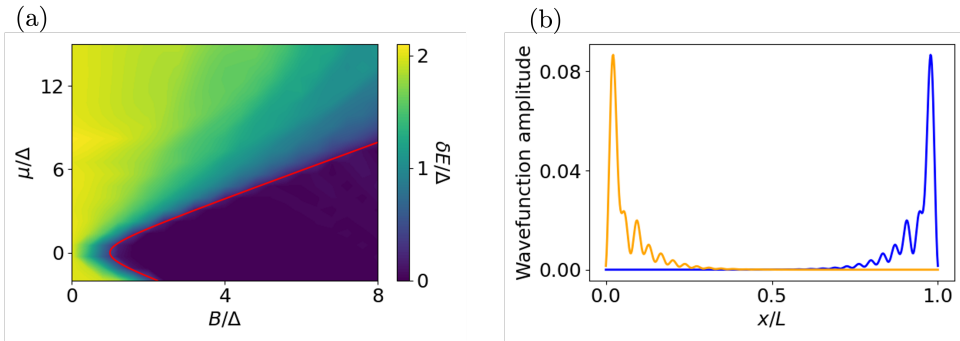

Figure 7: (a) Degeneracy splitting δE in the Rashba nanowire as a function of the magnetic field B and chemical potential μ showing the existence of zero-energy states in the dark blue region. The red line marks the analytical boundary between the topological and trivial phase. (b) MBS wavefunctions at $B = 2\,\Delta$ and $\mu = 0$.

Due to the particle-hole symmetry of Eq. (15) for each state at E, there exists another state at $-E$. Figure 7 (a) shows the energy splitting δE between the two states closest to $E = 0$ divided by the superconducting pairing Δ. We find qualitative agreement between the region predicted to host topological MBSs and the region hosting zero-energy states. In Figure 7 (b), we choose $B = 2\,\Delta$ and $\mu = 0$ inside the topological region and plot the resulting MBSs as already explained for the Kitaev chain. As predicted, they localize at the edges of the nanowire and decay exponentially ($\propto e^{-x/\xi}$), on a length scale ξ determined by the system parameters, from their respective edge towards the other side. On top of the exponential decay, we find an oscillation that was not present in the Kitaev chain, see Figure 6.

This qualitative agreement between the topological phase and the existence of zero-energy states in a Rashba nanowire suggests that it might be sufficient to analyse the spectrum to confirm the existence of topological MBSs inside the system. This is not the case, as we will see in the following.

Trivial zero-energy fermions in the Rashba nanowire

As done in [39], we now introduce the smooth potential

$$V(x) = a\, e^{-x^2/2\sigma^2} \tag{17}$$

with the parameters $a = 10\,\text{meV}$ and $\sigma = 200\,\text{nm}$. The remaining parameters of the nanowire are kept as before. We perform the same investigation of the energy splitting and the MBS wavefunctions inside the topological phase at $B = 2\,\Delta$, $\mu = 0$, see Figure 8.

There is no drastic change inside the topological parameter region. Figure 8 (a) shows that the system still hosts zero-energy states inside the topological region, and Figure 8 (b)

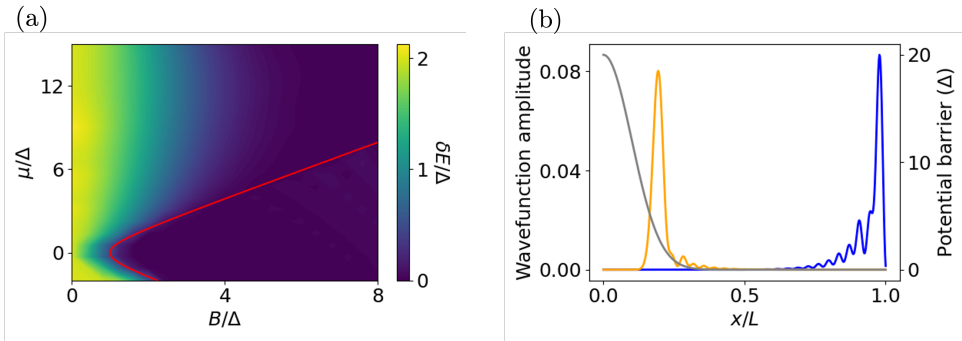

Figure 8: A recalculation of the data of Figure 7 including the effect of the smooth potential $V(x)$ defined in Eq. (17). (a) Degeneracy splitting δE in the Rashba nanowire as a function of the magnetic field B and chemical potential μ showing the existence of zero-energy states in the dark blue region. These zero-energy states occur now both in the topological and trivial parameter regime. The red line marks the analytical boundary between the topological and trivial phase. (b) MBS wave functions at $B = 2\,\Delta$ and $\mu = 0$. An additional (right) axis shows $V(x)$, Eq. (17) (gray line), which shifts the left MBS (orange) inside of the wire.

exemplifies that these states still resemble localized MBSs, where the left MBS (orange line) is shifted into the inner region. The reason for this is that $V(x)$ is a smooth modulation of the chemical potential

$$\mu_{\text{eff}}(x) = \mu - V(x). \tag{18}$$

This effective chemical potential pushes the nanowire into the trivial phase around the left edge ($0 < x \lesssim 2\,\sigma$) as predicted by Eq. (16). Inside the wire μ_{eff} falls off rapidly, defining a shifted boundary to the topological phase. The left MBS localizes at this shifted boundary. Figure 8 (b) includes a second axis showing $V(x)$ to visualize the effect.

However, the trivial parameter region changes significantly; it now hosts zero-energy states as well. Figure 9 shows one of those states at $B = 2\,\Delta, \mu = 3\,\Delta$ split into an MBSs basis. Without the topological protection, there is no mechanism forcing the MBSs to be spatially separated, like in Figure 8 (b). Instead, they localize in close vicinity to each other around the smooth potential barrier. Coupling to this state, also referred to as Andreev

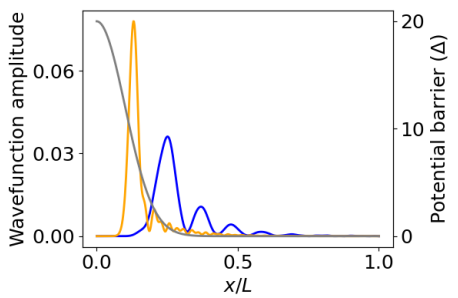

Figure 9: Trivial zero energy states appearing in the trivial phase at $B = 2\,\Delta, \mu = 3\,\Delta$ of a Rashba nanowire due to the introduction of a smooth potential barrier (gray line).

bound state (ABS), gives different behaviour depending on the spatial regions involved in the coupling. If a system only couples to the first MBS (orange peak), the state will behave like a topological MBS. If the coupling also includes the second MBS (blue), it will behave like a trivial fermionic state. We will discuss how to model this via tunnel couplings in more detail in section 10.

6 Experimental realizations of systems that potentially host isolated MBSs

In the following, we will discuss experimental systems aiming at realizing the previously introduced theoretical models. The challenge lies therein that p-wave superconductors are very rare in nature and candidates are exotic materials like Sr_2RuO_4 [43, 44] and UTe_2 [45]. Both presented approaches instead artificially create an effective p-wave pairing by combining s-wave superconductors with semiconductors exhibiting spin-orbit coupling. Together with the externally applied magnetic field B, this combines the three key ingredients that, according to [46], are necessary for p-wave superconductivity.

6.1 MBSs in superconductor-semiconductor hybrid structures

The idea behind superconductor-semiconductor hybrid structures is to combine properties like spin-orbit coupling α and long electron coherence length in semiconductors with superconductivity [47, 48]. By coating the semiconductor with a superconductor, the proximity effect will induce a superconducting gap Δ_{ind} in the semiconductor [49–52]. This is dependent on the transparency of the interface Γ and the superconducting gap Δ of the coating material. One intuitive picture is that the Cooper pairs living inside the superconductor can enter into the semiconductor, introducing superconducting coherences there. To obtain the necessary effectively one-dimensional systems the semiconductors are nanowires with a strict spatial restriction perpendicular to the wire orientation. These semiconducting nanowire is either epitaxially grown [53], see Figure 10 (a) and (b), or defined via an electrostatic gate applied to a two-dimensional electron gas [53]. Together with the external magnetic field B, these systems contain all parameters required by the Rashba nanowire and are thus candidates for the appearance of topological MBSs.

Although there are plenty of experimental results consistent with theoretical predictions [53, 55–61], the current results can not be considered to be sufficient proof of the existence of topological MBSs. These results consist mainly of zero-bias peaks obtained by electron spectroscopy, indicating the presence of zero-energy states, see Figure 10 (c). However, as we have seen in subsection 5.2, these could also be trivial zero-energy fermions/ABSs which provide an alternative explanation for these measurements [62–64]. Finding unambiguous

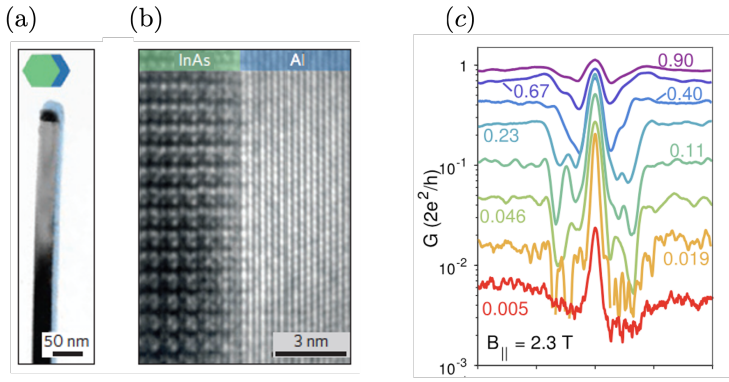

Figure 10: (a) A transmission electron microscopy (TEM) micrograph of an epitaxially grown superconductor-semiconductor hybrid nanowire. The 8 mm thick Al shell is colored in blue. On top, you see a cross-section of the wire geometry with green for the semiconductor (InAs) and blue for the superconductor (Al). (b) A high-resolution TEM picture of the semiconductor (InAs, left) -superconductor (Al, right) interface. (c) Tunneling conductance measurements as a function the applied bias voltage for several different values of the magnetic fields, showing zero-bias peaks consistent with MBSs in semiconductor-superconductor hybrid structures. The figures (a) and (b) were taken from [54] and (c) from [55].

proof of the topological nature of the devices is currently one of the big challenges of this research field. Therefore, in papers I and II, we checked the results of devices hosting topological MBSs, and then we modeled the same experiments for devices hosting trivial fermionic states.

6.2 MBSs in quantum dot-based Kitaev chains

We finalize this chapter by discussing quantum dot-based Kitaev chains. They are based on theoretical proposals in which the Kitaev chain is reduced to a minimum number of sites [65, 66]. The experimental realizations of these systems was one of the latest achievements in the search for isolated MBSs [67–74]. These chains consist of an array of spin-polarized single-level quantum dots (QDs). Figure 11 (a) shows the SEM picture of the experimental realization of a QD-based Kitaev chain consisting of two QDs. Each QD acts as a single site of the Kitaev chain with a gate-tunable on-site potential μ. In between the quantum dots are nanowires proximitized with superconductors hosting two ABSs each. The ABSs mediate two effective couplings between its connecting QDs: (i) the tunnel coupling t_{cot} via spin-conserving elastic co-tunneling and (ii) the effective p-wave pairing Δ_{CAR} via crossed-Andreev reflection, see Figure 11 (b).

Designing experimental setups with tunable $t_{\text{cot}}, \Delta_{\text{CAR}}$ coupling between the QDs was a major challenge for QD-based Kitaev chains. As the MBSs in short QD-based Kitaev chains are not topologically protected by a spatial separation [66], it is crucial to tune these systems to the sweet spot $t_{\text{cot}} = \Delta_{\text{CAR}}$ in which the Kitaev chain hosts perfectly localized MBSs. But there is an inherent competition between both processes as t_{cot} is spin-preserving

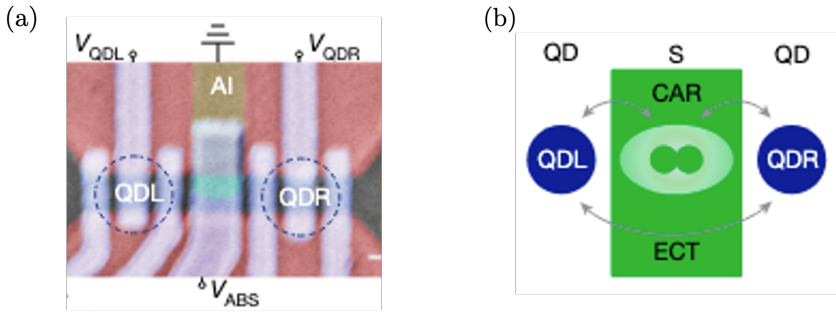

Figure 11: (a) Scanning electron microscopy image of an experimental realization of the QD-based Kitaev chain in a two-dimensional electron gas. (b) An effective representation of the minimal Kitaev chain with the left (QDL) and right (QDR) QDs coupled via elastic co-tunneling (ECT) and crossed Andreev reflection (CAR). The Figures were taken from [75].

but Δ_{CAR} relies on flipping the spin of one electron in the involved Cooper pair.

Early theoretical models suggested introducing a relative angle between the spins of neighboring QDs via, for example, micromagnets [66]. This would provide experimental control over a parameter varying between $t_{\mathrm{cot,\,max}}, \Delta_{\mathrm{CAR}} = 0$ for aligned spins and $t_{\mathrm{cot}} = 0, \Delta_{\mathrm{CAR,\,max}}$ for anti-aligned spins with a sweet-spot $t_{\mathrm{cot}} = \Delta_{\mathrm{CAR}}$ in between these extrema. But no experiments managed to realize this approach.

Setups as realized by [75] instead use aligned QD sites with couplings t_{cot} and Δ_{CAR} between the left and right QDs mediated by two ABSs inside a nanowire, as shown in Figure 11 (a). The necessary (partial) spin-flip is achieved by spin-orbit coupling inside the nanowires and the tunability between t_{cot} and Δ_{CAR} by gate tuning the particle-hole composition of the mediating ABSs. Next, we are going to discuss in detail how to understand this mechanism. We will begin by introducing a simple model for ABSs based on a QD proximitized by a superconductor, which shows the resulting gate-tunability of the ABS's particle-hole components. This directly translates into the gate-tunability of t_{cot} and Δ_{CAR} as we will see afterwards.

Gate controlling the particle hole composition of ABSs

The following short introduction into ABSs in proximitized QDs follows [76]. We begin by introducing the Hamiltonian for a single-level QD

$$H = \zeta\,(n_\uparrow + n_\downarrow) + U n_\uparrow n_\downarrow + \Delta\, d_\uparrow^\dagger d_\downarrow^\dagger + \Delta d_\downarrow d_\uparrow, \tag{19}$$

with spins $\sigma = \uparrow, \downarrow$, charging energy U, superconducting coupling $\Delta \in \mathbb{R}$ obtained via a proximitized superconductor and the single particle energies

$$\zeta = \varepsilon - \mu, \tag{20}$$

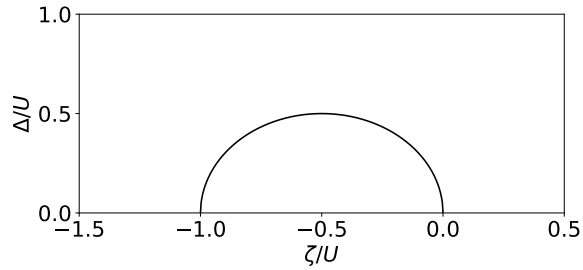

Figure 12: The dome around the center $\zeta/U = -\frac{1}{2}$, $\Delta/U = 0$ with radius $\frac{1}{2}$ as defined by the degeneracy condition in Eq. (23). Inside the dome, the ground state sector consists of the spin doublets $|\downarrow\rangle, |\uparrow\rangle$ and outside of it of the singlet $u|0\rangle - v|2\rangle$.

depending on the gate-controlled chemical potential μ. For a more detailed treatment including a magnetic field B and complex-valued Δ, see [76].

This four-dimensional system is directly solved by splitting it into even (e) and odd (o) total electron numbers and applying a Bogoliubov transformation to the even sector. This is in direct analogy to diagonalization of the BCS Hamiltonian as explained in section 4. We find the eigenenergies

$$E_{o,\sigma} = \zeta, \qquad E_{e,\pm} = \zeta + \frac{U}{2} \pm \sqrt{\left(\zeta + \frac{U}{2}\right)^2 + \Delta^2}, \tag{21}$$

with the eigenstates

$$|o,\pm\rangle = |\sigma\rangle, \qquad |e,\pm\rangle = u|0\rangle \pm v|2\rangle. \tag{22}$$

The ground state sector is determined by the degeneracy condition

$$E_{o,\sigma} \stackrel{!}{=} E_{e,-} \qquad \Rightarrow \qquad \frac{U}{2} = \sqrt{\left(\zeta + \frac{U}{2}\right)^2 + \Delta^2}, \tag{23}$$

defining a dome around $\zeta/U = -\frac{1}{2}$, $\Delta/U = 0$ with radius $\frac{1}{2}$, see Figure 12. Inside the dome, the ground sector consists of the spin doubles $|\downarrow\rangle, |\uparrow\rangle$ and outside of it of the singlet $u|0\rangle - v|2\rangle$. To simplify the discussion, we choose to place the system outside of the dome, continuing with the ground state

$$|GS\rangle = u|0\rangle - v|2\rangle, \tag{24}$$

with excitations to the singlet states

$$|EX\rangle = |\downarrow\rangle, |\uparrow\rangle, \tag{25}$$

split off by the energy difference

$$E = E_{o,\sigma} - E_{e,-} = -B - \frac{U}{2} + \sqrt{\left(\zeta + \frac{U}{2}\right)^2 + \Delta^2}. \tag{26}$$

These excitations describe ABSs with energy E created by

$$|EX\rangle \langle GS| = u^* |\sigma\rangle \langle 0| - v^* |\sigma\rangle \langle 2|, \tag{27}$$

with the particle (u) and hole (v) character

$$u^2 = \frac{1}{2}\left(1 + \frac{E + U/2}{\sqrt{\left(E + \frac{U}{2}\right)^2 + \Delta^2}}\right), \quad v^2 = \frac{1}{2}\left(1 - \frac{E + U/2}{\sqrt{\left(E + \frac{U}{2}\right)^2 + \Delta^2}}\right), \tag{28}$$

directly determined by the single particle energies ζ. The single particle energy ζ in turn contains the chemical potential μ, which is determined by a gate voltage V_g applied to the QD. This makes the electron hole composition of the quasiparticle experimentally controllable via an electric gate.

Gate controlling the couplings $t_{\mathrm{cot}}, \Delta_{\mathrm{CAR}}$ in the QD-based Kitaev chain

The following analysis follows [77]. A minimal QD-based Kitaev chain, as shown in Figure 11 (a), is described by the Hamiltonian

$$H_{\mathrm{mKC}} = H_{\mathrm{QDs}} + H_{\mathrm{ABSs}} + H_{\mathrm{coup}}, \tag{29}$$

consisting of a left (l) and right (r) QD, two ABSs ($m = 1, 2$) in the central nanowire, and the tunnel coupling between these systems. The approach, as developed by [77], is to assume both the QD occupations and ABS to be in their ground states. In the next step, the effective coupling between the QDs mediated by the ABSs is obtained by a second-order process, virtually occupying the ABSs. For this approach to be valid, it is essential that the couplings t_l, t_r are small compared to the ABS energies E_m. Formally, these effective couplings are calculated via a Schrieffer-Wolff transformation and read

$$\begin{aligned} t_{\mathrm{cot}} &= \frac{t_l t_r}{\Delta} \sum_{m=1,2} \frac{u_m(x_l) u_m^*(x_r) - v_m(x_r) v_m^*(x_l)}{E_m/\Delta}, \\ \Delta_{\mathrm{CAR}} &= \frac{t_l t_r}{\Delta} \sum_{m=1,2} \frac{u_m(x_l) v_m^*(x_r) - u_m(x_r) v_m^*(x_l)}{E_m/\Delta}. \end{aligned} \tag{30}$$

The spatial dependencies x_l, x_r are due to the spatial extent of the ABSs over the length of the nanowire. These spatial dependences encode the spin precession while an electron

travels through the nanowire. The wire length L and spin-orbit wave vector k_{so} should result in a misaligned spin rotation compared to the QD spin polarization, $k_{so} L \neq 0, \pi$.

Furthermore, as can be seen from Eq. (30), both couplings consist of two different paths of virtual processes. For example, we consider a charge tunneling from the right to the left QD via t_{cot}. The charge can either first tunnel from the right dot into an ABS ($u_m^*(x_r)$) and then out of the ABS into the left dot ($u_m(x_l)$). Alternatively, the tunnelling process first splits a Cooper pair by tunnelling one charge into the left QD and the other occupies the ABS ($v_m^*(x_l)$), after which the charge from the right QD recombines with the ABS occupation to reform the Cooper pair ($v_m(x_r)$). As both processes happen coherently, the final result is a superposition of them. Importantly, these two paths interfere destructively, while the two paths for Δ_{CAR} interfere constructively at $\zeta = 0$ [77]. This different interference behaviour, together with the different scaling of t_{cot} and Δ_{CAR} with ζ/Δ, guarantees the occurrence of a sweet spot at which $t_{cot} = \Delta_{CAR}$ [77].

How to work with MBSs

In the following chapter, we will develop the necessary tools to model MBS systems and discuss their most fundamental physical properties. This groundwork also sets the stage for the discussion of the papers I-IV. We begin by introducing an effective picture in which MBSs are treated as fully localized operators. Subsequently, we discuss the nonabelian (non-commutative) exchange statistics of MBS, the construction of qubits based on MBSs, transport through MBS systems in the tunneling regime, and finally, the topological Kondo effect.

7 The effective picture to describe MBSs

The following effective picture translates the exponentially localized MBS wavefunction introduced in the previous section 5 into a simpler description of localized operators with exponentially suppressed hybridizations, see Figure 13. Importantly, this effective picture needs to be introduced for long one-dimensional nanowires like the Rashba nanowire of section 5 but naturally already exists for minimal QD-based Kitaev chains.

As explained in section 5, MBSs emerge from an (almost-)zero-energy state inside the superconducting gap Δ of a topological superconductor. From the creation/annihilation operators $c^\dagger, c$ of this state, we obtain the MBS operators

$$\gamma = c^\dagger + c, \qquad \tilde{\gamma} = i(c^\dagger - c), \tag{31}$$

which are exponentially localized ($\propto e^{-\zeta/L}$) at different spatial boundaries of the system.

Figure 13: Effective representation of a topological subgap state (gray line, left) via two zero-dimensional MBS operators (orange crosses, right).

These operators are hermitian

$$\gamma^\dagger = \gamma, \qquad \tilde{\gamma}^\dagger = \tilde{\gamma}, \tag{32}$$

anticommute

$$\{\gamma, \tilde{\gamma}\} = 0, \tag{33}$$

and square to identity

$$\gamma^2 = \tilde{\gamma}^2 = 1. \tag{34}$$

The MBS operators can be combined to define a non-local fermionic parity operator

$$i\gamma\tilde{\gamma} = 1 - 2c^\dagger c = \pm 1, \tag{35}$$

whose eigenvalues ± 1 are the quantum numbers of the associated fermionic mode. Equivalently, one can describe the fermionic mode via an occupation operator

$$n = \frac{1}{2}\left(1 + i\gamma\tilde{\gamma}\right) \in \{0, 1\}. \tag{36}$$

As there exists a direct mapping between parities and occupations, we will occasionally switch between descriptions. The effective Hamiltonian of this two-level system reads

$$H = \varepsilon\, i\gamma\tilde{\gamma}, \tag{37}$$

with eigenenergies $\pm\varepsilon$. The energy splitting $\Delta E = 2\,\varepsilon$ is due to the residual hybridization $\varepsilon \propto e^{-\zeta/L}$ between the MBSs that is exponentially suppressed for long wires. For the remaining manuscript, we will assume that this splitting is smaller than the superconducting gap ($\varepsilon \ll \Delta$) to justify the effective single particle description in which we neglect interactions with states above the gap. Also, we will assume that the localization length ζ is a lot smaller than the system length L, which allows viewing the MBSs as localized objects, see Figure 13.

This effective low-energy picture with localized MBS forms the foundation for the following discussion on their non-Abelian exchange statistics.

8 Nonabelian properties of MBSs

To motivate why the exchange statistics of MBS are special, we take a step back and consider the wavefunction $|\psi\rangle$ of a three-dimensional quantum system consisting of two indistinguishable quantum particles. Exchanging the position of these particles results in a trivial modification of the wavefunction by a global sign $|\psi\rangle \to \pm\,|\psi\rangle$. This ensures that during a double exchange, leading each particle back to its original position, the wavefunction is not

changed at all $|\psi\rangle \rightarrow (\pm)^2 |\psi\rangle = |\psi\rangle$. Each sign of the exchange statistics is connected to one fundamental particle class: Bosons $(+)$ and Fermions $(-)$. However, crucially, this logic holds only in three dimensions. A double exchange is equivalent to a closed loop of one particle around the other. In three dimensions the path of this loop can always be contracted into a single parameter point, thereby making it trivial.

This contraction is in general not possible in a two-dimensional system, where the contracted path would need to cross the encircled particle [78–80]. As a consequence, the exchange statistics of quantum particles in two dimensions is described by a unitary transformation not equal to the trivial $\pm$-sign of three-dimensional particles. Particles like the MBSs with a non-trivial exchange phase are called anyons [80–82]. Exchanging two MBSs is called a braid, a term motivated by the often used representation via world-lines in (2+1) dimensions, see [80, 82]. Consecutive braids, in general, don't commute, making them nonabelian. In the following, we will introduce braiding in more detail, investigate implementations that don't require spatial exchange and control over the position of MBSs, and discuss the connection between braiding and fusion rules. Fusion rules are a fundamental property of nonabelian anyons based on consecutive measurements of different parity bases, referred to as fusion channels [83].

8.1 Braiding

We will now provide a short introduction to braiding. For additional information, see [23, 35]. We start by considering a system hosting four MBSs $\tilde{\gamma}_L, \gamma_L, \tilde{\gamma}_R, \gamma_R$. We assume perfect degeneracy, meaning that hybridizations ε between the MBSs are so small that they are negligible. A natural choice of basis for the four-dimensional Hilbert space is obtained by grouping the left and right pairs of MBSs into parities $i\gamma_L\tilde{\gamma}_L$ and $i\gamma_R\tilde{\gamma}_R$, see Figure 14. To make the connection to fusion in the following subsection 8.2 and paper II more explicitly, we express the basis via occupation operators as defined in Eq. (36). This yields the four Fock states

$$|n_L, n_R\rangle \in \{|00\rangle, |01\rangle, |10\rangle, |11\rangle\}. \tag{38}$$

Braiding operations conserve the total parity of the system

$$\sigma = i^2 \gamma_L \tilde{\gamma}_L \gamma_R \tilde{\gamma}_R = \pm 1, \tag{39}$$

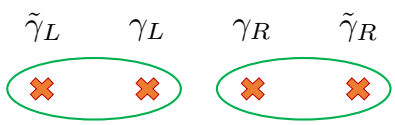

Figure 14: Four MBSs (orange crosses) are the necessary minimum for non-trivial braiding. The chosen basis representation is indicated by green circles around the combined MBSs.

which serves as a good quantum number and splits the states into two groups

$$\sigma = 1: \quad \{|00\rangle, |11\rangle\}, \qquad \sigma = -1: \quad \{|01\rangle, |10\rangle\}. \tag{40}$$

Braiding acts within each subspace, inducing rotations between its states. For simplicity we start by choosing $\sigma = 1$ and the initial state $|\psi_0\rangle = |00\rangle$. We will first examine how a single and double braid acts on the chosen initial state, then generalize the behaviour to arbitrary initial states via a calculation of the Berry phase U. The Berry phase is an operator representing the ground state transformation implemented by a closed parameter-loop in a time-dependent Hamiltonian $H(t)$ with adiabatically slow changes [84–86]. Initially, we assume full control over the spatial positions of the MBSs. Later, we comment on how to implement these exchanges by tuning parameters in the time-dependent Hamiltonian $H(t)$ and alternative braiding implementations that don't require spatial exchanges of MBSs.

Single braid

A single braid corresponds to exchanging two MBSs, here chosen as γ_L, γ_R [23], see Figure 15. We choose γ_L, γ_R as they are from different occupations of the basis, see Figure 14, which ensures a nontrivial rotation of the ground state. The chosen parametrization of the exchange doesn't influence the outcome, which is known as the path independence of the braiding operation. If we regroup the MBSs into pairs according to their new spatial configuration, namely $\tilde{\gamma}_L, \gamma_R$ for n'_L and $\gamma_L, \tilde{\gamma}_R$ for n'_R, the occupation states $|n'_L, n'_R\rangle$ relate to the original $|n_L, n_R\rangle$ basis via

$$|n_L, n_R\rangle = |00\rangle \qquad \rightarrow \qquad |n'_L, n'_R\rangle = \frac{|00\rangle + |11\rangle}{\sqrt{2}}. \tag{41}$$

This σ_x basis rotation may appear trivial because, mathematically, it is equivalent to a simple basis redefinition, which we could also have performed without the single braid. The key difference is that the chosen basis is motivated by the spatial locations of the MBSs. Still, the reason for this apparent triviality is that a single braid is not a closed loop in parameter space. Therefore, its Berry connection can be transformed backwards into a single parameter point, which reduces it to a trivial identity $U = 1$. The effect of the spatial MBS exchange is revealed only when we fix the basis according to the spatial configuration, as done above. Specifically choosing the basis like this is not necessary for the double braid, as we will see in the following.

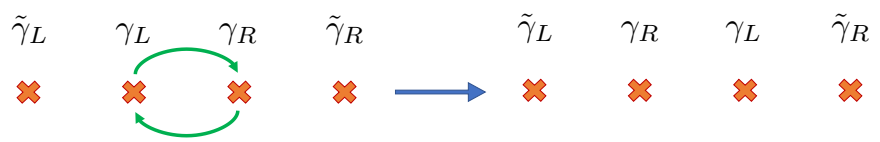

Figure 15: Implementation of a single braid via spatial exchange of the MBSs γ_L, γ_R.

Double braid

As indicated by the name, a double braid is implemented by two single braids. Meaning we perform the first braid as already shown in Figure 15 and afterwards perform the same exchange one more time. This is equivalent to moving γ_L one time around γ_R and back to its original position, see Figure 16. Therefore, a double braid leaves the spatial order of MBSs $\tilde{\gamma}_L, \gamma_L, \gamma_R, \tilde{\gamma}_R$ unchanged, and we describe the system with the same basis $|n_L, n_R\rangle$ before and after the operation. It can be shown that the initial state is transformed as [23, 35]

$$|\psi_0\rangle = |00\rangle \qquad \rightarrow \qquad |\psi'\rangle = |11\rangle\,. \tag{42}$$

Both occupations get flipped by the transformation. $|\psi(t)\rangle$ represents the instantaneous eigenstates of the time-dependent Hamiltonian $H(t)$ implementing the loop. One can show that the Berry phase for the described double braid is [23, 35]

$$\begin{aligned} U &= e^{\frac{\pi}{2}\gamma_R\gamma_L}, \\ &= \gamma_R\gamma_L, \end{aligned} \tag{43}$$

where the second line is obtained via writing the exponential into a sum and using $\gamma_{L/R}^2 = 1$. By directly acting on the different operators characterizing the system, we can summarize the effect of braiding. It switches the signs of the MBSs involved in the braid

$$U\gamma_L\,U^\dagger = -\gamma_L, \qquad\qquad U\gamma_R\,U^\dagger = -\gamma_R, \tag{44}$$

but leaves the uninvolved MBS operators unchanged

$$U\tilde{\gamma}_L\,U^\dagger = \tilde{\gamma}_L, \qquad\qquad U\tilde{\gamma}_R\,U^\dagger = \tilde{\gamma}_R. \tag{45}$$

Therefore, it flips the initialized parities

$$Ui\gamma_L\tilde{\gamma}_L\,U^\dagger = -i\gamma_L\tilde{\gamma}_L, \qquad\qquad Ui\gamma_R\tilde{\gamma}_R\,U^\dagger = -i\gamma_R\tilde{\gamma}_R \tag{46}$$

and its respective occupations

$$Un_L\,U^\dagger = \bar{n}_L, \qquad\qquad Un_R\,U^\dagger = \bar{n}_R \tag{47}$$

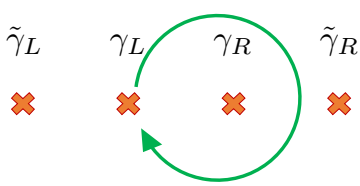

Figure 16: A double braid is implemented via two single braids as shown in Figure 15. This is equivalent to moving γ_L one time around γ_R.

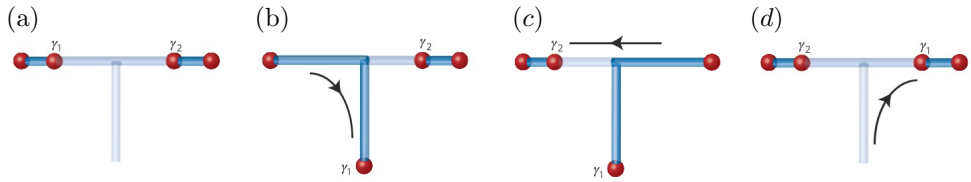

Figure 17: (a) - (d) Theoretical proposal for implementing a single braid in a trijunction. The blue colors mark the parts of the nanowire that are in the topological regime, thereby controlling the MBS positions. The figure was taken from [87].

with the convention $\bar{0} = 1$ and $\bar{1} = 0$.

In contrast to the single braid, the double braid is obtained by a closed loop in parameter space. Importantly, the path of γ_L can not be contracted into a single point without crossing γ_R, which would violate the spatial separation and hybridize the MBSs into a trivial Fermion. Compared to the single braid, which had a contractable path, this leads to a Berry phase acting nontrivially on the system.

Realizing braiding by spatially moving MBSs

A number of proposals suggest implementing MBS exchange in various platforms by physically moving their locations [28, 87]. The underlying idea is to shift the boundary between the trivial and topological phases of the superconductor by tuning the parameters of the time-dependent Hamiltonian $H(t)$. Since MBSs are localized at this boundary, such tuning enables direct control over their positions.

One of the most well-known theoretical proposals for braiding in superconductor–semiconductor hybrid structures is based on the trijunction geometry [87], see Figure 17. It allows direct control over the MBS position via gates controlling the chemical potential of the different segments. For a more detailed explanation on this, see [87].

Despite its conceptual simplicity, this approach was never experimentally realized. As an alternative, one can perform hybridization-based braiding, which achieves the same non-abelian exchange without requiring direct spatial control over MBSs.

Hybridization-based braiding

There exist numerous suggestions on how to perform braiding via hybridizations of MBSs [83, 88–93]. As summarized by [94] the required MBS hybridizations can be obtained via direct wavefunction overlap [92, 95] or control over the Coulomb interactions [88, 90, 91].

Hybridization-based braiding relies on a setup including six MBSs $\gamma_1, \tilde{\gamma}_1, \gamma_2, \tilde{\gamma}_2, \gamma_3, \tilde{\gamma}_3$, see

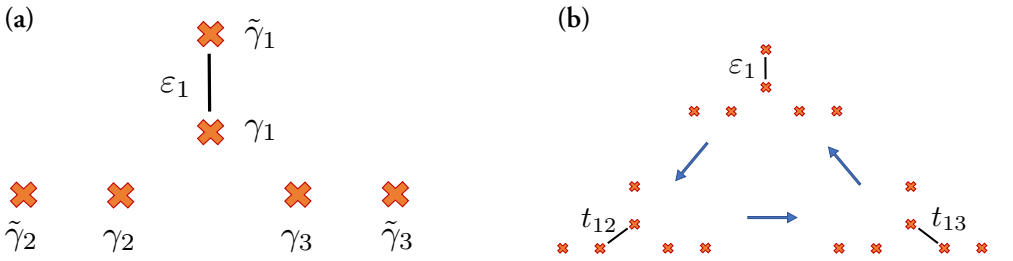

Figure 18: (a) The initial and final configuration for hybridization-based braiding. (b) The protocol for hybridization-based braiding of γ_2 and γ_3.

Figure 18 (a). Compared to Figures 14 - 16, the numbering of MBSs is shifted via $L \to 2$ and $R \to 3$ to match the labeling in paper IV. Now the goal is to braid MBSs γ_2 and γ_3. Before introducing the full protocol we first discuss MBSs γ_1 and $\tilde{\gamma}_1$

In the initial ($\tau = 0$) and final ($\tau = T$) configuration of the protocol γ_1 and $\tilde{\gamma}_1$ are strongly hybridized

$$H(\tau = 0, T) = \varepsilon_1 \, i\gamma_1\tilde{\gamma}_1. \tag{48}$$

This hybridization defines the ground state sector at energy $-\varepsilon_1$ by setting the parity

$$i\gamma_1\tilde{\gamma}_1 = -1. \tag{49}$$

As before, the four uncoupled MBSs $\gamma_2, \tilde{\gamma}_2, \gamma_3, \tilde{\gamma}_3$ build a fourfold degenerate ground-state sector divided into two subspaces by the conserved total parity

$$\sigma = i^3\gamma_1\tilde{\gamma}_1\gamma_2\tilde{\gamma}_2\gamma_3\tilde{\gamma}_3. \tag{50}$$

The braiding protocol induces rotations within these subspaces. In this sense, the additional fermionic degree of freedom $i\gamma_1\tilde{\gamma}_1$ is introduced only to be immediately gapped out. Its role is to provide a spatially separated location to temporarily store one of the braided MBSs during the protocol. This is in direct analogy to the trijunction, Figure 17, where the vertical wire serves as a temporary storage location of one MBS. Instead of moving the boundary between the topological and trivial regimes, the exchange is realized via the time-dependent Hamiltonian

$$H(\tau) = \varepsilon(\tau)\, i\gamma_1\tilde{\gamma}_1 + t_{12}(\tau)\, i\gamma_1\gamma_2 + t_{13}(\tau)\, i\gamma_1\gamma_3. \tag{51}$$

During the protocol the hybridization is slowly transferred from $i\gamma_1\tilde{\gamma}_1$ to $i\gamma_1\gamma_2$, then to $i\gamma_1\gamma_3$ and finally back to $i\gamma_1\tilde{\gamma}_1$, see Figure 18 (b). The exact parametrization of the hybridizations is not important, which reflects the path-independence of MBS braiding. The only two rules are: 1. the hybridization gap

$$\Delta_{\text{hyb}} = \sqrt{\varepsilon(\tau)^2 + t_{12}(\tau)^2 + t_{13}(\tau)^2}, \tag{52}$$

must stay finite throughout the protocol, and 2. the changes of the Hamiltonian have to be adiabatic with respect to this gap

$$|\partial_\tau \frac{H(\tau)}{\Delta_{\text{hyb}}}| \ll \Delta_{\text{hyb}}, \tag{53}$$

to avoid excitations above the gap. If these restrictions are met, a single run of the protocol implements the transformation

$$U_{\text{SB}} = e^{\frac{\pi}{4}\gamma_3\gamma_2}, \tag{54}$$

corresponding to a single braid of MBS γ_3 and γ_2. The double braid follows by performing the same protocol a second time. We discuss both an intuitive and analytical explanation of why this protocol implements a single braid in the discussion of the results of paper IV. We now conclude the discussion of nonabelian properties by turning to fusion rules.

8.2 Fusion rules

Fusion is another fundamental property of anyons closely related to braiding [80, 87, 90, 91, 93]. Compared to braiding, fusion rules offer a conceptually simpler route to demonstrating nonabelian statistics. Braiding requires two key capabilities: (i) the ability to initialize and measure MBS parities in well-defined pairs (e.g. $i\gamma_L\tilde{\gamma}_L$ in Figure 14), and (ii) control over the MBS positions via a time-dependent Hamiltonian. Fusion rules remove the second requirement, but instead demand initialization and read-out in at least two different parity bases. However, Fusion rules are considered less reliable than double braids in distinguishing topological and trivial phases [93].

We start with the minimal setup of four MBSs encoding two fermionic degrees of freedom, initialized in the left and right parities, see Figure 19 (a). We assume the system is prepared in the state $|n_L, n_R\rangle = |00\rangle$. Next, we measure in a rotated parity basis $|n, \tilde{n}\rangle_{\text{rot}}$, defined by the joint parities $i\gamma_L\gamma_R$ and $i\tilde{\gamma}_L\tilde{\gamma}_R$. Expressing the initial state in this basis gives

$$|00\rangle = \frac{|00\rangle_{\text{rot}} + e^{i\theta}\,|11\rangle_{\text{rot}}}{\sqrt{2}}, \tag{55}$$

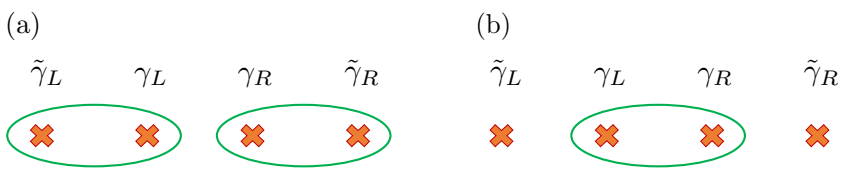

Figure 19: Initialization (a) and read-out (b) scheme for a fusion rule protocol.

where $e^{i\theta}$ is a relative phase determined by the basis choice. The measurement projects the system into the mixed state

$$\rho = \frac{1}{2}\left(|00\rangle\langle 00|_{\text{rot}} + |11\rangle\langle 11|_{\text{rot}}\right), \tag{56}$$

with each outcome $|00\rangle_{\text{rot}}$ and $|11\rangle_{\text{rot}}$ occurring with equal probability. Verifying this 50/50 distribution requires repeating the protocol multiple times. In practice, measuring only one of the two joint parities is sufficient, as the other follows from total-parity conservation, see Figure 19 (b).

9 Constructing an MBS qubit

The idea of topological quantum computing is to encode quantum information in topologically protected states [16, 80, 96, 97]. The topological protection together with protected quantum operation holds the promise of long qubit life-times and high gate fidelities [16, 80, 98]. Early proposals focused on fractional quantum hall states, which are anyons found as surface states in topological insulators [80, 96, 99]. Advances in the fabrication of superconductor-semiconductor hybrid structures have brought MBS-based platforms into the focus of attention [87, 91, 100, 101]. There are several suggestions of different setups realizing qubits via MBSs, which differ in the number of MBSs and the employed geometry [97, 100, 102]. Of particular interest has been the two-sided MBS tetron, from here on referred to as MBS tetron, containing the minimal number of four MBSs [97, 103].

In the following, we will introduce the MBS tetron in detail. Outlining its computational states, error sources, and potential experimental implementations. We will finish the section with a discussion of the disordered MBS tetron containing additional MBS or unprotected trivial states.

9.1 The MBS tetron

To obtain the MBS tetron, we need four MBSs, which span a four-dimensional Hilbert space. Total parity conservation splits the Hilbert space into two two-dimensional subspaces. Each subspace contains two degenerate states acting as computational states.

We construct the MBS tetron by connecting two topological superconductors via a trivial superconductor, see Figure 20. The whole system (topological and trivial superconductors) is floating and has a charging energy associated with the total number of electrons. The contained MBSs γ_{rm} are labeled by their nanowire ($m = u, d$) and respective side on which they localize ($r = L, R$). The low-energy Hamiltonian of this system reads [98]

$$H_{\text{sys}} = \sum_{m=u,d} \frac{i}{2} \varepsilon_m \gamma_{Lm} \gamma_{Rm} + E_C (N - n_g)^2, \tag{57}$$

where ε_m are hybridizations between MBSs within the upper and lower topological superconductors. E_C is the charging energy, N is the number of electrons on the island, including those forming Cooper pairs, and n_g is the excess charge on the island in the ground state. We assume E_C and the superconducting gap Δ are both much larger than the overlaps between the MBSs ($E_C, \Delta \gg \varepsilon_m$).

We obtain a Fock basis of our system by combining MBSs into fermionic states. Motivated by the discussion of paper I we combine γ_{Lu} with γ_{Ld} and γ_{Ru} with γ_{Rd} into

$$c_L = \frac{1}{2}(\gamma_{Lu} + i\gamma_{Ld}), \qquad c_R = \frac{1}{2}(\gamma_{Ru} + i\gamma_{Rd}), \tag{58}$$

to obtain the occupations n_L and n_R. From this choice, we obtain the Fock states of the MBS tetron as

$$|\psi\rangle = |n_L n_R, N\rangle \,. \tag{59}$$

Due to the large charging energy parity, each occupation n_r is connected to a specific charge. Therefore, we have N, which is the sum of the charges contained in Cooper pairs and in the MBS occupations.

The excess charge is tuned via an electrostatic potential as

$$n_g = \alpha_g \, V_g \tag{60}$$

with the lever arm α_g. It sets the numbers of charges N and $N+1$ on the island in the low-energy spectrum of H_{sys}, which consists of the four states

$$|00, N\rangle \,, \qquad |11, N\rangle \,, \qquad |10, N+1\rangle \,, \qquad |01, N+1\rangle \,. \tag{61}$$

N and $N+1$ are uniquely determined by the excess charge via

$$N \leq n_g \leq N+1. \tag{62}$$

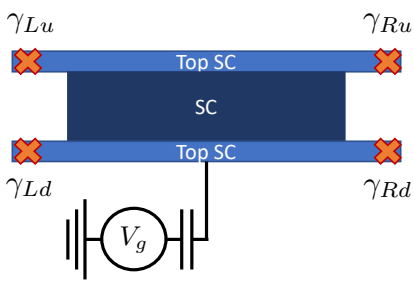

Figure 20: The MBS tetron - two topological superconductors (light blue), each hosting one MBS at each end (orange crosses). They are connected via a trivial superconductor (dark blue) into a floating island. A gate voltage V_g is applied to tune the excess charge $n_g \propto V_g$ of the ground state.

In papers I and II, we will choose n_g such that N is an even number. The large charging energy allows us to drop the total charge N from the notation and only discuss the occupations of the MBS degrees of freedom

$$|n_L n_R, N\rangle \rightarrow |n_L n_R\rangle \,. \tag{63}$$

The thus obtained computational states are protected by several mechanisms [97, 98]. Errors from finite MBS hybridizations are exponentially suppressed in the length of the wire, $\varepsilon \propto e^{-L/\zeta}$, see section 5. Thermal excitations of quasiparticles outside the superconducting gap are suppressed by low temperatures $\propto e^{-\Delta/T}$. Furthermore, tuning the excess charge n_g in a charge valley suppresses poisoning by charges from outside the system.

Building an MBS tetron

Before continuing with the disordered MBS tetron, we will shortly discuss experimental implementations of the MBS tetron. There has been recent experimental progress in the development of MBS tetrons as Microsoft announced the fabrication of the so-called Majorana I, a system containing a grounded version of the Majorana tetron [104], see Figure 21. Whether the system holds topological MBS is not yet fully clear.

The current state of the experimental characterization of this system is based on single-shot parity readout [105–108]. For this readout, external quantum dots k, l can be connected to selected wire ends k, l. If assuming topological MBS in the system, this connection enables measuring the parity $i\gamma_k\gamma_l$. The presented results of readout of different MBS basis combinations show short life-times of parities connecting MBSs from different wires as compared to parities of MBSs in the same wires [104]. This difference in the error of different bases hints at MBS hybridizations inside the wires as the main source of error [104].

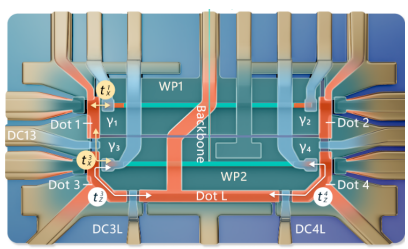

Figure 21: The MBS tetron of the Majorana I - a grounded version of the MBS tetron announced by Microsoft in [104]. It consists of two nanowires (light green), potentially holding MBS $\gamma_{1,2,3,4}$ connected via a grounded superconductor marked as backbone. Five quantum dots labelled 1, 2, 3, 4, L, tunnel coupled to the system, enable single-shot parity readout of the system in different basis combinations. The figure was taken from [104].

9.2 The disordered MBS tetron

As explained in section 5, we want to compare the results of the MBS tetron to the case of an imperfect system that either hosts additional MBSs or trivial fermions. As a minimal model for this situation, we consider the disordered MBS tetron, shown in Figure 22. The unwanted fermionic degrees of freedom are indicated by MBSs $\tilde{\gamma}_{rm}$. We describe the system with the Hamiltonian

$$H_{\text{sys}} = \sum_{\substack{m=u,d \\ r=L,R}} \frac{i}{2} \varepsilon_{rm} \gamma_{rm} \tilde{\gamma}_{rm} + \sum_{m=u,d} \frac{i}{2} \Omega_m \tilde{\gamma}_{Lm} \tilde{\gamma}_{Rm} + E_C (N - n_g)^2, \tag{64}$$

where $\varepsilon_{rm}, \Omega_m \ll \Delta, E_C$ describe hybridizations between the respective outer and inner MBSs.

We obtain a Fock basis of the system by combining MBSs γ_{rm} and $\tilde{\gamma}_{rm}$ at each corner of the box into occupations n_{rm}

$$|\psi\rangle = |n_{Lu}, n_{Ld}, n_{Ru}, n_{Rd}\rangle \,, \tag{65}$$

which yields a total ground state manifold of 16 states. Total parity conservation splits it into two subgroups of eight states each. The total parity of each group is equivalent to one total charge (N or $N+1$). As before, for simplicity, we drop the number of charges from the notation.

This model captures two qualitatively similar cases. First, the additional MBSs can be localized inside the topological nanowires at a transition from the topological to the trivial regime due to disorder inside the wire. Second, the model can describe trivial fermions where γ_{rm} and $\tilde{\gamma}_{rm}$ are a basis representation for the trivial state. In this case, the two MBSs would be spatially overlapping. The difference between these cases lies in the parametrization of the tunnel couplings $t_{rm}, \tilde{t}_{rm}$ as we will see in section 10 and will discuss further in papers I and II.

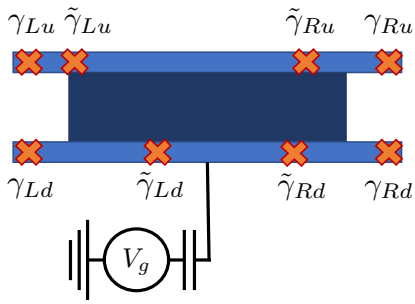

Figure 22: A disordered MBS tetron - two topological superconductors (light blue), each hosting two MBSs, one at each end (orange crosses). Due to disorder, the box contains four additional MBSs inside the wire. They are connected via a trivial superconductor (dark blue) into a floating island.

10 Transport through MBS system

In the following, we will develop a model describing transport through MBS systems in leading order of the tunnel coupling. We start by establishing the Hamiltonian describing tunnel coupling from fermions to MBSs. Afterwards, we discuss the formalism of quantum master equations (QMEs), which is commonly used to solve transport setups involving weak tunnel coupling and large interactions [109].

10.1 Tunnel coupling to MBSs

The derivation of the tunnel Hamiltonian presented in the following is based on work by [110]. We consider a single fermionic mode $d, d^\dagger$ tunnel coupling (t_c) to the left side of an otherwise isolated, interacting quantum system H_{sys}, see Figure 23. Within the interacting system exists one spatially extended fermionic mode inside a superconducting gap Δ described by two MBSs

$$\gamma = \sum_{k=0}^{N} e^{-i\phi/2}\xi_k\, c_k^\dagger + e^{i\phi/2}\xi_k^*\, c_k, \qquad \tilde{\gamma} = \sum_{k=0}^{N} e^{-i\phi/2}\tilde{\xi}_k\, c_k^\dagger + e^{i\phi/2}\tilde{\xi}_k^*\, c_k. \tag{66}$$

ϕ is the superconducting phase of the system and $\xi_k, \tilde{\xi}_k$ describe the wavefunction solutions for $\gamma, \tilde{\gamma}$ obtained via the diagonalization of the system Hamiltonian H_{sys} discretized on a lattice labelled by $k \in [0, N]$. See, for example, the solutions of $\xi, \tilde{\xi}$ obtained from numerical diagonalizations of the Kitaev chain and Rashba nanowire in section 5.

We describe the tunnel Hamiltonian by coupling the fermionic mode to the first site of the nanowire in a tight-binding representation

$$H_{\text{coupling}} = t_c\, d^\dagger\, c_0 + h.c.\,. \tag{67}$$

To obtain an expression in terms of $\gamma, \tilde{\gamma}$ we invert Eq. (66)

$$c_0 = e^{-i\phi/2}(\xi_0\,\gamma + \tilde{\xi}_0\,\tilde{\gamma}) + \sum_{l=1}^{N}(c_{l,0}\,\gamma_l + \tilde{c}_{l,0}\,\tilde{\gamma}_l), \tag{68}$$

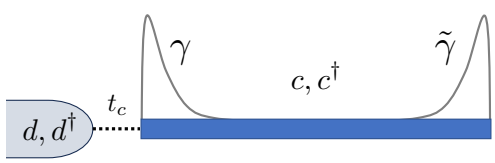

Figure 23: Fermionic mode $d, d^\dagger$ tunnel coupling to a spatially extended fermionic mode $c, c^\dagger$, inside an interacting quantum system, split into two spatially localized MBS $\gamma, \tilde{\gamma}$ inside a nanowire.

where $\gamma_l, \tilde{\gamma}_l$ are hermitian operators describing states above the superconducting gap Δ. We assume that the fermionic mode is energetically close to the almost-degenerate ground states of $\gamma, \tilde{\gamma}$ and that the weak coupling, $t \ll \Delta$, means that we can neglect states above the gap. In this limit, we can rewrite Eq. (67) as

$$H_{\text{coupling}} = t_c \, d^\dagger \, e^{-i\phi/2}(\xi_0 \, \gamma + \tilde{\xi}_0 \, \tilde{\gamma}) + h.c. \,. \tag{69}$$

As the final step, we redefine the tunnel coupling by absorbing the wavefunction amplitudes

$$t = t_c \, \xi_0, \qquad\qquad \tilde{t} = t_c \, \tilde{\xi}_0, \tag{70}$$

yielding

$$H_{\text{coupling}} = d^\dagger \, e^{-i\phi/2}(t\gamma + \tilde{t}\tilde{\gamma}) + h.c. \,. \tag{71}$$

For topological MBSs, we assume that $\tilde{\gamma}$ localizes on the right-hand side of the system and that the wavefunction amplitude on the left side is exponentially suppressed by the spatial separation, $\tilde{\xi}_0 \approx 0$, resulting in $\tilde{t} = 0$. The fermionic limit, on the other hand, is described by full spatial overlap of the MBS wavefunctions, $|\xi| = |\tilde{\xi}|$, leading to $t = i\tilde{t}$. We will come back to this in the discussion of papers I and II.

10.2 External fermionic mode inside an electric lead

Next, we consider the system hosting the external fermionic mode $d, d^\dagger$. The mode is hosted by a macroscopic electric lead hosting many non-interacting electrons in a Fermi gas described by the Hamiltonian

$$H_{\text{FG}} = \sum_{k\sigma} \xi_k f^\dagger_{k\sigma} f_{k\sigma}, \tag{72}$$

where $f^\dagger_k$ creates an electron with spin σ, wavenumber k and energy $E = \xi_k$. The occupation probability of a state at energy E in the Fermi gas is determined by the Fermi distribution

$$f(E) = \frac{1}{1 + e^{(E-\mu)/T}}, \tag{73}$$

which is characterized by the temperature T and the chemical potential μ. For the considered transport setups, we assume that the temperature T is smaller than the charging energy and the superconducting gap, $E_C, \Delta \gg T$, of the interacting system. By expressing this lead in a tight-binding representation we find $d, d^\dagger$, which destroy/create a fermionic occupation of the last site connecting to the interacting quantum system. Analogously to subsection 10.1, we invert the tight-binging representation and describe the $d, d^\dagger$ by the modes $f_{k\sigma}, f^\dagger_{k\sigma}$.

10.3 Master equation description of transport through quantum systems

After establishing how to model the leads and their connections to MBS systems, next, we introduce quantum master equations (QMEs) to solve these transport systems in the weak coupling limit. See [109] for more details on the derivation of QMEs and [111] for numerical implementations and solutions of QMEs.

Derivation of the QME

Putting all elements together, the full system Hamiltonian reads

$$H_{\text{tot}} = H_{\text{sys}} + H_{\text{lead}} + H_{\text{coupling}}, \tag{74}$$

where H_{sys} is given by the small interacting quantum system, H_{lead} represents the leads, and H_{coupling} describes the tunnel coupling between the leads and the small interacting system. The principal solution of the time evolution of the density matrix ρ_{tot} for the whole system is given by the Liouville-von Neumann equation

$$\partial_t \rho_{\text{tot}} = -i[H_{\text{tot}}, \rho_{\text{tot}}]. \tag{75}$$

The difficulty with an exact solution lies in the combination of a large number of degrees of freedom of the electric lead and the strong interactions of the small interacting system. We start by splitting the full system into degrees of freedom for the small interacting system and the leads

$$\rho_{\text{tot}} = \rho \otimes \rho_{\text{lead}}, \tag{76}$$

which is an approximation in leading order of the tunneling, as we neglect quantum-mechanical correlations between the system and the leads [109]. In the next step, we trace out ρ_{lead} from Eq. (75). During this step, we view the leads in the stationary limit, which is valid due to the considered limit of small tunnelling rates $\Gamma = 2\pi\nu t^2 \ll T$, where ν represents the density of states of the leads. We assume ν to be energy-independent and the same for all leads. For more details on this procedure, see [109]. We obtain the time evolution of the reduced density matrix as

$$\partial_t \rho = -i\left[\tilde{H}_{\text{sys}},\, \rho\right] + \mathcal{D}\,\rho, \tag{77}$$

which is split into two parts. First, the unitary time evolution is introduced by a version of the system Hamiltonian $\tilde{H}_{\text{sys}}$, which is potentially modified by including the Lamb shift [109]. The Lamb shift is a non-uniform shift of the energy levels in the small system due to the tunnel coupling to the leads. Second, a non-hermitian contribution $\mathcal{D}$ which describes the dissipative dynamics induced by the leads. The exact form of the dissipative term $\mathcal{D}$ depends on the chosen formulation, like the Redfield, first-order von Neumann, or Lindblad QME [111].

Solution for a general QME

To solve Eq. (77), we first rewrite it in superoperator notation [111], where the density matrix is represented by a vector $|\rho)$ and the time evolution is collected into a Liouvillian $\hat{\mathcal{L}}$ in the form of a matrix. We rewrite Eq. (77) as

$$\partial_t|\rho) = \hat{\mathcal{L}}\,|\rho). \tag{78}$$

Solving this is done via diagonalization of the Liouvillian. As the Liouvillian is in general non-hermitian, the eigenvalues χ_h are complex-valued. Furthermore, the left and right eigenvectors, $|l_h)$ and $|r_h)$, are not necessarily the same for a given eigenvalue. After acquiring the eigenvalues and eigenvectors, we can write the finite-time solution as

$$|\rho)(t) = |\rho)_{\text{ss}} + \sum_{h>0} e^{\chi_h t} c_h |r_h), \tag{79}$$

where c_h is obtained from the initial state $|\rho_0)$ as

$$c_h = (l_h|\rho_0). \tag{80}$$

The solution is split into two parts, the stationary state solution $|\rho)_{\text{ss}}$ and the finite time contribution. This is motivated by a general property that needs to be checked to have a well-defined solution. First, there should be exactly one zero eigenvalue, $\chi_0 = 0$, which defines a unique stationary state solution. If there exist several zero eigenvalues, that's a sign of symmetries in the system. Second, the real part of the remaining eigenvalues should be smaller than zero ($\text{Re}(\chi_h) < 0;\ \forall h > 0$). This leads to a strict exponential decay of all finite-time contributions. A violation of this condition leads to the unphysical case of an exponential increase of the respective contribution at large times.

11 The Kondo effect

One effect that is unique about the MBS tetron is the emergence of the topological Kondo effect [112]. We will first shortly discuss the standard Kondo effect [113] emergent in the Anderson impurity model [114], and afterwards we will explain the topological Kondo effect.

11.1 The Anderson impurity model

The Kondo effect explained the experimental observation that magnetic impurities in conductors lead to an increase in the resistance below a certain temperature called the Kondo

temperature T_K [113]. Kondo showed that this is explained by an anti-ferromagnetic interaction between the magnetic impurities and the conductance electrons, leading to an effective screening of magnetic impurity below T_K, which in turn yields an increase in resistivity as $\rho \propto \log(T)$. Schrieffer and Wolff showed in [115] that this anti-ferromagnetic interaction emerges as a strong coupling below a critical temperature in the Anderson impurity model

$$H = H_{\text{sys}} + H_{\text{lead}} + H_{\text{coupling}}, \tag{81}$$

tunnel coupling a single-level impurity

$$H_{\text{sys}} = \varepsilon_\sigma n_\sigma + E_C n_\uparrow n_\downarrow, \tag{82}$$

with spin σ and charging energy E_C to an electric lead. Since these early days, the Anderson impurity model has been extensively investigated, with many numerical routines applying different approximations to resolve the behaviour of the model below the Kondo temperature T_K [116–119].

11.2 The topological Kondo effect

The minimum setup to investigate the topological Kondo effect is one topological MBS tetron coupled to three electric leads via

$$H_{\text{coupling}} = \sum_{l=2,3,4} t_l d_l^\dagger \gamma_l + h.c., \tag{83}$$

as introduced by [112], see Figure 24. The electric leads are operated in the zero-bias, $\mu_1 = \mu_2 = \mu_3 \approx 0$, and zero temperature, $T_2 = T_3 = T_4 \approx 0$, limit. All tunnel couplings have to be finite $t_2, t_3, t_4 > 0$, but don't need to be fine-tuned to a specific parameter point. The excess charge n_g is tuned to establish a well-defined ground state charge

$$n_g = N, \tag{84}$$

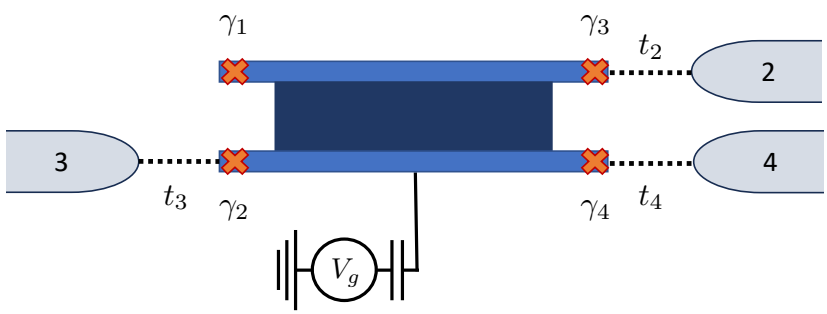

Figure 24: The minimal setup exhibiting the topological Kondo effect. Three leads couple to MBS $\gamma_2, \gamma_3, \gamma_4$ in the zero bias and low temperature limit.

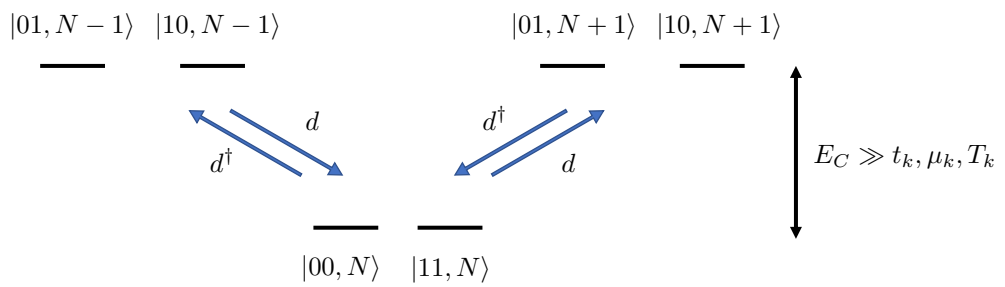

Figure 25: Tunnel transitions of the Kondo setup. The qubit can virtually occupy excited states at energy E_C by adding/subtracting a charge from the lead and reversing that process again. The degenerate ground state manifold resembles a spin-$\frac{1}{2}$ that can get flipped by a virtual transition.

which we choose to be an even number. This defines a two-dimensional ground state manifold

$$|\psi\rangle_{\text{gs}} = |00, N\rangle\,, |11, N\rangle\,, \tag{85}$$

and four excited states

$$|\psi\rangle_{\text{exc}} = |01, N \pm 1\rangle\,, |10, N \pm 1\rangle\,, \tag{86}$$

at energy E_C. We identify the ground state manifold with a spin-$\frac{1}{2}$ degree of freedom by defining the following Pauli matrices

$$\sigma_x = i\gamma_1\gamma_2, \qquad \sigma_y = i\gamma_1\gamma_3, \qquad \sigma_z = i\gamma_1\gamma_4. \tag{87}$$

In leading order of the tunnel coupling, the tuning of n_g suppresses transport through the tetron as the only available charge states are split by a large energy E_C. In second order, co-tunnelling processes can virtually occupy the excited states before returning to the ground state [112, 115, 117], as shown in Figure 25. Importantly, this virtual process can flip the effective spin of the system. This is formally solved by a Schrieffer-Wolff transformation, yielding the effective Hamiltonian

$$H_{\text{eff}} = \frac{1}{2}\sum_\alpha \lambda_\alpha\, \sigma_\alpha J_\alpha, \tag{88}$$

where the energies $\lambda_\alpha = \sum_{ij} |\epsilon_{\alpha ij}| \frac{t_i t_j}{2E_c}$ describe the second-order coupling and $J_\alpha = i\sum_{ij}\epsilon_{\alpha ij}\, d_i^\dagger d_j$ is a spin-1 degree of freedom distributed over the three leads [112]. This system can be solved via a renormalization group analysis in the limit $\mu_l, T_l \to 0$ and below the Kondo temperature T_K, it exhibits exotic non-Fermi liquid behaviour, associated with the nonlocal conductance

$$G_{kl}(T) = \frac{dI_k}{d\mu_l} = \frac{2}{3} + c_{kl} T^{\frac{2}{3}}, \tag{89}$$

quantifying the response of current through lead k as a reaction to a change of the chemical potential of lead l, with nonuniversal coefficient c_{kl} [112].

Results

12 Summary and discussion for papers I and II

The overall goal addressed in papers I and II is to perform elementary qubit operations on MBS tetrons via experiments based on slow DC current measurements. The proposals aim at extracting information about crucial properties like the coherence time and to distinguish topological systems from tetrons hosting trivial states, introduced in section 9. In each paper, we introduce one transport setup weakly coupling (disordered) MBS tetrons to electric leads, described via QMEs as introduced in section 10. In paper I, we focus on tetron initialization and characterization, while paper II introduces a transport-based fusion protocol. All proposed experiments employ parity blockade, which was first established for parity read-out of MBS tetrons. We will begin by discussing the nature of parity blockade in detail. To this end, we will also introduce charge cycles, which are an intuitive way to investigate the behaviour of MBS-based transport setups. Afterwards, we will discuss the content of papers I and II. In comparison to papers I and II, the focus will be on understanding the main results of each publication in terms of charge cycles. They are useful for a qualitative explanation of the dynamics, thereby providing intuition. However, the quantitative results were obtained by full analytical and numerical solutions of the respective QMEs and can be found in papers I and II.

12.1 Understanding parity blockade via charge cycles

It has proven useful for papers I and II to describe the transport dynamics and parity blockade in terms of charge cycles. We will exemplify charge cycles on the transport setup of paper I and learn how to intuitively think about parity blockade in that setup. Afterwards, we generalize the procedure to arbitrary amounts of MBSs and declare general conditions for implementing a charge cycle description and parity blockade.

Transport setup for the MBS tetron

We start by considering the transport setup, shown in Figure 26. Tunneling amplitudes t_{ls} connect the leads $l = L, R$ to the upper ($s = u$) and lower ($s = d$) MBSs on the respective ends of the MBS tetron via

$$H_T = \sum_{ls} t_{ls}\, d_l\, \gamma_{ls} + h.c.\,. \tag{90}$$

We tune $n_g \propto V_g$ such that there exist only two charge states, N and $N+1$, in the low-energy sector, and the higher energy states are split off by $E_C \gg t_{ls}$. As the phase term $e^{\pm i\phi/2}$ appearing in Eq. (69) is responsible for tracking the number of electrons inside the system, which is trivial in our case, we absorb it into the tunnel coupling t_{ls}. For simplicity, we start by assuming that all tunnel amplitudes are of the same absolute value $|t_{ls}| = t$. We will investigate the effect of relaxing this condition in the later discussion of paper I. This choice defines the tunneling rate $\Gamma = 2\pi\nu t^2$, as introduced in subsection 10.3. We decided that the tunneling rate is smaller than the temperature, $T \gg \Gamma$, but larger than the overlaps of MBSs inside the tetron, $\Gamma \gg \varepsilon$. We tune the chemical potentials of the leads to achieve a symmetric bias voltage $V_b = \frac{\mu_L}{2} = -\frac{\mu_R}{2}$ defining the left (right) lead as the source (drain) for $V_b > 0$.

If a charge tunnels from the left lead into the tetron, there are two possible paths available - either via γ_{Lu} or γ_{Ld}. The interference between these paths is set by the tunneling amplitudes t_{Lu} and t_{Ld}. We use the gauge degree of freedom to choose $t_{Ld} = t$ and $t_{Lu} = t\, e^{i\phi_L}$. The relative phase ϕ_L is tuned via the magnetic flux Φ_L threaded between the two paths. With the same argument we also choose $t_{Rd} = t$ and $t_{Ru} = t\, e^{i\phi_R}$ tuned via Φ_R.

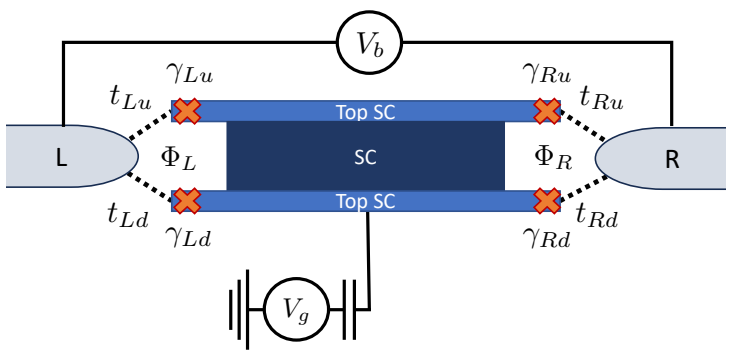

Figure 26: Transport setup for the MBS tetron. The MBS γ_{lu}, γ_{ld} on each side of the tetron connect to one lead $l = L, R$. The connections form a left and right loop, which are threaded with magnetic fields Φ_L, Φ_R. The chemical potentials μ_l of the leads are adjusted to establish a symmetric voltage bias V_b. A gate voltage V_g is applied to adjust the number of electrons in the ground state sector.

Coulomb diamonds in transport through MBS tetrons

At first, we need to ensure a tuning of the gate (V_g) and bias voltage (V_b) that enables transport through the system. The conductance-dependence we find by tuning these gates is known as Coulomb diamonds, see Figure 27. It is a typical transport signature of systems with large charging energies, like, for example, QDs [120, 121]. The voltage axes are scaled by the lead temperature T. The current I is shown in units of the tunneling rate Γ. We can distinguish between two regimes. The conducting regime in the bright yellow and dark blue regions. The sign of the current is directly given by the sign of the bias voltage. The second regime is the Coulomb-blocked regime with a suppressed current (green region). In this regime the energy splitting between the states with N electrons ($|00\rangle$, $|11\rangle$) and $N+1$ electrons ($|10\rangle$, $|01\rangle$), set by the gate voltage V_g, is too large to overcome for electrons from the chemical potential μ_l of the leads. In this regime, the system gets stuck in either the $N+1$ charge states (positive V_g) or the N charge states (negative V_g). In both papers, we tune the systems into the conducting regime with $V_b = 100\ T$, $V_g = 0$. By this choice, we define the left lead as the source and the right lead as the drain. Tunneling events in the opposite direction are exponentially suppressed in the limit $V_b \gg T$.
2cm

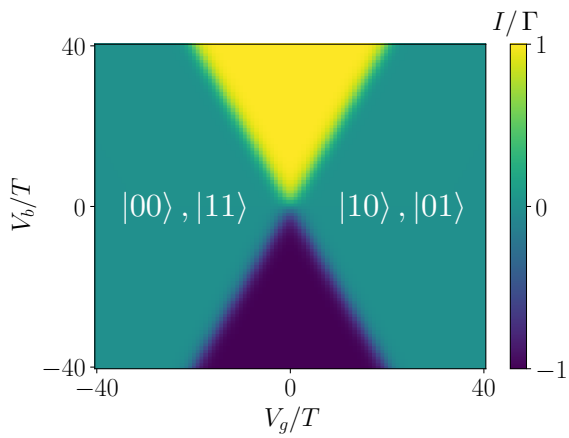

Figure 27: Current I through the MBS tetron with respect to gate (V_g) and bias voltage (V_b). We find conducting regions (yellow, blue) and regions where transport is suppressed (green). The green areas are marked with the stationary state Fock states in the established Coulomb valleys.

Description of transport through the MBS tetron via charge cycles

As described in subsection 9.1, we choose the basis of combining the left and right MBS pairs and obtain the four basis states as

$$|\psi\rangle = |n_L n_R\rangle \,. \tag{91}$$

The charge cycle works according to the following principle. For each state of the system, there is only one possible process for a charge to either tunnel from the source into the system or from the system into the drain. This simple dynamics only holds in the limit of large charging energy, as this allows only for putting either a charge into the system or taking one out. Furthermore, the large bias voltage compared to the temperature allows electrons to tunnel in only one direction.

Assume that we start with the system in the initial state $|00\rangle$. The only possible process at this point is to add a charge to the system via the source. This changes the state to $|10\rangle$. Next, a charge has to tunnel out of the system into the drain, changing the state to $|11\rangle$. This anomalous event of tunneling a charge out, while occupying the state, $n_R = 0 \to 1$, can be understood as the splitting of a Cooper pair. Next, a charge from the source tunnels into the system, changing its state to $|01\rangle$. The cycle is finished by a charge tunneling out to the drain, leading back to the initial state $|00\rangle$. We summarize the dynamics in the following charge cycle:

$$|00\rangle \to |10\rangle \to |11\rangle \to |01\rangle \to |00\rangle \to \dots \tag{92}$$

Each arrow in a charge cycle corresponds to a process associated with a rate. In this cycle, all rates are given by Γ. For each full cycle, two electrons are transferred through the system.

Parity blockade in the MBS tetron described via charge cycles

The tunnel rate for each process in Eq. (92) is directly proportional to the square of the tunnel amplitude of the respective tunnel coupling, see Eq. (90). For example the transitions $|11\rangle \to |01\rangle$, $|00\rangle \to |10\rangle$ are due to the coupling

$$t\, d_L(\gamma_{Lu} + e^{i\phi_L}\, \gamma_{Ld}) = t\, d_L\, \zeta_L, \qquad\qquad \zeta_L \equiv \gamma_{Lu} + e^{i\phi_L}\, \gamma_{Ld}, \tag{93}$$

inserting a charge from lead L (d_L) into the MBS tetron via the operator ζ_L. We will now explain how the relative phase ϕ_L determines the nature of the operator.

At $\phi_L = 0$, $\zeta_L = \gamma_{Lu} + \gamma_{Ld}$ corresponds to a MBS operator, which supports both regular tunneling ($|00\rangle \to |10\rangle$) and anomalous tunnelling ($|11\rangle \to |01\rangle$). Around this phase tuning, current will flow as described by Eq. (92).

Parity blockade is obtained by tuning the complex phase to an imaginary value, like at $\phi_L = -\frac{\phi}{2}$. At this point, $\zeta_L = \gamma_{Lu} - i\gamma_{Ld} = 2\, c_L^\dagger$ corresponds to a fermionic creation operator of the left occupation. This still supports regular tunnelling but prevents anomalous tunnelling. Considering the charge cycle shown in Eq. (92), the corresponding transition is now prohibited

$$|00\rangle \rightarrow |10\rangle \rightarrow |11\rangle \not\rightarrow |01\rangle \rightarrow |00\rangle \,. \tag{94}$$

As a consequence, transport is interrupted and the system gets stuck in the blocking state

$$|\psi\rangle = |11\rangle \,. \tag{95}$$

Tuning the phase to $\phi_L = \frac{\pi}{2}$ leads to $\zeta_L = 2\, c_L$ and the blocking state $|00\rangle$ instead. Parity blockade at the source induces explicitly only blocking states with total even parity, as it prohibits a process where a charge would tunnel into the system. Inducing parity blockade instead at the drain via Φ_R leads to blocking states $|01\rangle\,, |10\rangle$, each for one specific phase $\phi_R = \pm\frac{\pi}{2}$.

Generalizing the charge cycle description and parity blockade

Next, we want to generalize this procedure by considering a general system coupling one lead to N MBSs γ_k with tunnel couplings t_k. Schulenborg et al. showed in [107] that it is always possible to rotate the basis of N MBSs coupled to a lead such that $N-2$ are decoupled and exactly two are left coupling to the lead, see Figure 28. We denote these MBSs γ_1' and γ_2' with couplings t_1', t_1'. γ_1' and γ_2' describe the fermionic state that an electron can tunnel into (from the lead) or out of (into the lead).

As every system of K fermionic occupations can be described as $2K$ MBSs, this statement is also valid for general fermionic systems. Therefore, this rotation can in principle be applied to any transport setup. However, to achieve a full charge cycle description, it is necessary to apply a unitary transformation for each lead coupling to fermions. These transformations have to commute with each other, which is, in general, not the case. In our

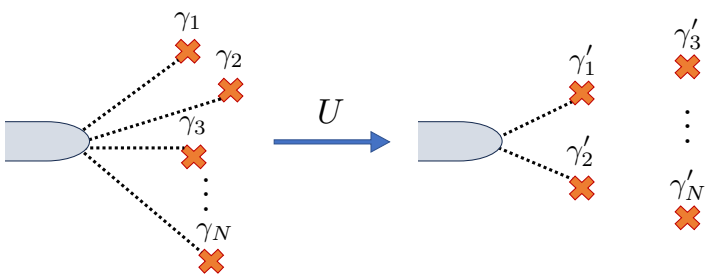

Figure 28: Sketch of a lead (gray) coupling to N MBSs. After application of a unitary basis transformation U, only two MBSs γ_1', γ_2' are coupling to the lead. The remaining MBSs $\gamma_{3,\ldots,N}'$ are decoupled.

systems, however, the commutation is guaranteed as the different leads couple to different sets of MBSs.

To establish parity blockade, we tune the couplings t_1', t_2' of this transformed MBS basis to the condition $t_2' = \pm i t_1'$. At this parameter point, the degree of freedom that the lead couples to appears like a true fermion/hole as described for Eq. (93). As t_1' and t_2' are functions of all tunnel couplings t_k, this is, in general, a non-trivial task experimentally. However, theory guarantees the existence of a general solution [107] given by

$$\sum_k t_k^2 = 0, \tag{96}$$

equivalent to the blockade in t_1', t_2'. Parity blockade is the underlying principle for all results presented in the following.

12.2 Paper I

The main goal of the first publication is to suggest experiments to initialize MBS tetrons and measure their quality via DC transport. In particular, our proposals solve two difficulties: Characterizing the lifetime of MBS tetrons and distinguishing the MBS tetron from the disordered MBS tetron. All experimental proposals are based on blocking the current via parity blockade.

Transport setup for disordered tetron

Before discussing the main results, we start by introducing the transport setup for the disordered tetron. It consists of the system Hamiltonian

$$H_{\text{sys}}^{\text{dis}} = \sum_{\substack{m=u,d \\ r=L,R}} \frac{i}{2} \varepsilon_{rm} \gamma_{rm} \tilde{\gamma}_{rm} + \sum_{m=u,d} \frac{i}{2} \Omega_m \tilde{\gamma}_{Lm} \tilde{\gamma}_{Rm} + E_C (N - n_g)^2, \tag{97}$$

introduced in subsection 9.1, connected to the leads via a generalized coupling Hamiltonian

$$H_T^{\text{dis}} = \sum_{ls} t_{ls} d_l \gamma_{ls} + \tilde{t}_{ls} d_l \tilde{\gamma}_{ls} + h.c.. \tag{98}$$

As shown in section 10 the couplings $\tilde{t}_{ls}$ to the additonal MBSs $\tilde{\gamma}_{ls}$ have to fullfill

$$\arg(\tilde{t}/t) = i,^4 \tag{99}$$

to interpolate via their absolute value $|\tilde{t}_{ls}|$ between fully disconnected MBSs inside the wire, $\tilde{t}_{ls} = 0$, and trivial fermionic states, $|\tilde{t}_{ls}| = |t_{ls}|$. As for the MBS tetron, the hybridizations are chosen to be much smaller than the tunneling rate, which in turn is much smaller than the charging energy

$$\varepsilon_m, \Omega_m \ll \Gamma \ll E_C. \tag{100}$$

We will use this model to compare the following results obtained for the MBS tetron with results obtained for an imperfect/disordered tetron.

Initializing tetrons and quantifying their lifetimes

The first direct consequence of parity blockade is the possibility to project the tetron into a well-defined state by applying parity blockade either on the left lead

$$\phi_L = \frac{\pi}{2} \;\rightarrow\; |\psi\rangle = |00\rangle\,, \qquad\qquad \phi_L = -\frac{\pi}{2} :\rightarrow\; |\psi\rangle = |11\rangle\,, \tag{101}$$

or the right lead

$$\phi_R = \frac{\pi}{2} \;\rightarrow\; |\psi\rangle = |01\rangle\,, \qquad\qquad \phi_L = -\frac{\pi}{2} :\rightarrow\; |\psi\rangle = |10\rangle\,. \tag{102}$$

If both blockades are applied in parallel, the resulting state is a statistical mixture depending on imperfections in the blockade tuning or MBS hybridizations, which we consider next.

Small deviations of the setup from the perfect fine-tuned limits can break the parity blockade and cause a remnant current I_{rem}. We model two sources for escape rates from the blockade: Finite overlaps between the MBSs in the upper and lower nanowire ($\bar{\varepsilon} = \varepsilon_u + \varepsilon_d$) and deviations from the blockade sweet-spot either in the absolute value of the amplitude $|\frac{t_{Lu}}{t_{Ld}}| = 1 - \delta_t$ or in the complex phase angle $\phi_L = -\frac{\pi}{2} + \delta_\phi$. We can summarize their effect in the following charge cycle

$$|00\rangle \xrightarrow{\bar{\varepsilon}} |10\rangle \rightarrow |11\rangle \overset{\delta}{\not\rightarrow} |01\rangle \rightarrow |00\rangle\,, \tag{103}$$

where $\delta^2 = \delta_t^2 + \delta_\phi^2$ is the remnant tunneling rate despite the blockade introduced by both deviations, and the overlaps between the MBSs introduce a unitary rotation between $|00\rangle$ and $|11\rangle$.

[4]The relative phase of tunnel amplitude was incorrectly chosen as $\tilde{t}_{ls} = t_{ls}$ in paper I. It can be shown that $\tilde{t} = t$ can be mapped to $t' = \sqrt{2}t$, $\tilde{t}' = 0$ corresponding to the case of an MBS inside the wire. We recalculated all numerical results with the correct phase and confirmed that the remnant current, as presented in Figure 30 (b) (green curve), is still constant.

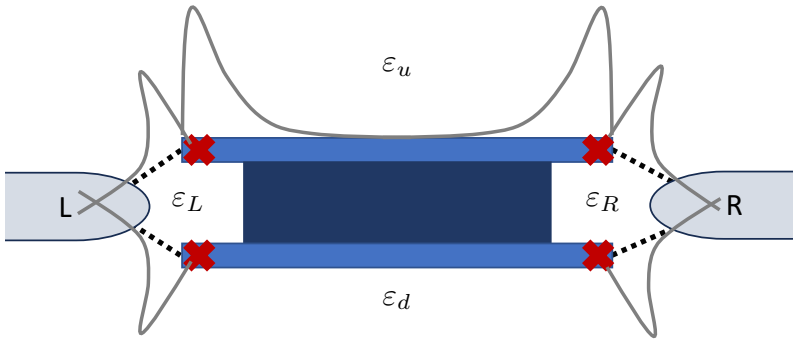

Figure 29: Representation of overlaps between the different MBSs of the tetron. $\varepsilon_{u,d}$ are introduced by the exponentially decaying wavefunction overlaps of the upper and lower pair of MBSs. $\varepsilon_{L,R}$ are introduced by overlaps due to the common coupling of two MBSs to the same lead.

For small deviations, $\delta_t, \delta_\phi \ll 1$, the solution for the remnant current to leading order in δ is

$$I^{\delta}_{\text{rem}} = 2e\,\delta^2\Gamma, \tag{104}$$

and in leading order of $\bar{\varepsilon}/\Gamma$

$$I^{\bar{\varepsilon}}_{\text{rem}} = \bar{\varepsilon}^2/\Gamma(1+I_P^2). \tag{105}$$

The inverse proportionality of $I^{\bar{\varepsilon}}_{\text{rem}}$ to Γ can be understood in terms of the quantum Zeno effect [122]. The overlaps introduce a rotation out of the blocking state $\propto (\bar{\varepsilon}\,t)^2$ (from the rotation $\cos(t\bar{\varepsilon})$). Electrons trying to enter from the lead repeatedly probe the state of the tetron at a rate Γ. The higher the rate of these measurements, the higher the probability that the tetron gets projected back into the blocking state, thereby enforcing the blockade. The different dependencies on Γ allow us to distinguish between deviations and overlaps as sources of the remnant current. The factor $1/(1+I_P^2)$ in Eq. (105) is due to the Lamb shift introduced by the coupling to the leads. This Lamb shift corresponds to a shift of the energy levels induced by the coupling to the leads. We can rewrite the Lamb shift into overlaps between MBSs on the left (ε_L) and right (ε_R) ends of the tetron as

$$\varepsilon_r = -2\Gamma I_P \sin\phi_r, \tag{106}$$

which is mediated via the common coupling to the respective lead r, see Figure 29. For our choices of chemical potential μ, temperature T, and bandwidth K of the leads, I_P is a factor of the order of $1-10$ characterizing the dependency of the Lamb shift on the leads.

Of more importance are two other dependencies in Eq. (106). First, the order of magnitude for the Lamb shift overlap is set by the tunneling rate, $\varepsilon_r \sim \Gamma$, which makes it a lot larger than the overlap introduced in the wires $\varepsilon_{L,R} \gg \varepsilon_{u,d}$. Whereas $\varepsilon_{u,d}$ introduces an escape rate out of the blocking state, the Lamb shift overlap is aligned with the blocking basis. This counteracts the rotation out of the blockade and motivates us to introduce an effectively decreased escape rate $\tilde{\bar{\varepsilon}} \equiv \bar{\varepsilon}/\sqrt{1+I_P^2}$.

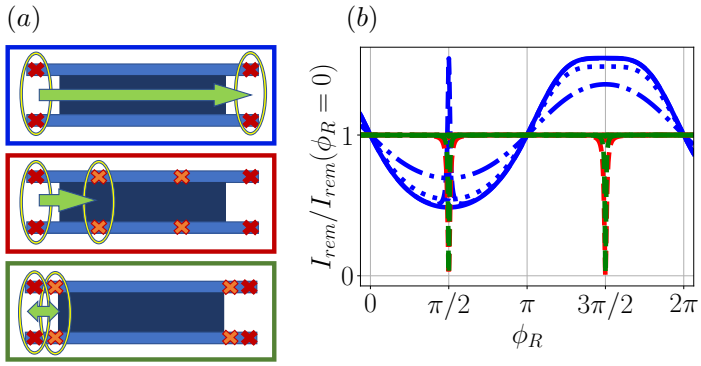

Figure 30: (a) Depiction of the dominant escape rates from the parity blockade for the different models. The overlaps between left and right pairs of MBSs introduce an escape rate depending on both leads for the MBS tetron (blue). This is not the case for the disordered MBS tetron in either limit of disconnected MBSs inside the wire (red) or ABSs (green). (b) The remnant current as a function of ϕ_R showing a qualitatively different dependence for MBS tetron (blue) compared to the disordered MBS tetron (red and green).

Second, the Lamb shift overlap depends on the relative phase ϕ_r set by the magnetic flux at the respective connection. The blockade at the left lead requires us to fix $\phi_L = \pi/2$. On the other hand, the relative phase on the right-hand connection is freely tunable. We can use it as a parameter to change the Lamb shift ε_R and, by that, the effective escape rate $\tilde{\tilde{\varepsilon}}(\phi_R)$. Tuning this will directly result in a change of the remnant current $I_{\text{rem}}(\phi_R)$. This is explicitly different for the disordered MBS tetron. In that model, the leading escape rate doesn't connect the left pair of MBSs via an overlap to the right pair. Instead, the escape rate is set by overlaps with the additional MBSs inside the tetron, which is independent of ϕ_R, see Figure 30.

Summing the proposed experiments up, measuring the remnant DC current under parity blockade enables access to the effective escape rate $\tilde{\tilde{\varepsilon}}$ of the tetron, thereby quantifying the quality of the tetron. The fine-tuning of the blockade needs to be sufficiently good to make this escape rate the dominant source for remnant current. The sources can be distinguished by their different dependence on the tunneling rate Γ, see Eq. (104) and Eq. (105). Furthermore, establishing the blockade on the left lead and varying the flux Φ_R on the right allows us to distinguish between the MBS tetron and the disordered MBS tetron.

12.3 Paper II

In the second publication, we propose a protocol that implements a fusion rule experiment via parity blockade in different tunnel coupling configurations. This protocol is capable of distinguishing between systems holding MBSs and ABSs.

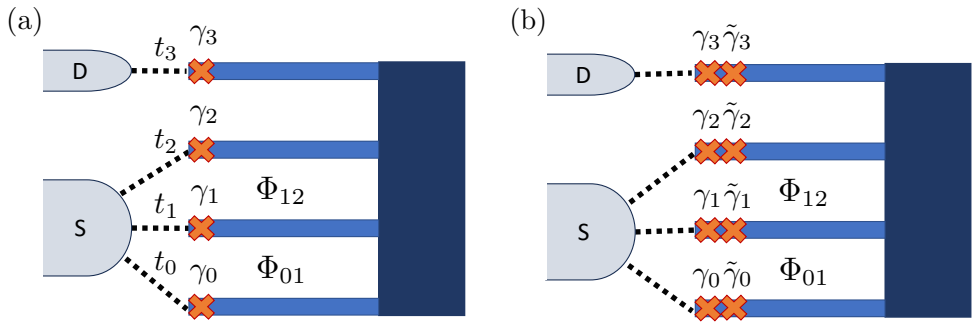

Figure 31: (a) Transport setup for the asymmetric MBS qubit. The source couples to the MBSs $\gamma_{0,1,2}$. To tune the relative phases, we thread two magnetic fluxes Φ_{01}, Φ_{12} through the connections with the source. The drain connects to γ_3. (b) Transport setup for the asymmetric ABS tetron. The leads connect to two MBSs on each site s.

The asymmetric transport setup

We start by introducing the transport setup for the asymmetric MBS tetron, shown in Figure 31, both in the topological (a) and ABS (b) versions.

First, we discuss the topological setup in Figure 31 (a). The system holds four nanowires labelled by $s = 0, 1, 2, 3$, each containing one MBS at its end. As before, the bias voltage is tuned to define one source and one drain. But the key difference to the previous setup is that the source connects to the first three MBSs $\gamma_0, \gamma_1, \gamma_2$ and the drain to γ_3. The tunnel Hamiltonian defining these connections is an adapted version of Eq. (90). The source connections define three different paths into the tetron, which are tuned via absolute values $|t_l|$ and phases adjusted via two magnetic fluxes Φ_{01}, Φ_{12}. To enable current flow, we choose one fixed connection to the source with $t_1 = t$ and the drain with $t_3 = t$. For both connections, we make use of the gauge degree of freedom to set $t_1, t_3 \in \mathbb{R}$. This leaves us with four degrees of freedom. The absolute values $|t_0|, |t_2|$ and complex phases ϕ_0, ϕ_2.

As in paper I, the gate voltage is tuned to establish degeneracy between N (even total parity) and $N+1$ (odd total parity) electrons. We choose the Fock basis for the low-energy Hilbert space by combining γ_0 with γ_1 and γ_2 with γ_3, and obtain

$$|\psi\rangle = |n_{01}, n_{23}\rangle\,, \tag{107}$$

residing in a fourfold degenerate ground state sector

$$|\psi\rangle \in \{|00\rangle\,, |11\rangle\,, |10\rangle\,, |01\rangle\}. \tag{108}$$

It is important to highlight that something is missing in this model. MBSs are always created in pairs. Accordingly, each nanowire should host two MBSs at the boundary from the topological to the trivial regime. Therefore, a precise description would include MBSs at the connection between the topological nanowire and the trivial superconductor. This model

can be seen as an effective model, where these degrees of freedom are fully disconnected and fixed to even parity, which simplifies the later charge cycle description significantly.

The asymmetric ABS tetron is a generalization of the asymmetric MBS tetron and includes the additional MBSs needed for a full description. At the same time, it provides a description of trivial fermionic states. In this model, each nanowire s contains one fermionic degree of freedom, described by the Fock state

$$|\psi\rangle = |n_0, n_1, n_2, n_3\rangle \,. \tag{109}$$

We describe each fermionic state as a pair of MBS operators, as explained in section 5.

The transport geometry for the asymmetric ABS tetron is the same as for the asymmetric MBS tetron. The only difference lies in the number of MBSs connecting to the source and drain. Each site s hosts two MBSs, γ_s and $\tilde{\gamma}_s$. We choose the MBS basis in such a way that both MBSs connect to the respective lead with the same absolute value of the tunneling amplitude, $|t_s| = |\tilde{t}_s|$. This leaves one undetermined degree of freedom per site s in the form of the complex relative phase θ_s between the tunneling amplitudes $\tilde{t}_s = e^{i\theta_s} t_s$. This degree of freedom can vary in the interval $[0, 2\pi]$. It interpolates between the limits of MBSs $\theta_s = 0, \pi$ and conventional ABSs $\theta_s = \frac{\pi}{2}, 3\frac{\pi}{2}$. There exists a bijective mapping between the parametrization via $\theta \in [0, \frac{\pi}{2}]$ and the interpolation between MBS and trivial states parametrized with fixed complexe phase $\tilde{t}_s = i\, t_s$ and varying tunnel coupling $|\tilde{t}| \in [0, |t|]$ introduced in section 10.

The transport-based fusion protocol

The fusion rule protocol is implemented by switching between two different coupling setups implementing parity blockade on the asymmetric MBS tetron, see Figure 32. In both blocking setups, the drain connects to the tetron via γ_3 with amplitude t. In the first blocking setup, Figure 32 (a), the source connects to the MBSs γ_0 and γ_1 with the same tunneling

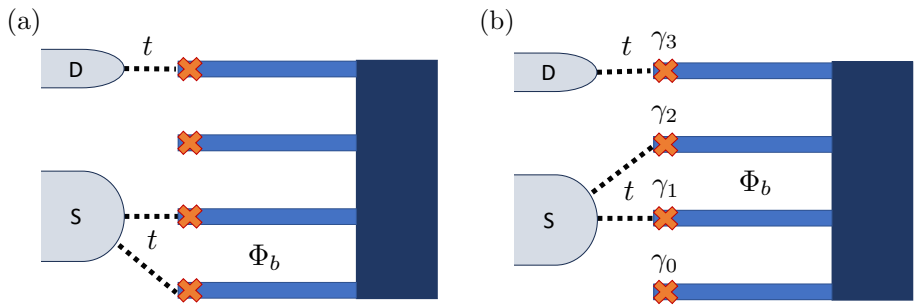

Figure 32: The two different blocking setups for the protocol. (a) Parity blockade in the connections γ_0, γ_1 corresponds to a projection along the occupation n_{01}. The protocol compares this to (b) a parity blockade projecting on the basis of γ_1, γ_2, thereby accessing the fusion rules.

amplitude t but is disconnected from γ_2. The magnetic flux through this loop is tuned into the blockade condition $\Phi_{01} = \Phi_b$. This blockade projects the system onto the blocking state

$$|\psi_z\rangle = |00\rangle\,, \tag{110}$$

expressed in the basis choosen in Eq. (108), where we combined γ_0 with γ_1 and γ_2 with γ_3. We denote it as the z-blockade because the blocking state represents an eigenstate of the Pauli matrix σ_z in the basis $\{|00\rangle\,, |11\rangle\}$ of the even total parity subspace. For the second blocking setup, Figure 32 (b), the tetron connects to γ_1 and γ_2 with t and is disconnected from γ_0. Again, a blockade is established via the magnetic flux $\Phi_{01} = \Phi_b$. We denote this setup as the x-blockade with the blocking state

$$|\psi_x\rangle = \frac{1}{\sqrt{2}}(|00\rangle + |11\rangle). \tag{111}$$

The idea for the fusion protocol is to use the parity blockade to measure and thereby project the tetron into the respective blocking state of the blocking setups. This is done by repeatedly switching between both setups and measuring the average amount of transferred charge, meaning the DC current.

Let's assume that we start in the x-blockade, with a perfect projection on $|\psi_x\rangle$. We then disconnect the tetron and reconnect it in the z-blockade. The dynamics for the time evolution into the new blocking state are summarized in the following charge sequence:

$$|\psi_x\rangle = \frac{|00\rangle + |11\rangle}{\sqrt{2}} \Rightarrow \begin{cases} |00\rangle \\ |11\rangle \rightarrow |01\rangle \rightarrow |00\rangle \end{cases}\,, \tag{112}$$

The initial state of the system is given by $|\psi_x\rangle$. A charge tries to enter the tetron via the connection to γ_0, γ_1, thereby measuring the occupation n_{01}. Depending on the outcome of that measurement, the system gets projected on $|00\rangle$ or $|11\rangle$. In the first case, the system directly reaches the z-blockade without any charge transfer. In the latter case, the charge can enter the tetron, projecting it onto $|01\rangle$. Afterwards, a charge can tunnel out of the tetron into the drain, eventually projecting the system onto the blocking state $|00\rangle$. Both cases happen with a 50 percent probability, which means an average charge transfer of $e/2$ for this switch. It is straightforward to show that the other way around (initializing in $|\psi_z\rangle$ and projecting onto $|\psi_x\rangle$) transfers the same amount of charge. A full protocol cycle includes switching from x- to z- and back to x-blockade, which transfers 1 e on average. Performing the protocol cycles with a frequency f leads to an average current $I = fe$.

We compare this intuitive picture with a numerical simulation calculating the average amount of transferred charge of a full protocol cycle over a protocol time $\tau \propto \frac{1}{f}$. This numerical simulation confirms the intuitive picture, which is confirmed by the plateau of

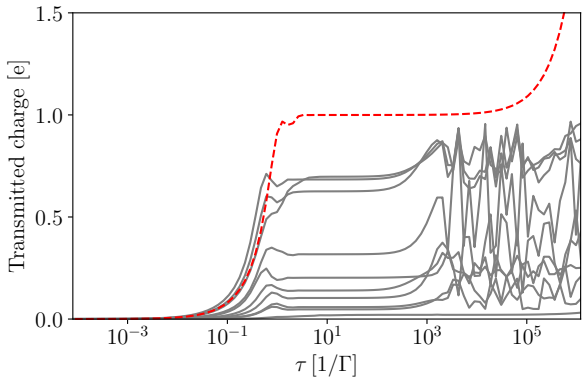

Figure 33: The transmitted charge of the fusion protocol as a function of the waiting time τ on a logarithmic axis. The result for the asymmetric MBS tetron (red dotted line) shows a monotonous dependence on the waiting time with a plateau at 1 e. This is compared to the gray curves, which represent the transmitted charge of the protocol for different realizations of the asymmetric ABS tetron. Each realization is obtained by randomly drawing four different $\theta_{0,1,2,3}$ from a uniform distribution $[0, 2\pi]$. None of the imperfect setups replicates the same monotonous behaviour or quantized plateau.

the red line at $\tau \approx 10^1 - 10^5$ in Figure 33. Next, we apply the simulation also to the generalized model, which yields several additional insights. First, it confirms the equivalence of the fusion protocol result between the effective model and the generalized model at $\theta_l = 0, \pi$. Second, it shows how this plateau appears at a different value for imperfect systems $\theta \neq 0, \pi$, see gray lines in Figure 33.

Furthermore, we investigate the effect of a finite protocol time τ on the amount of transmitted charge. The lower bound is given by the tunneling rate Γ. The protocol frequency needs to be sufficiently slow to enable the tunnel events described in Eq. (112). This can be seen by the rapid suppression of all curves at $\tau \leq 1/\Gamma$. The upper bound is determined by the remnant current discussed in paper I, which we modelled via small MBS overlaps $\varepsilon \propto 10^{-3}\,\Gamma$, which yields a significant contribution at large protocol times $\tau \geq 10^5/\Gamma$. A remnant current via imperfect tuning of the blockade δ would have led to the same qualitative behaviour. We can summarize the restrictions on the protocol times as

$$\Gamma^{-1} \ll \tau \ll \left(\bar{\varepsilon}^2/\Gamma\right)^{-1}, \left(\delta^2\,\Gamma\right)^{-1}. \tag{113}$$

In between these limits, we find the predicted plateau of 1 e consistent with the explanations from Eq. (112). We envision an experiment that aims at detecting this plateau. Experimentally detecting this plateau confirms the measurement of fusion rules and of MBSs instead of trivial ABSs.

13 Summary and discussion for paper III

In paper III, we introduce the minimal version of an MBS tetron (section 9) built via QD-based minimal Kitaev chains (subsection 6.2) called the poor man's Majorana tetron (PMMT). We will begin by constructing the model by connecting two minimal Kitaev chains into a charge island. We will discuss in detail the effect of the introduced charging energy on the ground state sector of the PMMT. Afterwards, we describe a transport setup in which the PMMT exhibits the topological Kondo effect (subsection 11.2) and the standard Kondo effect emergent in the Anderson impurity model (subsection 11.1) at different parameter regimes.

13.1 Revisiting the minimal Kitaev chain

The basic building block for the PMMT is the minimal Kitaev chain consisting of two sites introduced in subsection 6.2. We will start by taking a closer look at the ground state sector of the minimal Kitaev chain.

In the simplest version, the minimal Kitaev chain consists of two spin-polarized QDs ($a = L, R$) each tunnel coupled to a middle QD (SC) proximitized by a superconductor described by

$$H_{\text{mKC}} = \sum_{a=L,R} \mu_D \, d^\dagger_{a\downarrow} d_{a\downarrow} + \sum_{s=\uparrow,\downarrow} \mu_{SC} \, c^\dagger_s c_s + (\Delta \, c^\dagger_\uparrow c^\dagger_\downarrow + h.c.) - \sum_{a=L,R} t_a (e^{-ia\alpha\sigma_y})_{s\downarrow} \, c^\dagger_s d_{a\downarrow}. \tag{114}$$

The tunneling includes the effect of Rashba spin-orbit coupling that rotates the spin by an angle α orthogonal to the spin-polarization introduced by a strong magnetic field on the outer QDs. We apply the following sign convention for $a : (L = +, R = -)$ to account for the direction of the tunnelling process. For a more detailed treatment, including spins on the outer QDs and magnetic fields applied to all QDs, see paper III. Also, for simplicity, we choose the chemical potential on both outer QDs to be the same μ_D.

As explained in [77] and subsection 6.2, the central QD mediates an effective second-order coupling between the outer QDs. First, the ABSs are obtained by diagonalizing the Hamiltonian in the central QD. Afterwards, the effective Hamiltonian without ABSs is calculated by applying a Schrieffer-Wolff transformation on virtual occupations of the ABS

$$H^{\text{eff}}_{\text{mKC}} = \sum_{a=L,R} \mu_D \, d^\dagger_{a\downarrow} d_{a\downarrow} + (t_{\text{cot}} \, d^\dagger_L d_R + \Delta_{\text{CAR}} \, d^\dagger_L d^\dagger_R + h.c.). \tag{115}$$

Eq. (115) conserves total parity $P = \pm$. At $\mu_D = 0$, the diagonalization is straightforward,

and we find one ground state in the even (+) and odd (−) sectors, respectively

$$|+\rangle = \frac{1}{\sqrt{2}}(|00\rangle - |11\rangle), \qquad |-\rangle = \frac{1}{\sqrt{2}}(|01\rangle - |10\rangle), \tag{116}$$

with energies

$$E_+ = -\Delta_{\mathrm{CAR}}, \qquad E_- = -t_{\mathrm{cot}}, \tag{117}$$

The tunability of Δ_{CAR} and t_{cot} explained in subsection 6.2 allows us to tune to the sweet spot $\Delta_{\mathrm{CAR}} = t_{\mathrm{cot}}$ such that we obtain a degenerate ground state sector reminiscent of the perfectly localized zero-energy MBSs on the left and right QDs.

13.2 The poor man's Majorana tetron

In the next step, the poor man's Majorana tetron (PMMT) is designed by combining two minimal Kitaev chains ($\tau = u, d$) into a tetron design, as shown in Figure 34 (a). Importantly, the shared charging energy is achieved by combining the superconductors proximitizing their central QDs into one floating island

$$H_{\mathrm{PMMT}} = \sum_{\tau=u,d} H_{\mathrm{mKC},\tau} + H_c, \qquad H_c = E_C\,(N - n_g)^2, \tag{118}$$

with a shared charging energy E_C, charge N on the island, and excess charge n_g tunable via an external electric gate. Importantly, we assume that this connection introduces no tunnel

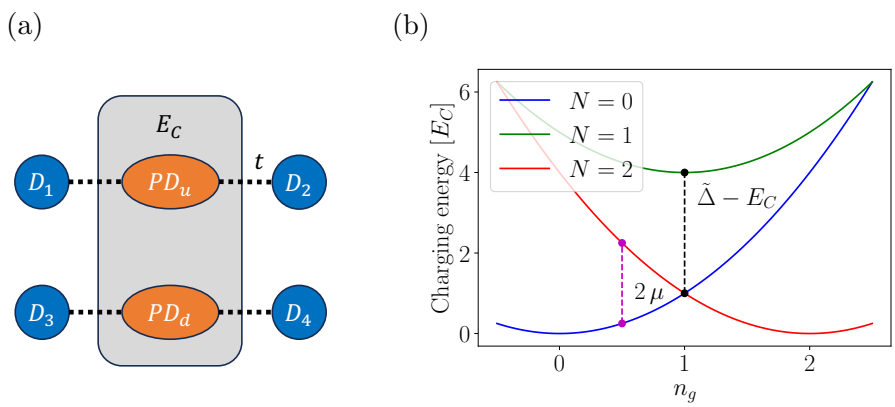

Figure 34: (a) Two QD-based minimal Kitaev chains with in total four QDs, $D_{1,2,3,4}$, tunnel coupled to the central QDs $PD_{u/d}$ combined into the poor man's tetron, with a shared charge island via the proximitizing superconductor. (b) The charging parabolas depicting the charge states of the three lowest energy charge states, $N = 0, 1, 2$, as a function of n_g. The splitting between the two lowest states is compensated by the tuning $2\mu_D$, defining $N = 1$ as the lowest high-energy state split off by $\tilde{\Delta} - E_C$.

coupling between the central QDs. We consider the charging energy to be smaller than the generalized superconducting gap $\tilde{\Delta} = \sqrt{\Delta^2 + \mu_{SC}^2}$. By choosing $\mu_D = 2E_C(1 - n_g)$ for all outer QDs, we establish degeneracy between the charge states $N = 0$ and $N = 2$ around the considered parameter region $0 < n_g < 2$, see Figure 34 (b). This choice establishes the charge states $N = -1, 1, 3$ as the high-energy states split off by $\Delta E \geq \tilde{\Delta} - E_C$, which mediate the effective coupling between the outer QDs.

The effective couplings of the PMMT

Equivalent to the minimal Kitaev chain, we perform a Schrieffer-Wolff transformation to calculate the effective coupling between the outer QDs. However, the shared charging energy and its effect on the higher excited states need to be taken into account during the calculation. The crossed Andreev reflection

$$\Delta_{\mathrm{CAR}} = t^2 \sin(2\alpha) \frac{\sqrt{\tilde{\Delta}^2 - \mu_{SC}^2}}{\tilde{\Delta}(\tilde{\Delta} - E_C)}, \tag{119}$$

stays qualitatively the same with an additional dependency on E_C that is of no crucial importance in the considered limit $E_C < \Delta$. On the other hand, the elastic cotunneling

$$t_{\mathrm{cot}}(N = 1 \pm 1) = t^2 \cos(2\alpha) \frac{\mu_{SC}\tilde{\Delta} + \mu_{SC}E_C \mp 2E_C\tilde{\Delta}}{\tilde{\Delta}(\tilde{\Delta} + 3E_C)(\tilde{\Delta} - E_C)}, \tag{120}$$

is now dependent on the central charge N, see Appendix A of paper III for a derivation. This charge dependence N has implications for the ground states, as we will see next.

The low-energy sector of the PMMT

Apart from the effective couplings, the ground states are also affected by the charging energies. In the limit $E_C \to 0$, the ground states are simple product states of the respective systems

$$|P_u, P_d\rangle = |P_u\rangle \otimes |P_d\rangle\,, \tag{121}$$

witht the states $|P_\tau\rangle$ defined in Eq. (116). Translating these ground states correctly into the ground states for $E_C > 0$ is simplified by re-expressing them in terms of the conserved total charge

$$N_t = N + \sum_{a,\tau} n_{a,\tau}, \tag{122}$$

which together with the lower parity P_d fully characterizes the conservation of total charge and local parities via the states $|N_t P_d\rangle$. The low-energy spectrum consists of six states. Two

of them hold an odd total charge $N = 3$

$$\begin{aligned} |3+\rangle &= \frac{1}{\sqrt{2}} \left[\cos\theta \left(|0100, 2\rangle - |1000, 2\rangle\right) + \sin\theta \left(|0111, 0\rangle - |1011, 0\rangle\right)\right], \\ |3-\rangle &= \frac{1}{\sqrt{2}} \left[\cos\theta \left(|0001, 2\rangle - |0010, 2\rangle\right) + \sin\theta \left(|1101, 0\rangle - |1110, 0\rangle\right)\right], \end{aligned} \tag{123}$$

where the angle

$$\theta = \frac{1}{2} \arctan\left(\frac{2\Delta_{\mathrm{CAR}}}{t_{\mathrm{cot}}(0) - t_{\mathrm{cot}}(2)}\right), \tag{124}$$

is a direct consequence of the charge dependence of $t_{\mathrm{cot}}(N)$ that introduces cross-talk between the upper and lower systems. This effect converges to $\theta \to \pi/4$ in the limit $E_C \to 0$ as predicted by the product states of Eq. (121).

The even total charge states divide into two classes. The first class is maximally simple as it describes two even total charge states that are not affected by the charging energy

$$|2m-\rangle = \frac{1}{2} \left[|0101, N_t - 2\rangle - |0110, N_t - 2\rangle - |1001, N_t - 2\rangle + |1010, N_t - 2\rangle\right], \tag{125}$$

with $m = 1, 2$. This stems from the fact that states in this class exclusively couple via t_{cot}, which leaves the central charge invariant, thereby avoiding cross-talk between the upper and lower system.

The second class of even total charge states, on the other hand, couples states exclusively via Δ_{CAR}, which maximizes cross-talk between the systems as it couples states with three different charges N on the island. We choose the tunnel couplings t^2 small enough to ensure the limit $E_C \gg \Delta_{\mathrm{CAR}}$, where we find the eigenstates

$$\begin{aligned} |2+\rangle &= \frac{1}{2} |0011, 0\rangle + \frac{1}{2} |1100, 0\rangle + \frac{1}{\sqrt{2}} |0000, 2\rangle, \\ |4+\rangle &= \frac{1}{2} |0011, 2\rangle + \frac{1}{2} |1100, 2\rangle + \frac{1}{\sqrt{2}} |1111, 0\rangle. \end{aligned} \tag{126}$$

Each of them consists only of three states as their fourth components ($|1111, -2\rangle$ for $|2+\rangle$ and $|0000, 4\rangle$ for $|4+\rangle$) are split off by the large charging energy.

Around $n_g \approx 1$, the ground state sector consists of the degenerate states $|3, \pm\rangle$. The closest excited states are the even states $|2, \pm\rangle, |4, \pm\rangle$ split of by

$$\begin{aligned} \delta E_{+}^{(N_t=3\pm1)} &\equiv E^{(N_t=3\pm1,+)} - E^{(3)} \approx \pm\mu - \left(\sqrt{2} - 1\right) \Delta_{\mathrm{CAR}} + \bar{t}_{\mathrm{COT}}, \\ \delta E_{-}^{(N_t=3\pm1)} &\equiv E^{(N_t=3\pm1,-)} - E^{(3)} \approx \pm\mu - \bar{t}_{\mathrm{COT}} + \Delta_{\mathrm{CAR}}, \end{aligned} \tag{127}$$

where we defined $\bar{t}_{\mathrm{cot}} = \frac{t_{\mathrm{cot}}(0)+t_{\mathrm{cot}}(2)}{2}$. This situation already closely resembles the state configuration of the topological Kondo effect as introduced in subsection 11.2. In the following, we will establish the necessary parameter adjustments to replicate the topological Kondo effect with the PMMT.

13.3 The three-lead Kondo model of the PMMT

We will focus on the simplest transport setup achieving the topological Kondo model by connecting three external leads as shown in Figure 35. With leads as introduced in subsection 10.2 and a tunneling Hamiltonian

$$H_{\mathrm{T}} = \sum_{\alpha=1,2,3} J_\alpha l_\alpha^\dagger d_\alpha + h.c.\,, \tag{128}$$

connecting each QD D_α to a degree of freedom in the electric lead created by $l_\alpha^\dagger$ with the tunneling amplitude J_α.

The topological Kondo effect of the PMMT

As with the setup for the topological tetron explained in subsection 11.2, to observe the topological Kondo effect we choose the tunnel couplings, chemical potentials and temperatures of all leads to be smaller than the energy splitting to the excited states $J_\alpha, \mu_\alpha, T_\alpha \ll \delta E_\pm^{N_t}$.

In this limit, the degenerate ground state sector acts as a spin-$\frac{1}{2}$ impurity coupled to three leads with tunneling-induced virtual occupations of the excited states as shown in Figure 36. These virtual occupations can lead to flips of the effective spin, thereby establishing the Kondo physics. A crucial difference to the original setup is the unequal energy splittings of the excited states, as shown by Eq. (127). These energy splittings are functions of Δ_{CAR} and t_{cot}, which are determined by the tunings of the gates n_g and μ_{SC}. The effective Hamiltonian

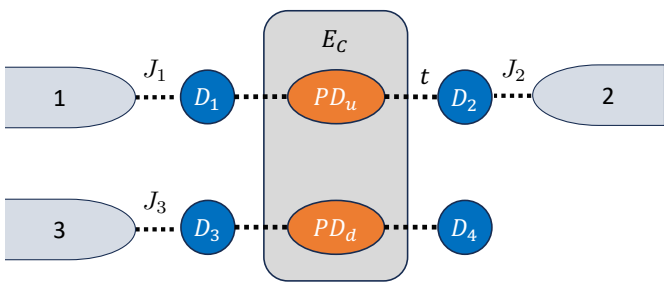

Figure 35: A transport setup coupling three leads $\alpha = 1, 2, 3$ with tunnel couplings J_α to the PMMT establishing the Kondo physics in the limit of weak couplings, zero-bias, and low temperatures.

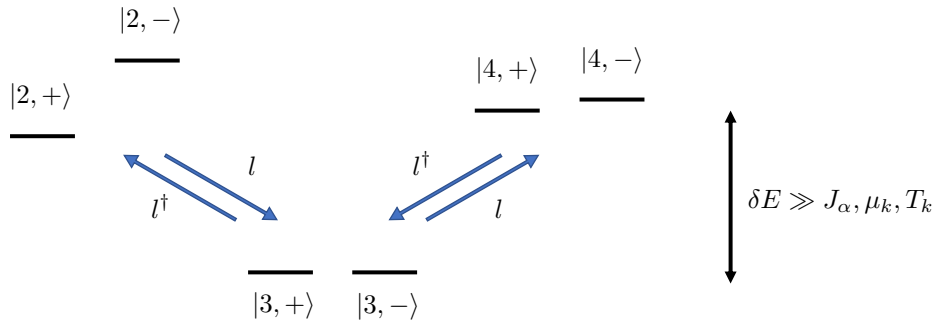

Figure 36: Virtual occupations of higher excited states in the topological Kondo setup of the PMMT. In comparison to the original topological Kondo setup, there is no mechanism guaranteeing the degeneracy of the excited states.

is obtained via a Schrieffer-Wolff transformation as

$$H_{\text{eff}} = H_{\text{TK}} + \delta H. \tag{129}$$

where H_{TK} represents the topological Kondo Hamiltonian as introduced in subsection 11.2. It also contains the perturbation δH driving the system away from the topological Kondo effect into a regime where it behaves like a spin-$\frac{1}{2}$ Anderson impurity model as introduced in subsection 11.1. This contribution stems from the unequal superposition building the states $|3,\pm\rangle$ with $\theta \neq \frac{\pi}{4}$, see Eq. (123), and the missing forth Fock state from the states $|2/4,+\rangle$, see Eq. (126). These imperfections are a direct result of cross-talk between the upper and lower minimal Kitaev chains due to charging energy. For a given transition via $N_t = 2$ or $N_t = 4$, these imperfections lead to an enhancement of the path via a virtual occupation of one parity state, $P_d = +$ or $P_d = -$, at the expense of the other. However, these transition amplitudes are also proportional to the energy splittings $\delta E^{N_t}_{P_d}$; therefore, we can compensate these unequal transition amplitudes by adjusting the energy splitting via the gates n_g, μ_{SC}. We identify the necessary tuning condition

$$\zeta^2_{N_t} = \frac{\delta E^{N_t}_{+}}{\delta E^{N_t}_{-}}, \tag{130}$$

with

$$\zeta_2 = \frac{1+\sqrt{2}\cot\theta}{2}, \qquad \zeta_4 = \frac{1+\sqrt{2}\tan\theta}{2}. \tag{131}$$

For a perfect tuning of n_g, μ_{SC}, exactly fulfilling Eq. (130), the transport setup would thus exhibit the non-Fermi liquid behaviour in the non-local conductance between the leads, introduced in subsection 11.2.

We further show in paper III that it is possible to simultaneously fulfill both conditions approximately by adjusting the available gates n_g, μ_{SC}.

Establishing the Anderson impurity model in the PMMT

We finalize our discussion by outlining how the Anderson impurity model is established by the transport setup in Figure 36. To make this behaviour explicit, we adjust the energy splittings $\delta E_{\pm}^{N_t}$; however, this time in order to enhance the effect of the perturbation δH. We consider the parameter point $\delta E_{+}^{N_t=2} = 0$ in which the state $|2,+\rangle$ is degenerate with the ground states $|3,\pm\rangle$ while the remaining states are split off.

In this parameter point, by neglecting all excited states, the transport setup can be mapped to H_{AIM}, introduced in subsection 11.1, in the limit of infinite charging energy of the impurity. In this mapping $|2,+\rangle$ resembles the vacuum state strongly coupled to the effective spins $P_\tau = \pm$ of the states $|3, P_\tau = \pm\rangle$ via the lead operators

$$l_+ \propto J_2^* l_2 - J_1^* l_1, \qquad\qquad l_- \propto J_4^* l_4 - J_3^* l_3, \tag{132}$$

which we generalized to include a fourth lead coupled with J_4. Due to the infinite interaction, processes flipping P_τ are suppressed, resulting in a vanishing differential conductance between the upper (1,2) and lower (3, 4) leads at zero bias.

14 Summary and discussion for paper IV

The goal of paper IV was to investigate new possibilities of hybridization-based braiding, in particular in QD-based Kitaev chains. As explained in subsection 6.2, current realizations of these chains consist only of two or three sites. Due to this length restriction, they are lacking the topological protection of a long chain, which makes them more vulnerable to imperfections like spatial MBS overlaps and MBS hybridizations. While the spatial overlaps are potentially problematic for many braiding protocols, we view the lack of protection against hybridizations as an opportunity. It enables us to hybridize neighboring MBS by gate-tuning their QDs away from the sweet spot.

In the following, we will begin by introducing an intuitive tool set, which we call MBS diagrammatics, to visualize the effect of MBS hybridizations on the ground state basis. Afterwards, we will apply this technique to illustrate the braiding of imperfect MBSs. The aim is to provide intuition to the analytically derived results of paper IV. This graphical intuition is crucial in order to discover new possibilities for the use of hybridizations to manipulate MBS systems.

14.1 An introduction to MBS diagrammatics

MBS diagrammatics is a graphical technique we developed, based on earlier ideas by [89], with several tools that illustrate an intuitive way to picture the diagonalization of networks of hybridizing MBSs. Hybridizations are represented by lines connecting two MBSs. The technique introduces several unitary basis transformations represented via graphical moves that diagonalize small subsets of networks. These techniques can be applied iteratively until the true low-energy state is displayed.

1. Move: Diagonalizing star networks

The first move is found by diagonalizing the Hamiltonian

$$H = i\gamma_0 \sum_k \varepsilon_k \gamma_k = i\Delta\gamma_0 \sum_k \frac{\varepsilon_k}{\Delta}\gamma_k = i\Delta\gamma_0\gamma_\Delta, \tag{133}$$

as was first introduced by [89].

A single MBS γ_0 hybridizing with ε_k to N MBS γ_k is equivalent to γ_0 coupling to a superposition of MBSs represented by a single γ_Δ and $N-1$ decoupled MBSs, see Figure 37. The hybridized MBS is given by

$$\gamma_\Delta = \sum_k \rho_k \gamma_k, \tag{134}$$

with the normalized amplitudes $\rho_k = \frac{\varepsilon_k}{\Delta}$ and the total gap $\Delta = \left(\sum_k \varepsilon_k^2\right)^{1/2}$. The ground state sector consists of the fermionic degrees of freedom of the uncoupled MBSs $\gamma'_{k\geq 2}$ and is defined by

$$i\gamma_0\gamma_\Delta = -1, \qquad P = \frac{1}{2}(1 - i\gamma_0\gamma_\Delta), \tag{135}$$

with the resulting projector P on the ground state sector.

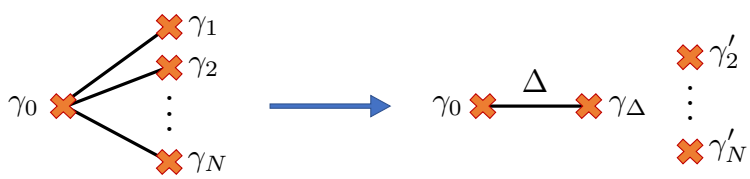

Figure 37: Graphical representation of the first move of MBS diagrammatics, which yields the gap Δ and the hybridized MBS γ_Δ in a star network.

Figure 38: Graphical representation of the second move of MBS diagrammatics, which splits up a hybridization chain of four MBS into two pairs of hybridized MBSs.

2. Move: Breaking up chains of MBSs

We find the simplest version of the second move by diagonalizing the following Hamiltonian

$$H = i\varepsilon_{01}\,\gamma_0\gamma_1 + i\varepsilon_{12}\,\gamma_1\gamma_2 + i\varepsilon_{23}\,\gamma_2\gamma_3 = i\Delta_{01}\,\gamma_0^D\gamma_1^D + i\Delta_{23}\,\gamma_2^D\gamma_3^D. \tag{136}$$

It breaks up a chain of four coupled MBSs into two groups, see Figure 38. Importantly, the move also predicts that the diagonalization rotates only next-nearest neighbors inside the chain

$$\gamma_0^D = \alpha\,\gamma_0 + \beta\,\gamma_2, \qquad \gamma_1^D = \mu\,\gamma_1 + \nu\,\gamma_3, \tag{137}$$
$$\gamma_2^D = \alpha\,\gamma_2 - \beta\,\gamma_0, \qquad \gamma_3^D = \mu\,\gamma_3 - \nu\,\gamma_1, \tag{138}$$

where the amplitudes α, β, μ, ν and the hybridization Δ_{01}, Δ_{23} can be found in the supplementary information of paper IV.

Solving the time-dependent manipulations of minimal star networks

Next, we will use the 1. move to solve the simplest version of a hybridization-based MBS exchange implemented via the following time-dependent Hamiltonian

$$H = i\varepsilon_1(\tau)\,\gamma_0\gamma_1 + i\varepsilon_2(\tau)\,\gamma_0\gamma_2, \qquad \varepsilon_2(\tau = 0) = 0, \qquad \varepsilon_1(\tau = T) = 0, \tag{139}$$

that switches between different hybridizations with a total protocol time $\tau \in [0, T]$. The process we model centers around a hybridization of γ_0. First, it only hybridizes with γ_1 at $(\tau = 0)$. At $0 < \tau < T$ the system continuously switches to a hybridization with γ_2 until γ_1 is decoupled at $(\tau = T)$, see Figure 39 (a). This is the fundamental step in hybridization-based braiding protocols as introduced in subsection 8.1. Accordingly, there exist plenty of solutions to describe the effect of this step on the ground state sector [85, 86, 89]. However, we will still discuss the solution in detail, as for the later derivation, it is crucial to develop an intuitive understanding of the induced transformation.

To solve this step, we introduce the angle

$$\omega = \arctan(\varepsilon_2/\varepsilon_1), \tag{140}$$

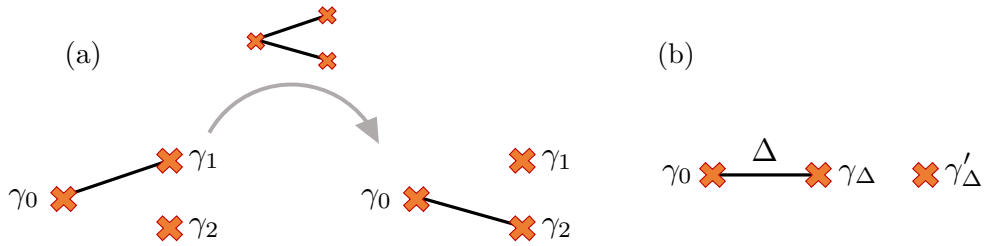

Figure 39: Graphical representation of a rotation induced via time-dependent hybridizations in a minimal star network $N = 2$ with a specific expression for the uncoupled MBS γ'_Δ.

parametrizing the step as a dimensionless quantity evolving from 0 to $\frac{\pi}{2}$. The hybridized MBS γ_Δ is given by the first move, and importantly, due to the minimum of three MBSs, there exists a unique solution for the uncoupled MBS γ'_Δ, see the supplementary information of paper IV,

$$\gamma_\Delta = \cos(\omega)\gamma_1 + \sin(\omega)\gamma_2, \qquad \gamma'_\Delta = \cos(\omega)\gamma_2 - \sin(\omega)\gamma_1, \tag{141}$$

illustrated in Figure 39 (b). The above expressions for γ_Δ and γ'_Δ already fully capture the effect of this process on the system. The implemented transformation U can directly be constructed from them, see paper IV for details.

Instead of repeating this construction here, we will use the Berry phase to formally determine the transformation. This basis parametrization comes with the convenient properties

$$\partial_\omega \gamma_\Delta = \gamma'_\Delta, \qquad \partial_\omega \gamma'_\Delta = -\gamma_\Delta. \tag{142}$$

This is crucial as the effect of the step on the ground state is described by the Berry phase [86, 123]

$$U = \mathcal{T} \exp\left(- \int_0^{\frac{\pi}{2}} [P, \partial_\omega P]\, d\omega \right), \tag{143}$$

which we introduced in subsection 8.1. In this representation, the Berry phase is a time-ordered exponential depending on the ground state projector $P = \frac{1}{2}(1 - i\gamma_0\gamma_\Delta)$, that we already know from Eq. (135) of the first move. Combining P with Eq. (141) and Eq. (142) we find

$$\partial_\omega P = -\frac{i}{2}\gamma_0\, \partial_\omega \gamma_\Delta, \tag{144}$$

$$\Rightarrow [P, \partial_\omega P] = \frac{1}{4}[1 - i\gamma_0\gamma_\Delta, -i\gamma_0\, \partial_\omega \gamma_\Delta] = -\frac{1}{4}[\gamma_0\gamma_\Delta, \gamma_0\gamma'_\Delta] = \frac{1}{4}[\gamma_\Delta, \gamma'_\Delta], \tag{145}$$

$$= -\frac{1}{2}\gamma_2\gamma_1. \tag{146}$$

As this is a time-independent integrand, we can drop the time-ordering $\mathcal{T}$ and trivially solve the Berry phase

$$U = \exp\left(-\int_0^{\frac{\pi}{2}} -\frac{1}{2}\gamma_2\gamma_1\, d\omega\right) = \exp\left(\frac{\pi}{4}\gamma_2\gamma_1\right). \tag{147}$$

Summarizing the effect on the ground state sector as an exchange of MBSs γ_1 and γ_2.

14.2 Energy splittings in the hybridization-based braiding protocol due to imperfect MBSs

In the following, we will motivate the generalized braiding protocol. We will start by revisiting the hybridization-based braiding protocol for a perfect system introduced in section 8.1 and provide a solution in terms of MBS diagrammatics. Afterwards, we discuss the error term that results from imperfect MBSs that are not fully localized on their respective sides, which breaks the necessary ground state degeneracy. Motivated by this, we will introduce the correction term that restores the degeneracy and finalizes the generalized braiding protocol. We will finish by illustrating a solution of this braiding Hamiltonian in terms of MBS diagrammatics.

Solving the hybridization-based protocol for perfect MBSs via MBS diagrammatics

The Hamiltonian for the hybridization-based protocol reads

$$H = \varepsilon\, i\gamma_1\tilde{\gamma}_1 + t_{12}\, i\gamma_1\gamma_2 + t_{13}\, i\gamma_1\gamma_3, \tag{148}$$

with time-dependent hybridizations $\varepsilon(\tau), t_{12}(\tau), t_{13}(\tau)$ creating a closed loop in parameter space over time T as introduced in section 8.1. The parameter loop is split into three time steps. We will focus the presented solution and generalization of the model on the second

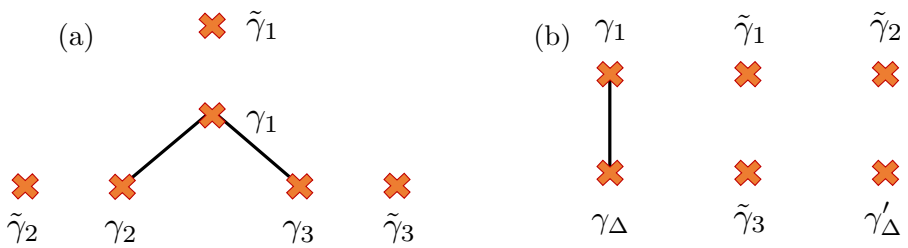

Figure 40: (a) The hybridizations (solid lines) during the second time step of the braiding protocol. The system corresponds to a minimal star network. (b) Applying the first move yields a graphical representation of the diagonalized version of the MBS system of the second protocol step.

time step of the protocol ($\tau \in [\frac{T}{3},\ 2\,\frac{T}{3}]$) as the resulting diagrams are the easiest to solve. A generalization to the whole parameter loop can be found in the supplementary information of paper IV.

Importantly, although the Hamiltonian has three hybridizations, the protocol is defined such that only a maximum of two hybridizations is turned on at any point in time. Therefore, we can apply the solution established in subsection 14.1 for the time-dependent minimal star network. During the second time step, the hybridization with γ_1 is transferred from γ_2 to γ_3 as shown in Figure 40 (a).

We diagonalize the network via the first move and use γ_Δ and γ'_Δ, see Figure 40 (b), to find the Berry phase of this second protocol step

$$U_{23} = \exp\left(\frac{\pi}{4}\gamma_3\gamma_2\right). \tag{149}$$

The intuitive picture is that the strong hybridization enforces $i\gamma_1\gamma_\Delta = -1$. The uncoupled MBS γ'_Δ has to adapt and shift around this energy gap in order for the system to stay in the ground state sector. As a result, if γ_2 shared a parity with any other uncoupled MBS γ_x, this information is pushed around by the energy gap and is now shared between γ_x and $\tilde{\gamma}_1$.

$$\gamma_2 = \gamma'_\Delta(\tau = T/3) \qquad \rightarrow \qquad \gamma'_\Delta(\tau = 2T/3) = -\tilde{\gamma}_1. \tag{150}$$

Interestingly, the minus sign predicts a flip of this parity consistent with the Berry phase result in Eq. (149). In the same manner, we can also solve the first (transferring the hybridization from $\tilde{\gamma}_1$) and third step (back to $\tilde{\gamma}_1$) and find

$$U_{23} = \exp\left(\frac{\pi}{4}\gamma_2\tilde{\gamma}_1\right), \qquad U_{31} = \exp\left(\frac{\pi}{4}\tilde{\gamma}_1\gamma_3\right), \tag{151}$$

We obtain the full Berry phase by multiplying the transformation of each step

$$U = U_{31}\,U_{23}\,U_{12} = \exp\left(\frac{\pi}{4}\gamma_3\gamma_2\right), \tag{152}$$

realizing a single braid of γ_2 and γ_3.

Generalizing the hybridization-based protocol to imperfect MBSs

In the following, we will generalize the previous protocol by accounting for finite spatial overlaps of the MBSs, see Figure 41. Formally, this corresponds to the transformation

$$\gamma_k \rightarrow \frac{1}{\sqrt{1+\zeta^2}}\,\gamma_k + i\frac{\zeta}{\sqrt{1+\zeta^2}}\,\tilde{\gamma}_k, \tag{153}$$

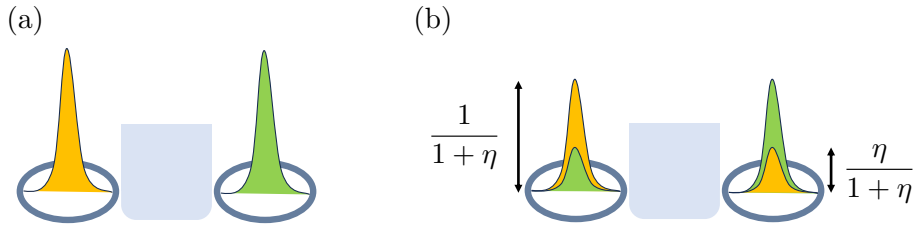

Figure 41: (a) Perfect MBS localized on their respective site exemplified on a QD-based Kitaev chain. (b) Imperfect MBSs with finite overlaps on the sites (QDs) of their neighboring MBSs. The overlap is parametrized by $\eta \in [0, 1]$, which fully interpolates between localized MBSs, $\eta = 0$, and a trivial fermion with fully overlapping MBS, $\eta = 1$.

overlapping each inner MBS γ_k with its outer neighbor $\tilde{\gamma}_k$, parametrized by $\zeta \in [0, 1]$. Applying this transformation to Eq. (148) modifies the Hamiltonian by introducing the error term in the second line of

$$\begin{aligned} H/\Delta =& \rho_1 \, i\gamma_1\tilde{\gamma}_1 + \rho_2 \, i\gamma_1\gamma_2 + \rho_3 \, i\gamma_1\gamma_3 \\ &+ \eta \, (\rho_2 \, i\tilde{\gamma}_1\tilde{\gamma}_2 + \rho_3 \, i\tilde{\gamma}_1\tilde{\gamma}_3), \end{aligned} \tag{154}$$

proportional to $\eta = \zeta^2$. We visualize its effect by revisiting the MBS diagram in the second step, see Figure 42 (a). This additional term couples $\tilde{\gamma}_1$ to $\tilde{\gamma}_2, \tilde{\gamma}_3$. We can apply the first move to this new minimal star network, defining γ_η, which is hybridized with γ_1 at coupling strength $\eta\,\Delta$, and the disconnected γ'_η, see Figure 42 (b). This representation summarizes the problem of this error term efficiently. The additional coupling assigns an energy $\pm\eta\,\Delta$ to the parity of $i\tilde{\gamma}_1\gamma_\eta$, thereby breaking the crucial ground state degeneracy.

14.3 Solving the generalized hybridization-based protocol for imperfect MBSs via MBS diagrammatics

The solution to the degeneracy breaking is motivated by considering Figure 42 (a) and hybridizing γ_2 with $\tilde{\gamma}_2$ and γ_3 with $\tilde{\gamma}_3$, which are the only pairs of neighbors where the hybridizations are not used yet. Remember that the pair $\gamma_1, \tilde{\gamma}_1$ is already hybridized during

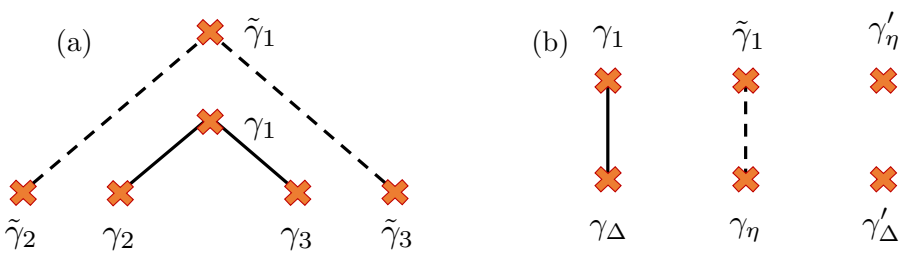

Figure 42: (a) Including hybridizations induced by imperfect MBSs (dashed lines) into the second protocol step. (b) Applying the first move to this outer minimal star network introduces $\gamma_\eta, \gamma'_\eta$. It visualizes the breaking of ground state degeneracy by hybridizing $\tilde{\gamma}_1$ with γ_η.

the first and third time step and can't be used for corrections. We thus arrive at the final Hamiltonian

$$\begin{aligned} H/\Delta =& \rho_1\, i\gamma_1\tilde{\gamma}_1 + \rho_2\, i\gamma_1\gamma_2 + \rho_3\, i\gamma_1\gamma_3 \\ &+ \eta\,(\rho_2\, i\tilde{\gamma}_1\tilde{\gamma}_2 + \rho_3\, i\tilde{\gamma}_1\tilde{\gamma}_3) \\ &+ \lambda\,(i\gamma_2\tilde{\gamma}_2 + i\gamma_3\tilde{\gamma}_3), \end{aligned} \tag{155}$$

visualized in Figure 43. The correction strength is parametrized by λ. In terms of the previously diagonalized basis, $\gamma_\Delta, \gamma'_\Delta$ and $\gamma_\eta, \gamma'_\eta$, this correction could introduce up to four hybridizations. One for each possible combination between the two groups.

After a few lines of algebra, see the supplementary information of paper IV, we find that the correction term only introduces two hybridizations, which are shown in Figure 43 (b). This is not obvious from the diagram and needs to be found via explicit calculation. The fact that this only introduces two terms is a direct consequence of the chosen symmetric form for the errors and correction (η is the same for $\tilde{\gamma}_2, \tilde{\gamma}_3$, and λ is the same for the pairs $2, 3$). Without this choice, the remaining calculation would, in principle, still be possible by multiple applications of the first and second moves. But it is not clear whether the final calculation of the Berry phase would yield a closed analytic solution in the general case.

To diagonalize Figure 43 (b), we apply the second move to split up the connection between γ_Δ and γ_η to find

$$H = \Delta^D\, i\gamma_1^D\gamma_\Delta^D + \varepsilon^D\, i\gamma_\eta^D\tilde{\gamma}_1^D + \lambda\, i\gamma'_\Delta\gamma'_\eta, \tag{156}$$

represented in Figure 44.

This final application of the second move yields the final, fully diagonalized Hamiltonian, which holds several pieces of information. As the connection we broke up was proportional to the correction parameter λ, all new MBS operators ($\gamma_1^D, \gamma_\Delta^D, \gamma_\eta^D, \tilde{\gamma}_1^D$) and hybridizations ($\Delta^D, \varepsilon^D$) are now dependent on it.

First, we obtain the generalized gap Δ^D (solid line) and associated MBS parity defining the

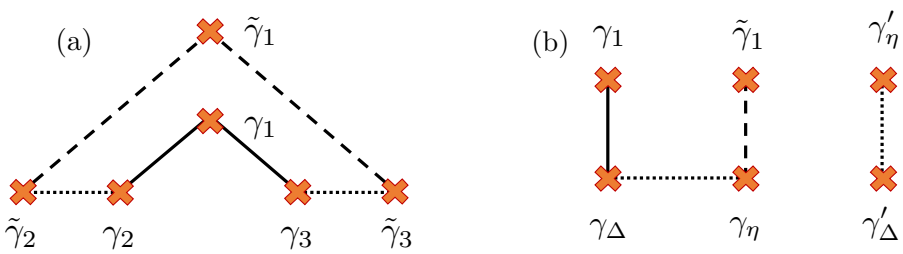

Figure 43: (a) Fully generalized system including hybridizations (dotted lines) introduced to correct the energy splitting. (b) Translating these corrections into the basis of the previously diagonal Hamiltonian with errors yields a chain of MBSs and a hybridization of γ'_η with γ'_Δ.

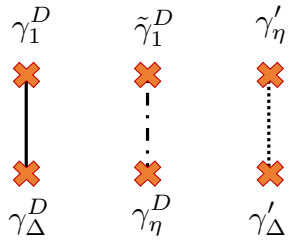

Figure 44: The final diagonal version of the full Hamiltonian obtained by breaking the chain of MBSs via the second move. This version of the Hamiltonian enables a full determination of the necessary correction strength by demanding degeneracy between the generalized error (dotted-dashed line) and correction (dotted). The generalized energy gap (solid line) with the associated parity fully determines the projector on the ground state sector.

ground state sector

$$i\gamma_1^D\gamma_\Delta^D = -1. \tag{157}$$

Within this ground state sector, we find the generalized splitting $\varepsilon^D(\eta,\lambda)$ (dotted dashed line) now depending on both error and correction. The following approach to fix this energy splitting uses the conserved parity within the total system

$$\sigma = i^3\gamma_1\tilde{\gamma}_1\,\gamma_2\tilde{\gamma}_2\,\gamma_3\tilde{\gamma}_3 = i^3\gamma_1^D\gamma_\Delta^D\,\gamma_\eta^D\tilde{\gamma}_1^D\,\gamma'_\Delta\gamma'_\eta. \tag{158}$$

Inserting Eq. (157) directly relates this to a conserved ground state parity from which we find the degeneracy condition

$$\varepsilon^D(\eta,\lambda) + \sigma\,\lambda = 0. \tag{159}$$

This is a nonlinear equation determining how λ has to be tuned in dependence on the error η to establish degeneracy. The solution for the correction $\lambda^*(\eta)$ is next used to find the projection operator following from Eq. (157)

$$P(\lambda^*(\eta),\eta) = \frac{1}{2}(1 - i\gamma_1^D\gamma_\Delta^D). \tag{160}$$

Generalizing the solution to describe the full protocol requires generalizing the expressions for $\varepsilon^D(\eta,\lambda)$ and $\gamma_1^D,\gamma_\Delta^D$ to all protocol steps. This results in a more involved dependence of these quantities on the protocol parametrizations ρ_1,ρ_2,ρ_3, which we left implicit in the chosen notation. The general Eqs. (159), (160), and the solution strategy stay unchanged by this.

Explicit calculations show that the generalized protocol closes the energy gap Δ^D at even total parity ($\sigma = 1$) in the trivial fermion limit ($\eta = 1$). At that parameter point, the gap closure makes an adiabatically slow execution of the protocol impossible. This does not happen for odd total parity. This is due to the choice of symmetric corrections ($+\lambda$

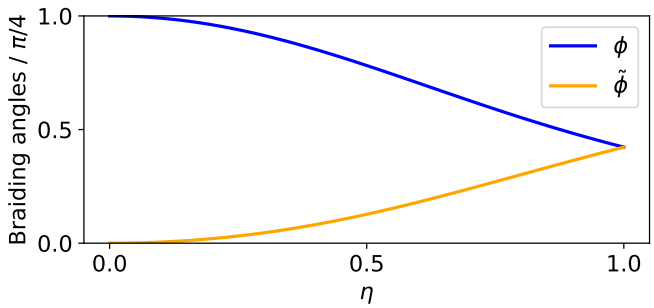

Figure 45: The generalized braiding angles interpolating a single braid of γ_2, γ_3 for perfect MBSs at $\eta = 0$ and (partially) exchanging $\tilde{\gamma}_2, \tilde{\gamma}_3$ at $\eta = 1$ representing a trivial fermionic exchange.

for both parities of Eq. (155)) instead of asymmetric corrections ($\pm\lambda$ on the parities). If we were to choose asymmetric corrections, the roles of even and odd total parity would be exchanged.

In the chosen symmetric correction with even total parity, we can use the general projectors $P(\eta)$ to solve the full Berry phase of the generalized protocol as

$$U(\eta) = \mathcal{T} \exp\left(- \oint [P(\eta), \partial_\omega P(\eta)]\, d\omega \right) = \exp(\phi(\eta)\, \gamma_3\gamma_2) \exp\left(\tilde{\phi}(\eta)\, \tilde{\gamma}_3\tilde{\gamma}_2\right), \quad (161)$$

with the generalized angles

$$\phi(\eta) = \frac{\pi}{4}\left(1 - \frac{\eta^2}{\sqrt{1+\eta^2+\eta^4}}\right), \qquad \tilde{\phi}(\eta) = \frac{\pi}{4}\left(1 - \frac{1}{\sqrt{1+\eta^2+\eta^4}}\right), \quad (162)$$

see Figure 45. This result describes the outcome of a braiding protocol capable of fully interpolating between perfect MBS ($\eta = 0$) with the known result

$$\phi(\eta = 0) = \frac{\pi}{4}, \qquad \tilde{\phi}(\eta = 0) = 0, \quad (163)$$

and trivial fermions ($\eta = 1$), where it predicts

$$\phi(\eta = 1) = \tilde{\phi}(\eta = 1) = \frac{\pi}{4}\left(1 - \frac{1}{\sqrt{3}}\right). \quad (164)$$

This exchange of both pairs with an angle around $0.42\frac{\pi}{4}$ is a trivial operation, as it corresponds to performing a partial exchange of the left (2) and right (3) fermion. In between these limits we find the general case, in which γ_2 and γ_3 are not fully exchanged any longer ($\phi < \frac{\pi}{4}$) but still experience a stronger rotation than $\tilde{\gamma}_2$ and $\tilde{\gamma}_3$ ($0 < \tilde{\phi} < \phi$).

Outlook and personal reflections

These are exciting times to work in the field of Majorana research. The continuous efforts of many experimental groups around the world are making the unique physics of device candidates for hosting MBSs more accessible with every peer-reviewed and published article. Our role as theorists is to keep track of that progress. Stay up to date with the strengths and weaknesses of different realizations, and provide these experimental groups with suggestions for ways to explore the opportunities opening up right now. In the following, we will view the results of papers I-IV in that light.

Experimental realizations of the proposal in papers I and II require the availability of a MBS tetron, which arguably poses a significant hurdle. The only group currently claiming the successful fabrication of such a device is Microsoft Quantum. Although their latest publication is based on a grounded version of the presented tetron, the suggested DC transport experiments are still possible. The required parity blockade is the same parameter tuning that Microsoft currently uses for their parity read-out. This parity read-out can be translated into the suggested tetron initialization and lifetime measurement. The slow DC transport measurements offer a simple alternative to the current single-shot parity read-out measurements. Also, an adapted version of the fusion rule experiments in paper II is possible by translating the x and z parity measurements into x and z parity-blocked transport setups. For the fusion rule experiment, another main difference lies in the different geometry of the proposed setup. The consequences of this difference for distinguishing between MBSs and trivial states are not obvious at this point and need to be investigated theoretically.

Experimental realizations of the proposal in papers III and IV, on the other hand, require the ability to build QD-based Kitaev chains with high control over the effective couplings, establishing a high localization of the unprotected MBSs. Experimental groups in Delft are currently world-leading in this technique. The current devices are 2- and 3-site Kitaev chains, which show a high level of controlability. With these fundamental building blocks, both the poor man's Majorana tetron and the performance of a hybridization-based braiding protocol are natural next steps. While the poor man's Majorana tetron doesn't offer a protected qubit platform, it grants access to the topological Kondo effect, which is unique

to MBS systems. One of the main experimental challenges lies in developing a design with the correct tuning of the charging energy, proximitized superconducting gap, and the effective couplings, t_{cot} and Δ_{CAR}. The investigated hybridization-based braiding protocol of paper IV is a natural choice for QD-based Kitaev chains, as the gate control over the effective couplings provides direct experimental control over the MBS hybridizations. The derived corrections neglected the shared dependence of spatial MBS overlap and MBS hybridization on the effective couplings in QD-based Kitaev chains. Future theory work can enhance the use of the correction protocol by investigating a specific model tailored to these systems.

References

[1] R. Schaller, IEEE Spectrum **34**, 52 (1997).

[2] C. A. Mack, IEEE Transactions on Semiconductor Manufacturing **24**, 202 (2011).

[3] B. Hoefflinger, *Chips 2020: a guide to the future of nanoelectronics* (Springer, 2012).

[4] E. Mathieu, Moore's law has accurately predicted the progress in transistor counts over the last 50 years (2024), our World in Data, published April 15, 2024.

[5] M. A. Nielsen and I. L. Chuang, *Quantum computation and quantum information* (Cambridge university press, 2010).

[6] H. Riesel, *Prime numbers and computer methods for factorization*, Vol. 57 (Springer Science & Business Media, 2013).

[7] J. P. Buhler, H. W. Lenstra, and C. Pomerance, in *The development of the number field sieve*, edited by A. K. Lenstra and H. W. Lenstra (Springer Berlin Heidelberg, Berlin, Heidelberg, 1993) pp. 50–94.

[8] R. L. Rivest, A. Shamir, and L. Adleman, Commun. ACM **21**, 120–126 (1978).

[9] A. Robert, P. K. Barkoutsos, S. Woerner, and I. Tavernelli, npj Quantum Information **7**, 38 (2021).

[10] A. Khalid, S. Tufail, and A. I. Sarwat, in *SoutheastCon 2021* (2021) pp. 1–7.

[11] T. D. Ladd, F. Jelezko, R. Laflamme, Y. Nakamura, C. Monroe, and J. L. O'Brien, Nature **464**, 45 (2010).

[12] M. Cerezo, A. Arrasmith, R. Babbush, S. C. Benjamin, S. Endo, K. Fujii, J. R. McClean, K. Mitarai, X. Yuan, L. Cincio, and P. J. Coles, Nature Reviews Physics **3**, 625 (2021).

[13] IBM, Ibm quantum at ces 2020, https://newsroom.ibm.com/media-quantum-innovation?keywords=quantum&l=100 (2023), accessed: 3 November 2023.

[14] IBM Quantum, Ibm debuts next-generation quantum processor & ibm quantum system two, extends roadmap to advance era of quantum utility, https://www.ibm.com/quantum/blog/quantum-roadmap-2033 (2023), introduces IBM Condor, a 1,121-qubit superconducting quantum processor based on cross-resonance gate technology.

[15] F. Leymann and J. Barzen, Quantum Science and Technology **5**, 044007 (2020).

[16] A. Kitaev, Annals of Physics **303**, 2 (2003).

[17] K. J. S. *et al.*, Science **374**, 1237 (2021).

[18] Z. Chen *et al.*, Nature **595**, 383 (2021).

[19] T. I. Andersen *et al.*, Nature **618**, 264 (2023).

[20] R. Acharya *et al.*, Nature **614**, 676 (2023).

[21] E. Majorana, Il Nuovo Cimento (1924-1942) **14**, 171 (1937).

[22] A. Y. Kitaev, Physics-Uspekhi **44**, 131 (2001).

[23] M. Leijnse and K. Flensberg, Semiconductor Science and Technology **27**, 124003 (2012).

[24] J. F. Annett, *Superconductivity, superfluids and condensates*, Oxford master series in condensed matter physics (Oxford Univ. Press, Oxford, 2004).

[25] D. J. Griffiths and D. F. Schroeter, *Introduction to Quantum Mechanics*, 3rd ed. (Cambridge University Press, 2018).

[26] S. Nadj-Perge, I. K. Drozdov, B. A. Bernevig, and A. Yazdani, Phys. Rev. B **88**, 020407 (2013).

[27] O. A. Awoga, I. Ioannidis, A. Mishra, M. Leijnse, M. Trif, and T. Posske, Phys. Rev. Res. **6**, 033154 (2024).

[28] D. A. Ivanov, Phys. Rev. Lett. **86**, 268 (2001).

[29] Y. Oreg, G. Refael, and F. von Oppen, Phys. Rev. Lett. **105**, 177002 (2010).

[30] R. M. Lutchyn, J. D. Sau, and S. Das Sarma, Phys. Rev. Lett. **105**, 077001 (2010).

[31] J. Bardeen, L. N. Cooper, and J. R. Schrieffer, Phys. Rev. **108**, 1175 (1957).

[32] N. Leumer, M. Marganska, B. Muralidharan, and M. Grifoni, Journal of Physics: Condensed Matter **32**, 445502 (2020).

[33] D. Sticlet, C. Bena, and P. Simon, Phys. Rev. B **87**, 104509 (2013).

[34] I. Mahyaeh and E. Ardonne, Journal of Physics Communications **2**, 045010 (2018).

[35] R. Aguado, La Rivista del Nuovo Cimento **40**, 523–593 (2017).

[36] M. Nitsch, kitaev_chain: Release for thesis plots, `https://github.com/NitschMax/kitaev_chain/releases/tag/thesis-plot` (2025), version: thesis-plot.

[37] S.-Q. Shen, Topological invariants, in *Topological Insulators: Dirac Equation in Condensed Matter* (Springer Singapore, Singapore, 2017) pp. 51–79.

[38] J. Alicea, Reports on Progress in Physics **75**, 076501 (2012).

[39] G. Kells, D. Meidan, and P. W. Brouwer, Phys. Rev. B **86**, 100503 (2012).

[40] S. Datta, *Electronic Transport in Mesoscopic Systems* (Cambridge University Press, Cambridge, UK, 1995).

[41] M. Nitsch, nanowire_simulation: Thesis plots release, `https://github.com/NitschMax/nanowire_simulation/releases/tag/thesis-plots` (2025), release: thesis-plots.

[42] H. Pan and S. Das Sarma, Phys. Rev. Res. **2**, 013377 (2020).

[43] A. P. Mackenzie and Y. Maeno, Rev. Mod. Phys. **75**, 657 (2003).

[44] A. Pustogow, Y. Luo, A. Chronister, Y. Su, D. A. Sokolov, and etc., Nature **574**, 72–75 (2019).

[45] H. Yoon, Y. S. Eo, J. Park, J. A. Horn, R. G. Dorman, S. R. Saha, I. M. Hayes, I. Takeuchi, P. M. R. Brydon, and J. Paglione, npj Quantum Materials **9**, 91 (2024).

[46] P. Marra, Journal of Applied Physics **132**, 231101 (2022).

[47] S. Vaitiekėnas, A. M. Whiticar, M.-T. Deng, F. Krizek, J. E. Sestoft, C. J. Palmstrøm, S. Marti-Sanchez, J. Arbiol, P. Krogstrup, L. Casparis, and C. M. Marcus, Phys. Rev. Lett. **121**, 147701 (2018).

[48] M. Amundsen, J. Linder, J. W. A. Robinson, I. Žutić, and N. Banerjee, Rev. Mod. Phys. **96**, 021003 (2024).

[49] W. Belzig, C. Bruder, and G. Schön, Phys. Rev. B **54**, 9443 (1996).

[50] S. Gueron, Quasiparticles in a diffusive conductor: interaction and pairing (1997).

[51] M. Kjaergaard, H. J. Suominen, M. P. Nowak, A. R. Akhmerov, J. Shabani, C. J. Palmstrøm, F. Nichele, and C. M. Marcus, Phys. Rev. Appl. **7**, 034029 (2017).

[52] A. E. G. Mikkelsen, P. Kotetes, P. Krogstrup, and K. Flensberg, Phys. Rev. X **8**, 031040 (2018).

[53] R. M. Lutchyn, E. P. A. M. Bakkers, L. P. Kouwenhoven, P. Krogstrup, C. M. Marcus, and Y. Oreg, Nature Reviews Materials **3**, 52 (2018).

[54] P. Krogstrup, N. L. B. Ziino, W. Chang, S. M. Albrecht, M. H. Madsen, E. Johnson, J. Nygård, C. M. Marcus, and T. S. Jespersen, Nature Materials **14**, 400 (2015).

[55] F. Nichele, A. C. C. Drachmann, A. M. Whiticar, E. C. T. O'Farrell, H. J. Suominen, A. Fornieri, T. Wang, G. C. Gardner, C. Thomas, A. T. Hatke, P. Krogstrup, M. J. Manfra, K. Flensberg, and C. M. Marcus, Phys. Rev. Lett. **119**, 136803 (2017).

[56] V. Mourik, K. Zuo, S. M. Frolov, S. R. Plissard, E. P. A. M. Bakkers, and L. P. Kouwenhoven, Science **336**, 1003 (2012).

[57] M. T. Deng, C. L. Yu, G. Y. Huang, M. Larsson, P. Caroff, and H. Q. Xu, Nano Letters **12**, 6414 (2012), pMID: 23181691, https://doi.org/10.1021/nl303758w .

[58] A. D. K. Finck, D. J. Van Harlingen, P. K. Mohseni, K. Jung, and X. Li, Phys. Rev. Lett. **110**, 126406 (2013).

[59] M. T. Deng, S. Vaitiekenas, E. B. Hansen, J. Danon, M. Leijnse, K. Flensberg, J. Nygård, P. Krogstrup, and C. M. Marcus, Science **354**, 1557 (2016).

[60] S. Vaitiėkenas, G. W. Winkler, B. van Heck, T. Karzig, M.-T. Deng, K. Flensberg, L. I. Glazman, C. Nayak, P. Krogstrup, R. M. Lutchyn, and C. M. Marcus, Science **367**, 10.1126/science.aav3392 (2020).

[61] A. Yazdani, F. von Oppen, B. I. Halperin, and A. Yacoby, Science **380**, eade0850 (2023).

[62] E. Prada, P. San-Jose, and R. Aguado, Phys. Rev. B **86**, 180503(R) (2012).

[63] J. Avila, F. Peñaranda, E. Prada, P. San-Jose, and R. Aguado, Communications Physics **2**, 133 (2019).

[64] E. Prada, P. San-Jose, M. W. A. de Moor, A. Geresdi, E. J. H. Lee, J. Klinovaja, D. Loss, J. Nygård, R. Aguado, and L. P. Kouwenhoven, Nature Reviews Physics **2**, 575 (2020).

[65] J. D. Sau and S. Das Sarma, Nat. Commun. **3**, 964 (2012).

[66] M. Leijnse and K. Flensberg, Phys. Rev. B **86**, 134528 (2012).

[67] G. Wang, T. Dvir, G. P. Mazur, C.-X. Liu, N. van Loo, S. L. D. ten Haaf, A. Bordin, S. Gazibegovic, G. Badawy, E. P. A. M. Bakkers, M. Wimmer, and L. P. Kouwenhoven, Nature **612**, 448 (2022).

[68] T. Dvir, G. Wang, N. van Loo, C.-X. Liu, G. P. Mazur, A. Bordin, S. L. D. ten Haaf, J.-Y. Wang, D. van Driel, F. Zatelli, X. Li, F. K. Malinowski, S. Gazibegovic, G. Badawy, E. P. A. M. Bakkers, M. Wimmer, and L. P. Kouwenhoven, Nature **614**, 445 (2023).

[69] Q. Wang, S. L. D. ten Haaf, I. Kulesh, D. Xiao, C. Thomas, M. J. Manfra, and S. Goswami, Nature Communications **14**, 4876 (2023).

[70] A. Bordin, G. Wang, C.-X. Liu, S. L. D. ten Haaf, N. van Loo, G. P. Mazur, D. Xu, D. van Driel, F. Zatelli, S. Gazibegovic, G. Badawy, E. P. A. M. Bakkers, M. Wimmer, L. P. Kouwenhoven, and T. Dvir, Phys. Rev. X **13**, 031031 (2023).

[71] D. van Driel, R. Koch, V. P. M. Sietses, S. L. D. ten Haaf, C.-X. Liu, F. Zatelli, B. Roovers, A. Bordin, N. van Loo, G. Wang, J. C. Wolff, G. P. Mazur, T. Dvir, I. Kulesh, Q. Wang, A. M. Bozkurt, S. Gazibegovic, G. Badawy, E. P. A. M. Bakkers, M. Wimmer, S. Goswami, J. L. Lado, L. P. Kouwenhoven, and E. Greplova, arXiv:2405.04596 (2024).

[72] A. Bordin, X. Li, D. van Driel, J. C. Wolff, Q. Wang, S. L. D. ten Haaf, G. Wang, N. van Loo, L. P. Kouwenhoven, and T. Dvir, Phys. Rev. Lett. **132**, 056602 (2024).

[73] S. L. D. ten Haaf, Q. Wang, A. M. Bozkurt, C.-X. Liu, I. Kulesh, P. Kim, D. Xiao, C. Thomas, M. J. Manfra, T. Dvir, M. Wimmer, and S. Goswami, Nature **630**, 329 (2024).

[74] A. Bordin, F. J. B. Evertsz', B. Roovers, J. D. T. Luna, W. D. Huisman, F. Zatelli, G. P. Mazur, S. L. D. ten Haaf, G. Badawy, E. P. A. M. Bakkers, C.-X. Liu, R. S. Souto, N. van Loo, and L. P. Kouwenhoven, arXiv:2504.13702 (2025).

[75] S. L. D. ten Haaf, Q. Wang, A. M. Bozkurt, C.-X. Liu, I. Kulesh, P. Kim, D. Xiao, C. Thomas, M. J. Manfra, T. Dvir, M. Wimmer, and S. Goswami, Nature **630**, 329 (2024).

[76] R. Seoane Souto and R. Aguado, Subgap states in semiconductor-superconductor devices for quantum technologies: Andreev qubits and minimal majorana chains, in *New Trends and Platforms for Quantum Technologies* (Springer Nature Switzerland, 2024) p. 133–223.

[77] C.-X. Liu, G. Wang, T. Dvir, and M. Wimmer, Phys. Rev. Lett. **129**, 267701 (2022).

[78] J. M. Leinaas and J. Myrheim, Il Nuovo Cimento B (1971-1996) **37**, 1 (1977).

[79] F. Wilczek, Phys. Rev. Lett. **48**, 1144 (1982).

[80] C. Nayak, S. H. Simon, A. Stern, M. Freedman, and S. Das Sarma, Rev. Mod. Phys. **80**, 1083 (2008).

[81] F. Wilczek, *Fractional statistics and anyon superconductivity*, Vol. 5 (World scientific, 1990).

[82] M. Greiter and F. Wilczek, Annual review of condensed matter physics **15**, 131 (2024).

[83] D. J. Clarke, J. D. Sau, and S. Tewari, Phys. Rev. B **84**, 035120 (2011).

[84] E. Cohen, H. Larocque, F. Bouchard, F. Nejadsattari, Y. Gefen, and E. Karimi, Nature Reviews Physics **1**, 437 (2019).

[85] C. W. J. Beenakker, SciPost Phys. Lect. Notes , 15 (2020).

[86] F. Hassler, Topological quantum computing (2024), arXiv:2410.13547 [quant-ph] .

[87] J. Alicea, Y. Oreg, G. Refael, F. von Oppen, and M. P. A. Fisher, Nature Physics **7**, 412 (2011).

[88] B. van Heck, A. R. Akhmerov, F. Hassler, M. Burrello, and C. W. J. Beenakker, New Journal of Physics **14**, 035019 (2012).

[89] T. Karzig, F. Pientka, G. Refael, and F. von Oppen, Phys. Rev. B **91**, 201102 (2015).

[90] M. Hell, J. Danon, K. Flensberg, and M. Leijnse, Phys. Rev. B **94**, 035424 (2016).

[91] D. Aasen, M. Hell, R. V. Mishmash, A. Higginbotham, J. Danon, M. Leijnse, T. S. Jespersen, J. A. Folk, C. M. Marcus, K. Flensberg, and J. Alicea, Phys. Rev. X **6**, 031016 (2016).

[92] M. Hell, M. Leijnse, and K. Flensberg, Phys. Rev. Lett. **118**, 107701 (2017).

[93] D. J. Clarke, J. D. Sau, and S. Das Sarma, Phys. Rev. B **95**, 155451 (2017).

[94] A. Tsintzis, R. S. Souto, K. Flensberg, J. Danon, and M. Leijnse, PRX Quantum **5**, 010323 (2024).

[95] M. Hell, K. Flensberg, and M. Leijnse, Phys. Rev. B **96**, 035444 (2017).

[96] J. K. Pachos and S. H. Simon, New Journal of Physics **16**, 065003 (2014).

[97] T. Karzig, C. Knapp, R. M. Lutchyn, P. Bonderson, M. B. Hastings, C. Nayak, J. Alicea, K. Flensberg, S. Plugge, Y. Oreg, C. M. Marcus, and M. H. Freedman, Phys. Rev. B **95**, 235305 (2017).

[98] D. Aasen, M. Aghaee, Z. Alam, *et al.*, Roadmap to fault tolerant quantum computation using topological qubit arrays (2025), arXiv:2502.12252 [quant-ph] .

[99] H. L. Stormer, Rev. Mod. Phys. **71**, 875 (1999).

[100] F. Hassler, A. R. Akhmerov, and C. W. J. Beenakker, New Journal of Physics **13**, 095004 (2011).

[101] S. Plugge, L. A. Landau, E. Sela, A. Altland, K. Flensberg, and R. Egger, Phys. Rev. B **94**, 174514 (2016).

[102] T. Hyart, B. van Heck, I. C. Fulga, M. Burrello, A. R. Akhmerov, and C. W. J. Beenakker, Phys. Rev. B **88**, 035121 (2013).

[103] S. Plugge, A. Rasmussen, R. Egger, and K. Flensberg, New Journal of Physics **19**, 012001 (2017).

[104] M. Aghaee, Z. Alam, R. Andersen, *et al.*, Distinct lifetimes for x and z loop measurements in a majorana tetron device (2025), arXiv:2507.08795 [cond-mat.mes-hall] .

[105] M. I. K. Munk, J. Schulenborg, R. Egger, and K. Flensberg, Phys. Rev. Res. **2**, 033254 (2020).

[106] J. F. Steiner and F. von Oppen, Phys. Rev. Res. **2**, 033255 (2020).

[107] J. Schulenborg, S. Krøjer, M. Burrello, M. Leijnse, and K. Flensberg, Phys. Rev. B **107**, L121401 (2023).

[108] M. Aghaee, A. Alcaraz Ramirez, Z. Alam, *et al.*, Nature **638**, 651 (2025).

[109] H.-P. Breuer and F. Petruccione, *The Theory of Open Quantum Systems* (Oxford University Press, 2007).

[110] L. Fu, Phys. Rev. Lett. **104**, 056402 (2010).

[111] G. Kiršanskas, J. N. Pedersen, O. Karlström, M. Leijnse, and A. Wacker, Computer Physics Communications **221**, 317 (2017).

[112] B. Béri and N. R. Cooper, Phys. Rev. Lett. **109**, 156803 (2012).

[113] J. Kondo, Progress of Theoretical Physics **32**, 37 (1964), https://academic.oup.com/ptp/article-pdf/32/1/37/5193092/32-1-37.pdf .

[114] P. W. Anderson, Phys. Rev. **124**, 41 (1961).

[115] J. R. Schrieffer and P. A. Wolff, Phys. Rev. **149**, 491 (1966).

[116] K. G. Wilson, Rev. Mod. Phys. **47**, 773 (1975).

[117] A. C. Hewson, *The Kondo problem to heavy fermions*, 2 (Cambridge university press, 1997).

[118] R. Bulla, T. A. Costi, and T. Pruschke, Rev. Mod. Phys. **80**, 395 (2008).

[119] B. M. de Souza Melo, L. G. G. V. D. da Silva, A. R. Rocha, and C. Lewenkopf, Journal of Physics: Condensed Matter **32**, 095602 (2019).

[120] H. Schoeller, Transport theory of interacting quantum dots, in *Mesoscopic Electron Transport*, edited by L. L. Sohn, L. P. Kouwenhoven, and G. Schön (Springer Netherlands, Dordrecht, 1997) pp. 291–330.

[121] L. P. Kouwenhoven, C. M. Marcus, P. L. McEuen, S. Tarucha, R. M. Westervelt, and N. S. Wingreen, Electron transport in quantum dots, in *Mesoscopic Electron Transport*, edited by L. L. Sohn, L. P. Kouwenhoven, and G. Schön (Springer Netherlands, Dordrecht, 1997) pp. 105–214.

[122] B. Misra and E. C. G. Sudarshan, Journal of Mathematical Physics **18**, 756 (1977).

[123] J. E. Avron, L. Sadun, J. Segert, and B. Simon, Communications in Mathematical Physics **124**, 595 (1989).